GDAŃSK UNIVERSITY
OF TECHNOLOGY

The author of the doctoral dissertation: Aleksandra Wieloszyńska
Scientific discipline: Automation, electronic, electrical engineering and space technologies

DOCTORAL DISSERTATION

Title of doctoral dissertation: Anisotropic optical properties of few-layer black phosphorus coatings: from fundamental insights to opto-electrochemical sensor design

Title of doctoral dissertation (in Polish): Anizotropowe właściwości optyczne powłok z kilkuwarstwowego czarnego fosforu: badania podstawowych parametrów na potrzeby konstrukcji czujników opto-elektrochemicznych

Supervisor *signature*
Robert Bogdanowicz, PhD, Assoc. Prof.
Auxiliary supervisor *signature*
Paweł Jakóbczyk, PhD

GDAŃSK UNIVERSITY
OF TECHNOLOGY

STATEMENT

The author of the PhD dissertation: Aleksandra Wieloszyńska

I, the undersigned, agree/~~do not agree~~* that my PhD dissertation entitled:
Anisotropic optical properties of few-layer black phosphorus coatings: from fundamental insights to opto-electrochemical sensor design

may be used for scientific or didactic purposes.[1]

Gdańsk,...................................... ....
signature of the PhD student

Aware of criminal liability for violations of the Act of 4th February 1994 on Copyright and Related Rights (Journal of Laws 2006, No. 90, item 631) and disciplinary actions set out in the Law on Higher Education (Journal of Laws 2012, item 572 with later amendments),[2] as well as civil liability, I declare, that the submitted PhD dissertation is my own work.

I declare, that the submitted PhD dissertation is my own work performed under and in cooperation with the supervision of Robert Bogdanowicz, PhD, Assoc. Prof., the auxiliary supervision of Paweł Jakóbczyk, PhD.

This submitted PhD dissertation has never before been the basis of an official procedure associated with the awarding of a PhD degree.

All the information contained in the above thesis which is derived from written and electronic sources is documented in a list of relevant literature in accordance with art. 34 of the Copyright and Related Rights Act.

I confirm that this PhD dissertation is identical to the attached electronic version.

Gdańsk,...................................... ....
signature of the PhD student

I, the undersigned, agree/~~do not agree~~* to include an electronic version of the above PhD dissertation in the open, institutional, digital repository of Gdańsk University of Technology, Pomeranian Digital Library, and for it to be submitted to the processes of verification and protection against misappropriation of authorship.

Gdańsk,...................................... ....
signature of the PhD student

*) delete where appropriate.

---

[1] Decree of Rector of Gdansk University of Technology No. 34/2009 of 9th November 2009, TUG archive instruction addendum No. 8.

[2] Act of 27th July 2005, Law on Higher Education: Chapter 7, Criminal responsibility of PhD students, Article 226.

ABSTRACT

Few-layer black phosphorus (FLBP) is characterised by a tuneable bandgap, high carrier mobility and anisotropic optical properties. It therefore has the potential to find applications in electronics and photonics. FLBP oxidizes upon exposure to air, limiting its utility in devices and components. To address this issue, the thesis introduces methods and tools developed for studying FLBP's optical parameters, with a particular emphasis on its potential for sensing applications. Spectroscopic ellipsometry and polarisation microscopy were utilised to characterise the optical properties of multilayer black phosphorus in relation to its degradation processes and optical anisotropy. The dissertation also employed photoluminescence and electrochemistry techniques for the characterization and evaluation of the black phosphorus-based sensor for metal ion detection. Ellipsometry was used to determine the refractive index and extinction coefficient of FLBP, demonstrating that separating and centrifuging the bulk material can yield a layer with optical parameters closely resembling those of a two-dimensional material. Polarizing microscopy studies made it possible to determine the kinetics of the black phosphorus oxidation process, thereby revealing how it modifies the polarization parameters. Polarizing microscopy studies made it possible to determine the kinetics of the black phosphorus oxidation process, which modifies the polarization parameters. For the sensor design, FLBP was combined with zinc oxide, firstly to increase the resistance of black phosphorus to degradation by oxidation, and secondly to shift the photoluminescence response of the sensor into the visible region. This approach allowed the use of silicon detector in the photoluminescent sensor, enabling the detection of zinc and magnesium ions at lower concentrations than those detected by standard solutions.

STRESZCZENIE

Kilkuwarstwowy czarny fosfor charakteryzuje się przestrajalną przerwą energetyczną, wysokimi ruchliwościami nośników oraz anizotropowymi właściwościami optycznymi. Z tego względu ma potencjał, aby znaleźć zastosowanie w elektronice i fotonice. Kilkuwarstwowy czarny fosfor ulega utlenianiu w zetknięciu z powietrzem, co komplikuje jego bezpośrednie wykorzystywanie w urządzeniach i elementach. W niniejszej rozprawie zaproponowano metody i narzędzia opracowane do badania parametrów optycznych niskowymiarowego czarnego fosforu z ukierunkowaniem na zastosowania czujnikowe. W tym celu wykorzystano elipsometrię spektroskopową i mikroskopię polaryzacyjną do scharakteryzowania właściwości optycznych kilkuwarstwowego czarnego fosforu w aspekcie procesów jego degradacji oraz optycznej anizotropii. W rozprawie użyto technik fotoluminescencji i elektrochemii przy konstrukcji i badaniu efektywności czujnika na bazie czarnego fosforu do wykrywania jonów metali. Dzięki elipsometrii wyznaczono współczynnik załamania i ekstynkcji niskowymiarowego czarnego fosforu i pokazano, że przy odpowiedniej izolacji i separacji materiału objętościowego można uzyskać warstwę, której parametry optyczne zbliżone są do właściwości materiału dwuwymiarowego. Badania z użyciem mikroskopii polaryzacyjnej umożliwiły określenie kinetyki procesu utleniania czarnego fosforu modyfikujące jego parametry polaryzacyjne. Na potrzeby budowy czujników, połączono niskowymiarowy czarny fosfor z tlenkiem cynku, aby po pierwsze zwiększyć odporność czarnego fosforu na degradację przez utlenianie, a po drugie przesunąć fotoluminescencyjną odpowiedź czujnika w zakres widzialny. Takie podejście umożliwiło użycie krzemowych układów detekcji w czujniku fotoluminescencyjnym, umożliwiając wykrywanie jonów cynku i magnezu o niższych koncentracjach niż detekowane przez standardowe rozwiązania.

Table of contents

Abstract 3

Table of contents 4

List of abbreviation 6

List of publications 7

Chapter 1. Introduction to optoelectronic properties of two-dimensional materials 8

- 1.1 Graphene 8
- 1.2 Transition metal dichalcogenide 10
- 1.3 Phosphorene 13
- 1.4 Applications of two-dimensional materials 16

Chapter 2. Few-layer black phosphorus – optoelectronic properties and applications 20

- 2.1 Allotropes of phosphorus 20
- 2.2 Preparation and characterisation of few-layer black phosphorus 20
- 2.3 Optical and electrical parameters 23
- 2.4 Degradation of few-layer black phosphorus 28
- 2.5 Dichroism and birefringence in few-layer black phosphorus 33
- 2.6 Few-layer black phosphorus as a sensor device 36

Chapter 3. Motivation and aim of the thesis 39

Chapter 4. Experiments and results 43

- 4.1 Preparation and characterization of few-layer black phosphorus 43
  - 4.1.1 Electrochemical exfoliation of few-layer black phosphorus 43
  - 4.1.2 Liquid exfoliation of few-layer black phosphorus 48
  - 4.1.3 Mechanical exfoliation of few-layer black phosphorus 50
  - 4.1.4 Black arsenic-phosphorus preparation 50
  - 4.1.5 Black phosphorus – zinc oxide preparation 52
- 4.2 Optical constants of few-layer black phosphorus measured by spectroscopic ellipsometry 55
- 4.3 Optimalisation of microscopic measurements of polarisation imaging 59
  - 4.3.1 Polarisation analysis of few-layer black phosphorus 63
- 4.4 Black phosphorus – zinc oxide sensors to detect metal ions – design and investigation 71
  - 4.4.1 Photoluminescence sensor redouts 71
  - 4.4.2 Electrochemical sensor redouts 79

Chapter 5. Conclusions 87

References 91

List of figures 105
List of tables 110

List of abbreviation

2D material	Two-dimensional material
AC	Armchair
ALD	Atomic layer deposition
BP	Black phosphorus
CVD	Chemical vapor deposition
DFT	Density functional theory
DMF	N,N-dimethylformamide
EC	Electrochemistry
FLBP	Few-layer black phosphorus
mid-IR	Mid-infrared
ML	Monolayer
NIR	Near-infrared
NMP	N-methyl-2-pyrrolidone
PDMS	Polydimethylsiloxane
PL	Photoluminescence
PVD	Physical vapor deposition
TMDCs	Transition metal dichalcogenide
vdWf	van der Waals forces
ZZ	Zigzag

List of publications

1. **Aleksandra Wieloszyńska**, Krzysztof Pyrchla, Paweł Jakóbczyk, Dawid Lentka, Mirosław Sawczak, Łukasz Skowroński, Robert Bogdanowicz., "Tailoring optical constants of few-layer black phosphorus coatings: Spectroscopic ellipsometry approach supported by ab-initio simulation" – J. Ind. Eng. Chem., vol. 127, pp. 579–589, (2023)

2. Anna Dettlaff, Michał Rycewicz, Mateusz Ficek, **Aleksandra Wieloszyńska**, Mateusz Szala, Jacek Ryl, Robert Bogdanowicz, "Conductive printable electrodes tuned by boron-doped nanodiamond foil additives for nitroexplosive detection" – Microchimica Acta, 189(8), 1-11 (2022)

3. Srinivasu Kunuku, Mateusz Ficek, **Aleksandra Wieloszyńska**, Magdalena Tamulewicz-Szwajkowska, Krzysztof Gajewski, Miroslaw Sawczak, Aneta Lewkowicz, Jacek Ryl, Tedor Gotszalk, Robert Bogdanowicz, "Inluence of B/N co-doping on electrical and photoluminescence properties of CVD grown homoepitaxial diamond films" - Nanotechnology, 33.12: 12560 (2021)

4. Mattia Pierpaoli, Chiara Giosuè, Natalia Czerwińska, Michał Rycewicz, **Aleksandra Wieloszyńska**, Robert Bogdanowicz, Maria Letizia Ruello, "Characterization and Filtration Efficiency of Sustainable PLA Fibers Obtained via a Hybrid 3DPrinted/ Electrospinning Technique" – Materials -Vol. 14,iss. 22 (2021), s.6766-

5. Maciej R. Molas, Łukasz Macewicz, **Aleksandra Wieloszyńska**, Paweł Jakóbczyk, Andrzej Wysmołek, Robert Bogdanowicz, Jacek B. Jasiński, "Photoluminescence as a probe of phosphorene properties" — npj 2D Materials and Applications -Vol. 5,iss. 1 (2021), s.83

6. Michał Sobaszek, Marcin Strąkowski, Łukasz Skowroński, Katarzyna Siuzdak, Mirosław Sawczak, Igor Własny, Andrzej Wysmołek, **Aleksandra Wieloszyńska**, Jerzy Pluciński, Robert Bogdanowicz, "In-situ monitoring of electropolymerization processes at boron-doped diamond electrodes by Mach-Zehnder interferometer" - Sensors and Actuators B: Chemical 304 (2020): 127315

7. **Aleksandra Wieloszyńska**, Paweł Jakóbczyk, Robert Bogdanowicz, "Polarization-dependent optical absorption in phosphorene flakes" - Low-Dimensional Materials and Devices 2019 11085, 1108515 (2019)

Chapter 1. Introduction to optoelectronic properties of two-dimensional materials

As electronics develop, devices are becoming smaller and more compact. Moreover, these devices are supposed to work faster and more efficiently. Therefore, it is necessary to find new materials with specific properties that can meet the growing demand. The interest of scientists has turned to two-dimensional (2D) materials, i.e. materials that have by definition the thickness of a single atomic layer [1]–[3]. Material with a few atomic layers with properties that do not exist in traditional 3D materials are also included to 2D materials. With the ongoing miniaturisation, 2D materials' small dimensions make them very attractive. In addition, they are characterised by interesting optical and electrical properties that differ significantly from the parameters of their bulk forms. Graphene was the first known 2D material, although many more have been discovered since [4], such as transition metal dichalcogenide (TMDCs) [5], MXenes [6], and phosphorene [7]. Graphene is characterised by high conductivity [4], TMDCs on the other hand, have the wide bandgap [5], while phosphorene is known for its strong optical anisotropy [8]. Hence, 2D materials can be used in many electronic, optical and optoelectronic applications. Furthermore, their structures and small size affect their chemical reactivity, which has shown them to be excellent sensor devices [9], [10]. There are three main methods to synthesise 2D materials: mechanical exfoliation, liquid exfoliation, and chemical vapour deposition. In mechanical exfoliation, the Scotch tape is used to separate the individual layers from the bulk material. The method is simple, fast and inexpensive, but it is ineffective to produce larger flakes and the results are hardly controllable [11]. Samples produced by liquid exfoliation are more reproducible. To obtain a sample without defects, the type of solvent and the sonication time must be chosen carefully. Liquid exfoliated flakes are rather small, which limited their use in nanoelectronics and optoelectronics, but they are suitable for chemical and energy applications [12]. The bottom-up-based method for obtaining 2D materials is chemical (CVD) or physical vapour deposition (PVD). The number of defects and size of the growth sample are fully controllable through controlling the vapour deposition parameters, such as the precursor, temperature, atmosphere, pressure, and substrate [13], [14].

1.1 Graphene

Initially, theoretical considerations challenged the existence of 2D materials at temperatures beyond absolute zero. This changed in 2004, when Novosolev et al. produced graphene using mechanical exfoliation [4]. Graphene is composed of carbon atoms and can be easily obtained from graphite, in which layers are bonded by weak van der Waals forces (vdWf) [15]. Its honeycomb structure in different directions is shown in Fig. 1.1.

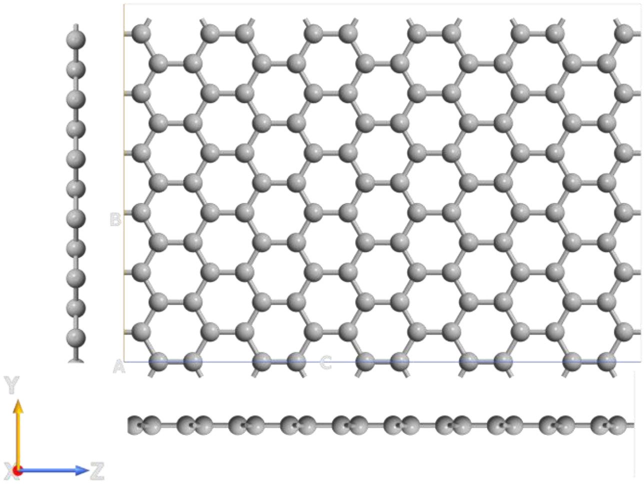

Fig. 1.1 Top and side views of atomic structure of graphene.

Graphene has almost zero bandgap and a low on/off ratio, which limited its applications in electronics. However, the bandgap can be tuned by strain and doping [16]. Theoretical and experimental studies show that replacing a C atom with, e.g., a nitrogen or boron atom opens up the graphene bandgap [17].

Graphene is also characterised by excellent electrical conductivity, good thermal conductivity, and high carrier mobility (3000–10,000 cm^2/Vs [4]). Moreover, the quantum Hall effect appears in graphene at room temperature [18], [19]. Graphene is notable for its optical properties, particularly its transparency in the visible to near-infrared (NIR) range. [20]. Furthermore, its absorption practically does not change with the frequency but depends on the thickness [21]. This is seen in the absorbance spectra shown in Fig. 1.2. Fig. 1.2a presents a comparison of theoretical and experimental results for 10 layers, 5 layers and monolayer (circle, square and triangle, respectively) [21]. The absorbance increases with the increasing number of layers. The density functional theory (DFT) calculated absorbance spectra for 1–4 layers is present in Fig. 1.2b [22]. The smallest absorbance was obtained for monolayer graphene, and the largest for 4-layer graphene. All the characteristics had a similar shape, and the absorbance slowly increased as the wavelength decreased. Graphene’s optical parameters can be tuned. The optical transmission changes after electrical gating or charge injection [23].

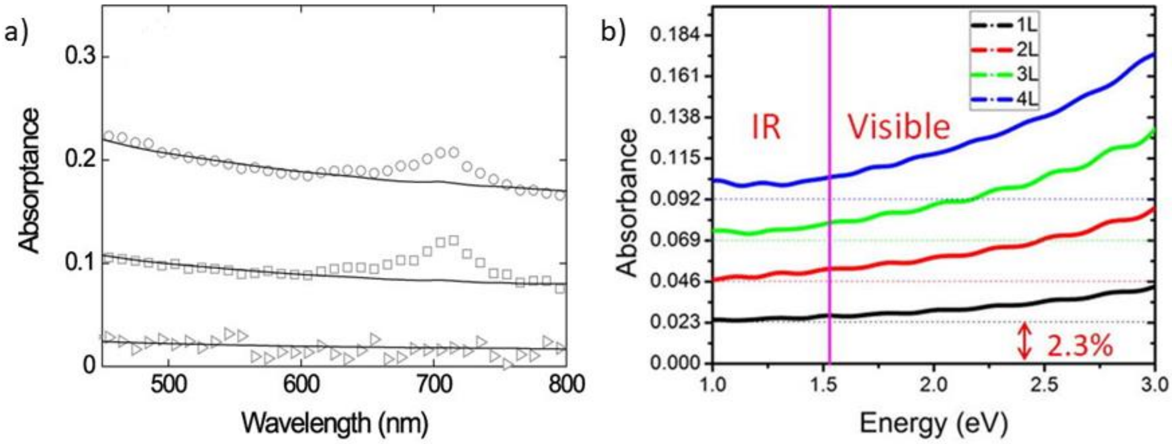

Fig. 1.2 a) Measured and calculated absorptance of graphene with 10 layers, 5 layers and monolayer (circle, square and triangle, respectively). Reprinted with permission from [21]. Copyright 2013 American Chemical Society. b) Absorbance of graphene from 1 to 4 layers. Reprinted from [22], with the permission of AIP Publishing.

Due to its symmetrical structure, monolayer graphene is optically isotropic. However, in twisted bilayer graphene, the symmetry is broken and some optical anisotropy can be identified using, for example, Raman spectroscopy [24]. Defects can also influence the optical properties of graphene [25]. In graphene, we can find various types of defects: stone-walls defect, single and multiple vacancies, carbon adatoms, foreign adatoms, substitutional impurities, dislocations (one-dimensional defects), edge defects [26], [27]. Due to the small thickness, interstitial atoms use the third dimension to connect the structure, e.g. the bridge configuration. In other cases, very high energy is needed [28]. There are free atoms at the edge of graphene, or they are passivated with hydrogen atoms. Reconstructions and removing carbon atoms lead to changes at the edges [29]. Furthermore, electron and ion irradiation and the chemical method can also produce defects in the graphene structure. Defects can cause enhanced chemical reactivity and change the electrical properties, e.g. open the bandgap or increase the conductivity [26], [27], [30].

The discovery of graphene sparked research into 2D materials. However, graphene's limited use in electronic applications, due to its lack of a bandgap and low on-off ratio, prompted a search for alternative materials.

1.2 Transition metal dichalcogenide

TMDCs are devoid of graphene disadvantages [5]. These semiconducting materials are of the MX_2 type, where M is a transition metal atom (e.g. Mo, W) and X is a chalcogen atom (e.g. S, Se). They create a covalently bonded X-M-X layer. The lattice constant changes according to the size of the ionic radius of the X atom. In addition, depending of the combination of M and X elements, different phases can be observed in TMDCs [31]: hexagonal (2H), rhombohedral (3R), octahedral (T), distorted octahedral (T'), orthorhombic (T_d). The example structure of TMDCs is shown in Fig. 1.3a [32].

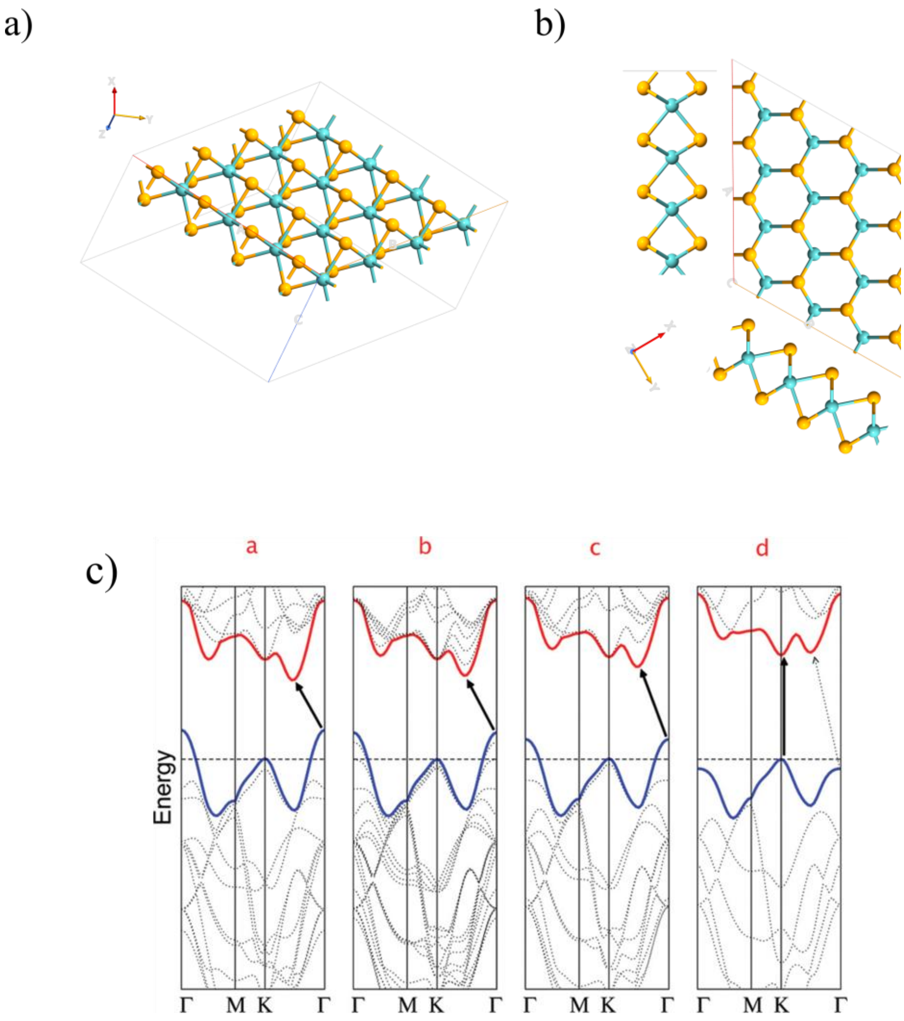

Fig. 1.3 a) Isometric and b) top and side views of atomic structure of $MoSe_2$. The yellow and blue balls represent Mo and Se atoms, respectively. c) Calculated band structures of a – bulk, b – 4-layer, c – 2-layer, and d – monolayer MoS2. Reprinted with permission from [33]. Copyright 2023 American Chemical Society.

As was mentioned, the TMDCs have non-zero bandgap, which can be tuned from 1 eV to ~2eV [5]. Furthermore, it depends on the number of layers and is usually direct only for a monolayer, as was shown in Fig. 1.3b. But the bandgap can also be changed by strain [34] or doping [35]. By applying a strain to the monolayer, we can change the bandgap to an indirect one. The carrier mobility of TMDCs is generally lower than the value obtained in graphene. For example, the carrier mobility for molybdenum disulfide (MoS_2) is up to 200 cm^2/Vs, but the on-off ratio is much higher ($1x10^8$) [36]. Thus, TMDCs are more important in many electronic applications than graphene.

Like graphene, TMDCs' optical parameters are impacted by various factors, including the exfoliation method [37], type of substrate [38], and the existence of defects in the structure [39]. Fig. 1.4 presents the differences in absorption spectra for MoS_2 (Fig. 1.4a) and $MoSe_2$ (Fig. 1.4c) on Si, SiO_2 or SiO_2/Si. The lowest absorption was obtained for pure silica as a substrate and the highest for SiO_2/Si. Fig. 1.4b and Fig. 1.4d show that using Au between the MoS_2/$MoSe_2$ layer and the substate make the absorption identical for different substrates [38].

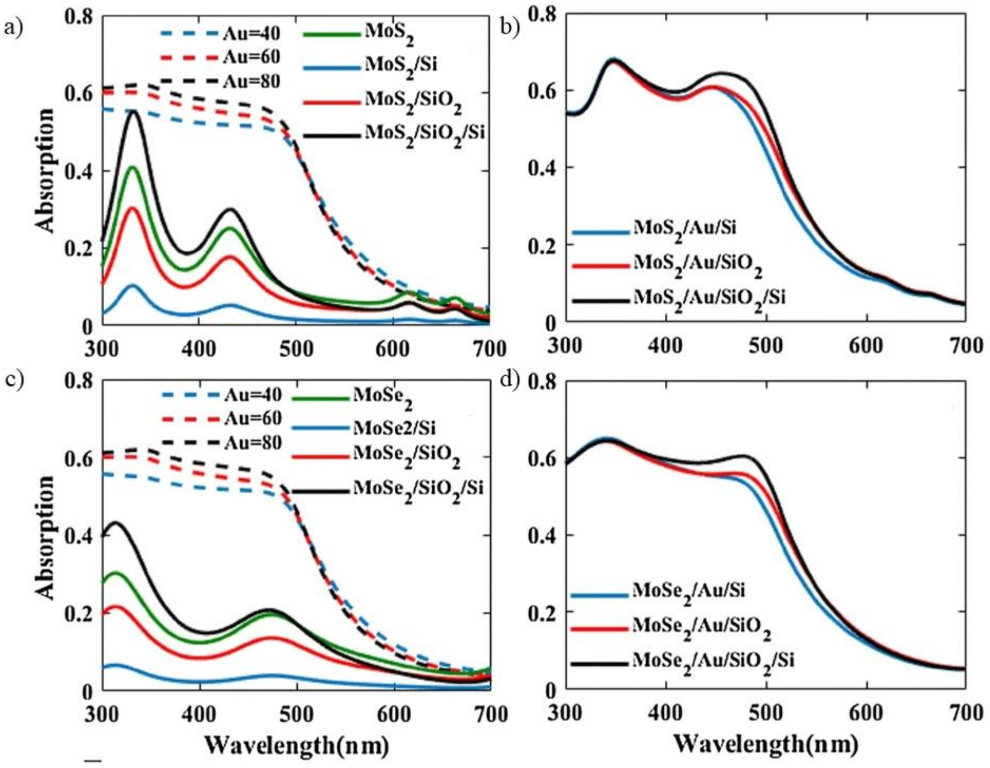

Fig. 1.4 a) Absorption spectra of various gold thicknesses, specifically 40 nm, 60 nm, and 80 nm (dashed lines), suspended TMDC (green line) and TMDC on three substrates of Si (blue line), SiO2 (red line) and SiO2 (50 nm)/Si (black line), for a) MoS2 and c) MoSe2. The gold layer is placed between the TMDC and the substrate for b) MoS2 and d) MoSe2 TMDCs. Reprinted from [38], with the permission of Springer Nature.

Overall, the absorption of TMDCs shows strong bound excitons, which confirm the strong Coulomb interaction. Furthermore, strong binding energies were also observed. It was shown that the binding energy for WSe_2 is 0.37 eV [40]. However, the presence of impurities can affect this value [41]. The theoretical prediction shows that the exciton binding energy for MoS_2 can be up to 1 eV [42], but the maximum reached experimental value so far is 0.57 eV [43].

TMDCs differ in their optical properties depending on their structure. For example, MoS_2 has a symmetric structure, hence it is characterised by optical isotropy, while ReS_2 has a 1T' phase, which means that its structure lacks symmetry. As a result, ReS_2 has anisotropic optical parameters [44]. Even in materials with a symmetrical structure, optical anisotropy can occur when, for example, it forms a heterostructure with another material. A. Shafi et al. [45] presented the anisotropic behaviour of a MoS_2 – AlGaAs nanowire heterostructure.

Different types of defects can be found in TMDCs, e.g. vacancies, ani-side, substitutional atoms and foreign adatoms, edge defects [46], [47]. Under electron beam irradiation, defects migrate and aggregate, creating line defects [47]. Defects may appear during bulk material growth. For example, chalcogen vacancies and inversion domains have been observed in synthesised CVT crystals [48]. However, CVT-grown crystals very often have structures with high spatial homogeneity, due to the high temperature and long growing time [49]. Furthermore, by changing the flow of sulphur vapour during CVT growth, it is possible to control the density of the sulphur vacancies, and hence, adjust the optical properties of the material.

Due to their wide bandgap and high on-off ratio, TMDCs hold promise for use in applications where graphene has proven inadequate. Nonetheless, low conductivity and carrier mobility may hinder their usefulness.

1.3 Phosphorene

Phosphorene is another 2D material consisting of phosphorus atoms. It fills the gap left by the previously mentioned materials combining their features - among other things, it has an even wider bandgap than TMDCs, and high on-off ratio and carrier mobility. Phosphorene was first synthesised in 2013 using the Scotch tape [7]. It has a puckered, honeycomb structure with two different directions – zigzag (ZZ) and armchair (AC) (shown in Fig. 1.5) [50]. Similar to the previously mentioned materials, the layers of phosphorus are bound by weak van der Waals forces, making them easy to separate [51].

For the purposes of this study, phosphorene is defined as a single layer while few-layer black phosphorus (FLBP) represents a multilayer material that shares similar properties with 2D materials. Materials with 25 or 30 layers and above are considered bulk materials.

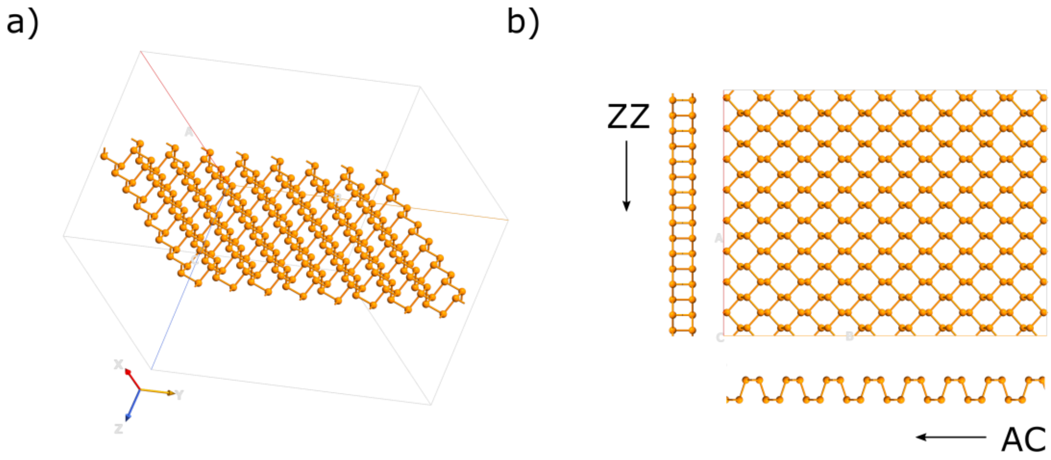

Fig. 1.5 a) Isometric and b) top and side views of atomic structure of phosphorene.

The bandgap of FLBP can be tuned from 0.3 eV for bulk, 1 eV for three-layer to ~2 eV for monolayer, which is a much wider range than that of graphene and TMDCs [52]. It highly depends on the number of layers, but also on the orientation direction. Phosphorene is also characterised by high mobility (up to $26 \cdot 10^3$ cm^2/Vs) and a high on-off ratio (up to 10^5 for monolayer) which is of great importance in electronic applications. A comparison of the parameters of all three mentioned 2D materials is shown in Table 1.1.

Table 1.1 Comparison of parameters of graphene, TMDCs and phosphorene.

	Graphene	TMDCs	Phosphorene
Bandgap	~0 eV	1-2 eV	0.3-2 eV
Carrier mobility	up to $10 \cdot 10^3$ cm^2/Vs [4]	200 cm^2/Vs [36]	$3.4 \cdot 10^3$-$26 \cdot 10^3$ cm^2/Vs [53]
On-off ratio	100	$1x10^8$ [36]	10^5
Refractive index	2.95 @633nm [54]		2.9 @650nm [55]

The optical and electrical properties of phosphorene are highly anisotropic, due to its asymmetry structure [8], [50]. This is especially noticeable during optical measurements. Photoluminescence is only visible in one direction (Fig. 1.6a), while absorption is the largest along the armchair direction and then decreases with the angle until the absorption is along the zig-zag direction, where is the smallest (Fig. 1.6b) [50], [56].

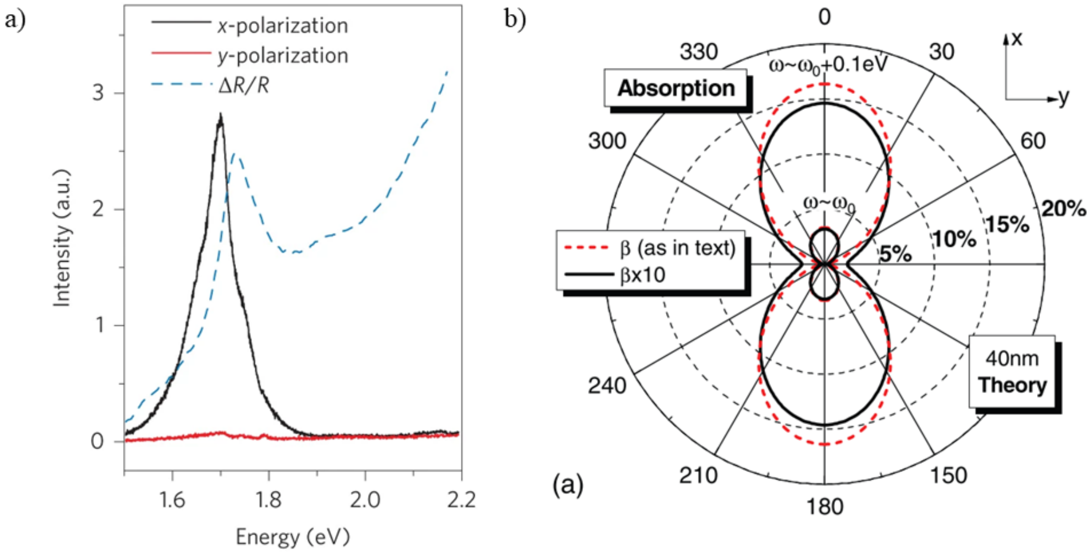

Fig. 1.6 a) Photoluminescence spectra of monolayer phosphorene. Reprinted from [50], with permission from Springer Nature. b) Absorption coefficient as a function of the light polarisation angle of a 40 nm BP film. Reprinted from [56].

The disadvantage of FLBP, which limits its application, is its fast degradation in air and water. After a short period of exposure to air, PxOy compounds were noted on the surface of FLBP [57], [58]. DFT calculation determined that oxygen dissociates on phosphorene, eventually forming an oxidised phosphorus layer. Then, PxOy compounds interacted with H_2O, leading to the formation of phosphoric acid [59]. These processes were also confirmed by experiments [57], [60]. A few different methods can be used to protect the phosphorene layer against degradation [61]. Creating an alloy of P and As is one of them. It not only protects the BP layer but also improves its parameters. Arsenic replaces some phosphorus atoms, forming black-AsP (b-AsP) with a similar structure that BP (Fig. 1.7) [62].

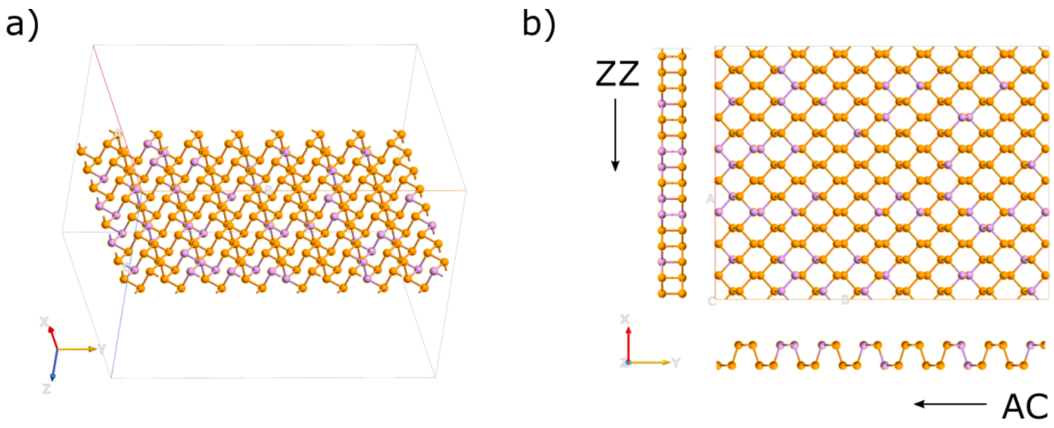

Fig. 1.7 a) Isometric and b) top and side views of atomic structure of b-AsP structure. The orange and purple balls represent P and As atoms, respectively.

The b-AsP is produced by the synthesis of red phosphorus with grey arsenic using the CVT-growth method. The obtained material has a much smaller range of bandgap than BP – between 0.15 and 0.3 eV [63], which makes it characterised by a wide response in the mid-infrared (mid-IR) range, which is promising in optical applications such as mid-IR photodetectors [64]. Furthermore, b-AsP, similar to BP, is optically anisotropic [65]. The more about protecting methods is described in section 2.4.

Chapter 2 presents more information about the optical and electrical parameters of FLBP, including its dichroism and birefringence properties, and the degradation process of BP flakes. Examples of BP applications in sensing devices are also presented.

1.4 Applications of two-dimensional materials

As was mentioned, 2D materials are characterised by unique optical and electrical parameters. Hence, the number of applications where they can be used is growing. Fig. 1.8 shows the scheme of example applications for graphene, TMDCs, and phosphorene.

Due to their small sizes and electrical properties, 2D materials are prominent candidates for future FETs. Hui Fang et al. built a field effect transistor (FET) with monolayer WSe_2 as the active channel. The resulting device was characterised by the high mobility (~250 cm^2/Vs) [66]. Other materials have also been used successfully in the construction of transistors, such as phosphorene [67], and MoS_2 [68]. Furthermore, transistors made of 2D materials are characterised by strong photoresponsibility [69]. A device based on MoS_2 can work in a broad spectral range with up to an 880 A/W photoresponse, making it an excellent photodetector [70]. Graphene, on the other hand, has ultrafast photonic response, however its almost zero bandgap contributes to a low photoresponsivity. To use graphene as a photodetector, Jinshui Miao et al. proposed a graphene/InAs heterojunction, thanks to which it was possible to increase the photoresponsivity from 0.1 mA/W to 0.5 A/W [71].

Because of the demand for miniaturised electronics products, there is also a need for micro energy storage devices. 2D materials have been found to be an excellent approach for this due to their unique electrical properties [72]. Bissets et al. compared the parameters of supercapacitors based on $MoSe_2$, WS_2, MoS_2 and TiS_2. Among them, the TiS_2 capacitor is characterised by the strongest capacitance. However, it easily oxides. In this case, N-methyl-2-pyrrolidone (NMP) leaves a layer on the surface, which also prevents the sample from oxidising

[73]. Graphene oxide ink was also found to be a great material to produce microcapacitors using 3D printing techniques. Chen et al. presented a device with capacitance up to 128 mF/cm^2 [74].

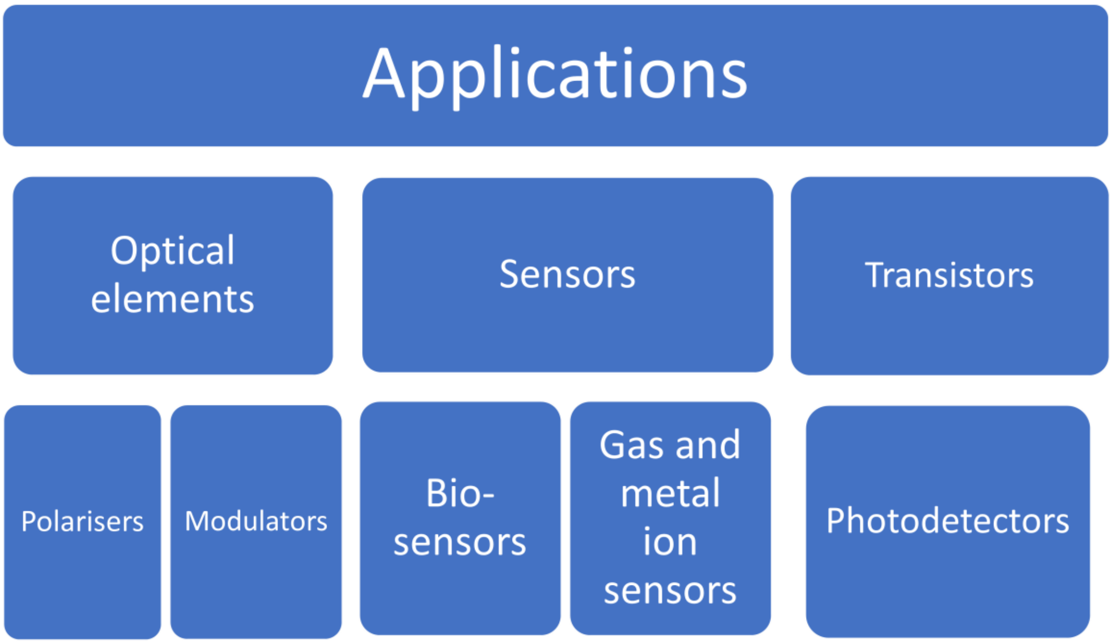

Fig. 1.8 Example applications for 2D materials.

Not only electronic but also optoelectronic and optical systems need smaller optical components. Lin et al. proposed a technique to produce flat lenses based on TMDCs [75]. They used a femtosecond laser to cut a pattern structure in the WSe$_2$ flake. The obtained lenses have concentric rings with tungsten oxide nanoparticles that strongly scatter light.

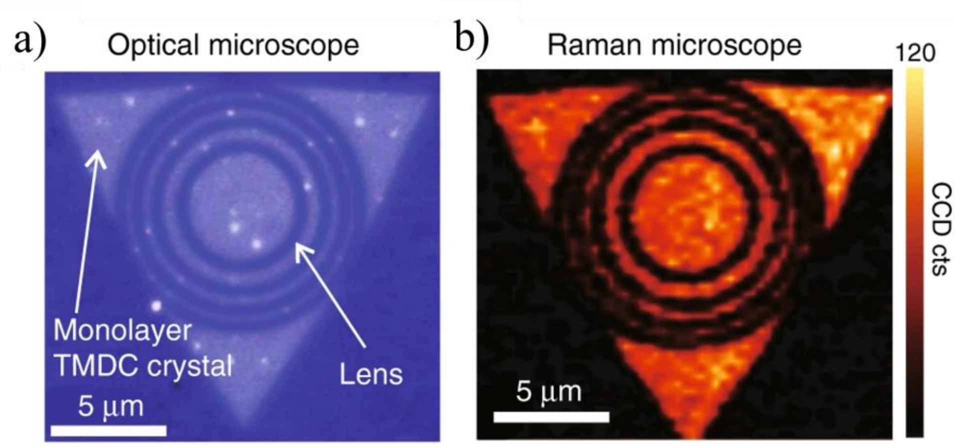

Fig. 1.9 a) Optical microscope image and b) Raman intensity image of WSe$_2$ lens. Reprinted from [75].

Optical and Raman microscope images of the WSe_2 lens are presented in Fig. 1.9a–b. It is possible to adjust the focusing properties of lenses by controlling the radius and number of rings.

Other optical components that can be made from 2D materials are a polariser and a phase retarder. FLBP's optical absorption allows it to absorb light polarised in one direction while remaining transparent to light polarised in another direction. This means that FLBP can work as a linear polariser [52]. Lee et al. also presented a phase retarder based on a 488 nm thick BP flake [76]. The polarisation intensity of light in the input and after passing through BP as a function of the analyser angle is compared in Fig. 1.10. The results show the phase retardation of the transmitted light.

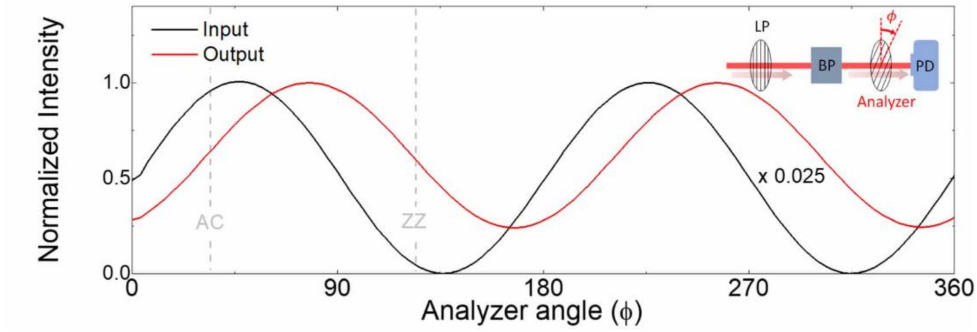

Fig. 1.10 Input light at 630 nm and that of the output after passing through a 488 nm thick BP flake. Reprinted from [76].

Numerous studies have been carried out on 2D materials working as a saturable absorber or a modulator [77]. In 2009, Bao et al. presented graphene as a saturable absorber for the first time [78]. A mode-locked fibre laser with a central wavelength at 1,565 nm working with graphene was capable of generating pulses with a width of 756 fs. In 2015, Sotor et al. discovered that a thulium-doped fibre laser with FLBP as a saturable absorber was able to form pulses at 1,910 nm with a width of 739 fs [79]. Phosphorene was also found to be a great electro-optic modulator [80]. After applying the electric field, the BP's absorption in the mid-IR range shifted.

Due to their properties, 2D materials are also promising in sensing applications. They can detect many different gases, such as humidity, NO_2, NH_3, and CO [9], [81]. To accomplish this, one employs, for example, changes in resistivity or conductance as a reaction to the adsorption of gas molecules. Furthermore, 2D material-based sensors have the potential to absorb or detect metal ions [82], [83]. This is especially important because an overabundance of metal ions in the environment can cause harm to both nature and human health [84], [85]. The next group of sensors that can be based on 2D materials is biosensors [86]. For example, a graphene FET can detect glucose and glutamate with a limit of detection (LoD) 0.1 mM and 5 μM, respectively [87]. Yew et al. have shown a fluorescent sensor based on BP nanoparticles to detect DNA with a sensitivity of 10^{-7} M [88].

In conclusion, 2D materials such as graphene and TMDCs have been the subject of increasing interest and research due to their unique properties and potential applications in various fields, including optics, sensing and electronics. Graphene, for example, exhibits high carrier mobility but almost zero bandgap, whereas TMDCs are characterised by a high on-off ratio and bandgap within the range of 1–2 eV. Phosphorene, on the other hand, has bandgap that can be tuned in a much wider range – from 0.3 to 2 eV. Furthermore, due to its structure, it is characterised by strong anisotropy, which could be advantageous for optical and optoelectronic applications. More about the properties and applications of phosphorene will be presented and discussed in chapter 2.

Chapter 2. Few-layer black phosphorus – optoelectronic properties and applications

Phosphorus is a chemical element that has been known for many years. Its compounds are used in many fields, such as electronics, optoelectronics and medicine. Phosphorus compounds are used, for example, as electrical contacts, in fuel cells and as cathodes in rechargeable lithium-ion batteries. The compounds Ga(AsxP1-x) and GayIn1-yAsxP1-x have been used in LEDs since the 1960s [89].

2.1 Allotropes of phosphorus

Pristine phosphorus was first obtained in 1669 and has four allotropes – white, red, blue, and black. White phosphorus is the most reactive allotrope due to its molecular form with four atoms in a tetrahedral structure. It is also very toxic. Heating white phosphorus yields red phosphorus, which exists in an amorphous state. Red phosphorus is less reactive than the white form. Blue and black phosphorus (BP) are crystals and are the most stable allotropes. A comparison of their allotropic parameters is given in Table 2.1.

Table 2.1 Comparison of all allotropes of phosphorus

Properties	White phosphorus	Red phosphorus	Blue Phosphorus	Black Phosphorus
Colour	Translucent waxy solid	Red	–	Black
Reactivity	Most reactive	Moderate reactive	Least reactive	Least reactive
Chemical structure	P4 molecules	Polymeric network	Crystalline form	Crystalline or amorphous form

The crystalline form of BP was obtained in 1914 from white phosphorus at a pressure of 1.2 GPa and a temperature of 200°C [90]. BP has a multilayer structure in which each layer is held together by weak van der Waals forces, making it easy to obtain a two-dimensional shape.

2.2 Preparation and characterisation of few-layer black phosphorus

Currently, there are a few types of exfoliation methods, such as mechanical or liquid exfoliation and chemical vapour deposition (shown in Fig. 2.1). Mechanical exfoliation usually involves the use of the Scotch tape to produce single flakes with a few atomic layers. It is a simple and inexpensive method but has some disadvantages. Traces of adhesive remain on the substrate and the concentration of flakes is low. Therefore, Castellanos-Gomez et al. proposed using polydimethylsiloxane (PDMS) in addition to the adhesive tape to create a bilayer phosphorene. This will increase the concentration of flakes and reduce contamination on the substrate [51].

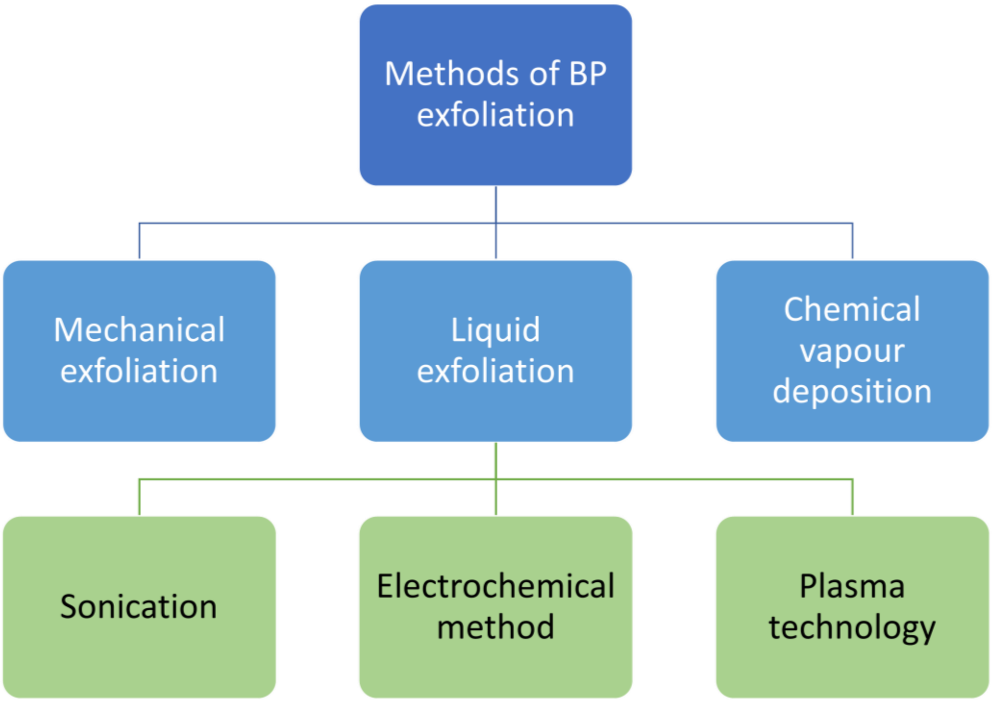

Fig. 2.1 Classification of methods of BP exfoliation.

In liquid exfoliation, the bulk the BP is immersed in a solvent and sonicated for as long as mono- (ML) and few-layers (FL) flakes are obtained. This method is more repeatable than mechanical exfoliation and it is possible to obtain bigger flakes. However, it is still hard to get flakes of the same size every time. The choice of solvent is very important in obtaining stable exfoliation conditions. It was showed that using sonication in NMP can produce FLBP that is stable in water. Furthermore, flakes of various sizes are obtained during the exfoliation process. Only the use of centrifugation with appropriately selected time and speed produces flakes of similar dimensions [91].

Electrochemical methods are also used to obtain ML and FL BP. Bulk BP is used as a working electrode, and Pt foil or graphite can be used as a counter electrode [92], [93]. After applying the voltage, the flow of the charge causes the phosphorus layers to tear. A comparison of the XPS survey spectra of bulk BP and exfoliated BP is presented in Fig. 2.2. Fig. 2.2a shows phosphorus (P), but also other atoms that contaminate the sample. During synthesis, BP becomes contaminated with tin [93]. Exfoliated BP also contains copper and carbon, which come from sample and specimen holders [93]. In Fig. 2.2b, high-resolution XPS are shown. A high peak, representing phosphorus oxide, is visible in the exfoliated BP, which confirms the instability of FLBP in the air [60], [93].

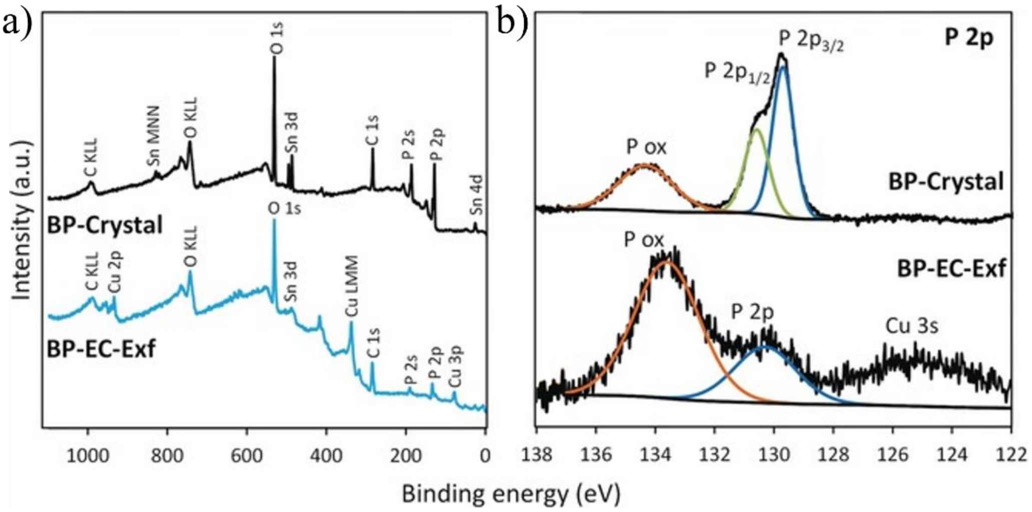

Fig. 2.2 a) XPS spectra of bulk BP (black) and electrochemically exfoliated BP (blue). b) High-resolution XPS spectra of the P 2p signal for bulk BP and electrochemically exfoliated BP. Reprinted from [93], with the permission of John Wiley and Sons.

Despite its many advantages, sonication and electrochemical exfoliation take a relatively long time (~2 hours). Huang et al. proposed plasma-liquid technology as a method to obtain large flakes of FLBP of good quality in just 5 minutes [94]. To avoid oxidation, the process was carried out in pure N,N-dimethylformamide (DMF). Bulk BP was used as a cathode and a stainless steel needle as the anode. After applying a high voltage, the process of exfoliation starts almost immediately. High-resolution mass spectroscopy (HRMS), transmission electron microscopy, optical microscopy, atomic force microscopy (AFM) and Raman spectroscopy were used to confirm the success of the exfoliation and obtaining good-quality material.

CVD is capable of growing thin layers of materials over a relatively large area compared to the previously mentioned methods. In addition, by controlling the CVD parameters, samples of similar quality can be obtained each time [95]. Smith et al. reported the synthesis of FLBP from red phosphorus directly on a silicon substrate using the CVD technique [96]. The films obtained had around four layers and had an average area of 4 μm^2. The CVD approach was also used to grow FLBP films on conductive carbon paper [97]. The red phosphorus was brought to a high temperature and thermal vapour deposition gave was used to deposit FLBP on the carbon substrate. The resulting material was then used as an anode in lithium-ion batteries.

The exfoliation method will affect the parameters of the resulting material, as a single flake will have slightly different properties than a layer composed of many differently oriented flakes. Therefore, the choice of exfoliation method must also depend on the application of the obtained material.

2.3 Optical and electrical parameters

As was mentioned in the chapter 1, BP’s structure has two different orientations – AC and ZZ [50]. This results in a high anisotropy of the electrical and optical properties of the material. Han Liu et al. studied the electrical parameters of mechanically exfoliated 10 nm-thick FLBP deposited on a Si substrate with metal contacts added every 45°. The electrical transport showed a sinusoidal dependence on the crystal’s orientation [7]. The optical responses also behave differently for both BP directions, showing strong linear dichroism [50], [98]. For the monolayer, the first absorption peak is at 1.55 eV in the AC direction, which is close to the BP bandgap. However, due to the mirror symmetry, peaks near the bandgap are forbidden for absorption in the ZZ direction [8]. This is shown in Fig. 2.3. The first absorption peaks in the AC direction change with the increasing layer number according to the BP bandgap value (Fig. 2.3a). The absorbance in the ZZ direction also shifts (Fig. 2.3b), but not so significantly. The same results were obtained in the DFT calculation [52].

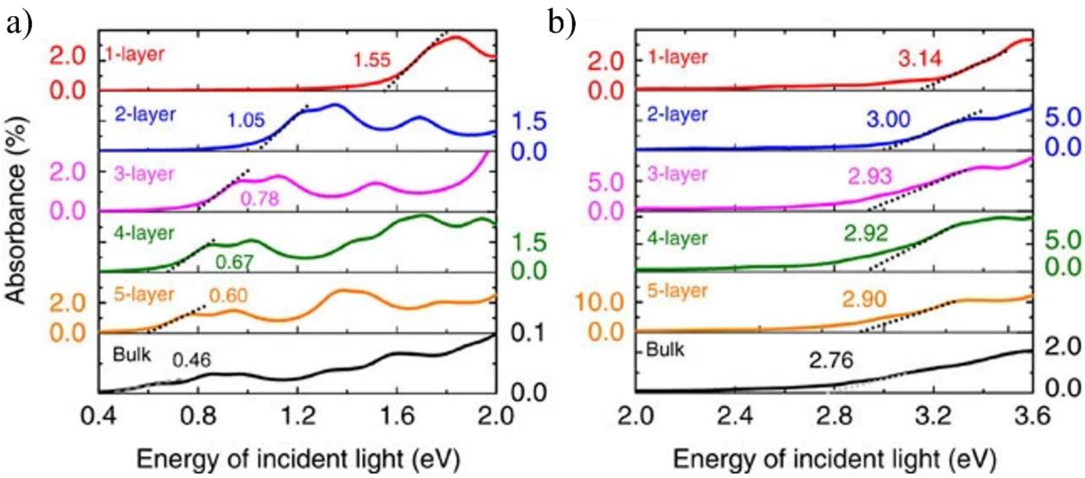

Fig. 2.3 Absorbance spectra for 1–5 layers and bulk BP among a) AC direction and b) ZZ direction. Reprinted from [8].

The layered puckered structure with strong layer interaction also causes a strong dependence of the FLBP bandgap on the thickness, as was shown in Fig. 2.4. The bandgap changes from 0.3 eV for bulk to ~2 eV for monolayer but always remains direct [52].

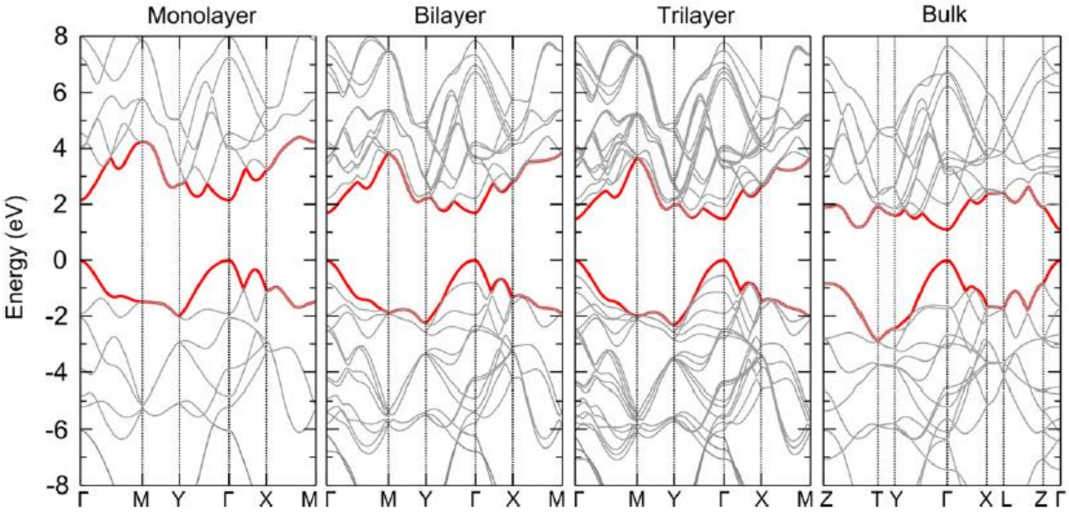

Fig. 2.4 Band structure for mono-, bi-, trilayer and bulk BP. Reprinted from [51], with the permission of IOP Publishing.

All electrical parameters of the FLBP are affected by the tuning bandgap. The carrier mobility changes as a function of both thickness and crystal orientation [8]. For monolayer BP, the difference in mobility for both directions is more significant than for few-layer samples. The mobility of the holes reaches up to 700 cm^2/Vs for the zig-zag direction and even 26,000 cm^2/Vs for the armchair direction, which are much higher values than the electron mobility (~80 and ~1,100 cm^2/Vs for the zig-zag and armchair, respectively) [8], [99]. Such values are lower than for graphene but higher than for TMDCs, as was shown in Table 1.1 in Section 1.3. The carrier mobility together with the high on-off ratio (up to 10^5) distinguishes FLBP among other 2D materials.

The optical properties of BP show excitonic effects. This is most noticeable for monolayer samples, where the screening is much smaller and the excitonic binding energy can reach 900 meV for free-standing BP [71]. For samples deposited on SiO_2/Si, the additional screening by a substrate must be taken into account as it causes the binding energy to decrease to 0.3 eV [52]. The difference between the electrical bandgap and the binding energy is the optical bandgap, which can be determined by analysing the absorption spectra.

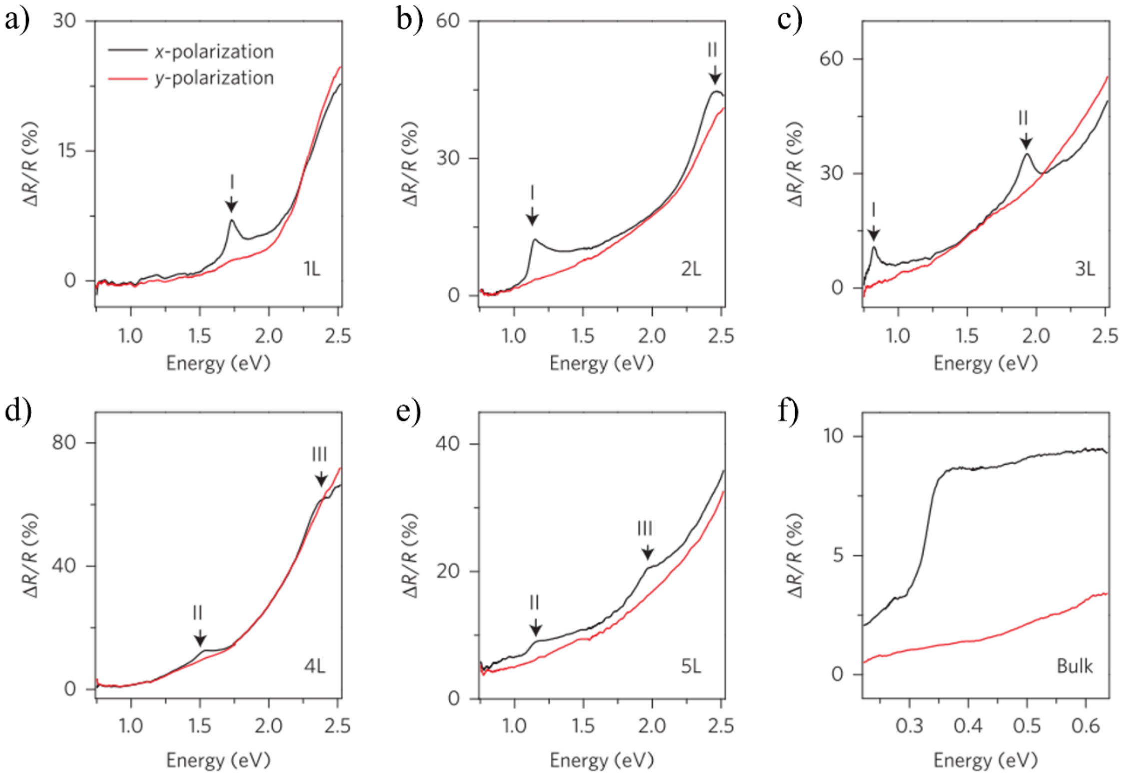

Fig. 2.5 Reflection spectra of a) monolayer, b) bilayer, c) trilayer, d) tetralayer, e) pentalayer, and f) bulk BP for AC (x-polarisation) and ZZ (y-polarisation). Reprinted from [50], with permission from Springer Nature.

Fig. 2.5 shows the reflection spectra for 1L–5L and bulk BP. The first peaks, marked as I, describe the position of the optical bandgap, which are 1.73, 1.15, 0.83, and below 0.75 eV for mono-, bi-, trilayer and below, respectively [50]. At the same time, these values can be assigned to the lowest-exciton transition energy. Therefore, there are no peaks in the absorption spectra below these values. In addition, the resonances above the bandgap (marked as II and III in Fig. 2.5) come from transitions on the successive subbands [50], [98].

The optical absorption can also provide information about the stability of the FLBP. By checking its change, it was possible to conclude that liquid exfoliated FLBP in DMF is stable under ambient condition for 5 days [94].

On the other hand, the absorption spectrum depends on the type of the BP sample and the exfoliation method used. The general trends show a decreasing absorption for longer wavelengths that 400 nm [100], [101]. Guo et al. presented FLBP exfoliated by sonication in NMP solution, which is characterised by three absorption peaks at 310 nm, 380 nm, and 470 nm [100]. Furthermore, the absorption spectra for BP quantum dots (BPQD) have only one peak – at ~300 nm [101]. However, it was shifted to higher wavelengths when the BPQD surface was modified with PEG [102]. Above 600 nm, the absorption is rather featureless, as can be seen from the excitation coefficient curve in Fig. 2.6 [76]. In addition, the absorption for the ZZ direction is much lower than that for the AC direction.

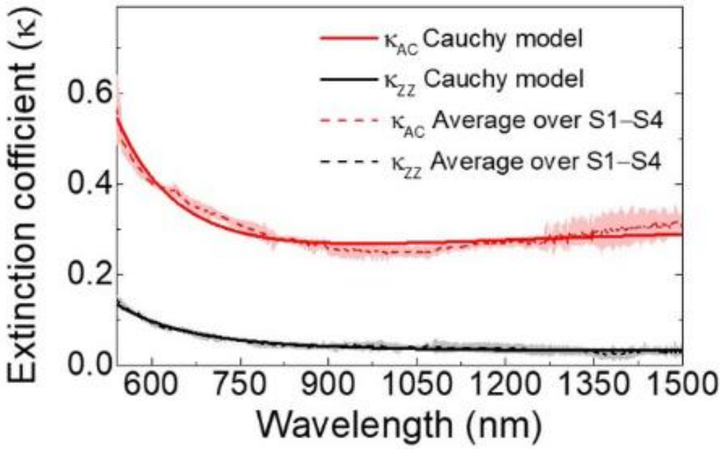

Fig. 2.6 Extinction coefficient of BP for the AC (red) and ZZ (black) direction. Reprinted from [76], with the permission of IOP Publishing.

The Raman spectra of the MLBP consists of three peaks at ~362 cm^{-1}, ~439 cm^{-1} and ~468 cm^{-1}, corresponding to the A_g^1, B_{2g}, and A_g^2 vibrational modes, respectively. The peaks are strain [103] and thickness [104] dependent. Guo et al. described how the Raman spectra changed with increasing the number of BP layers [100]. Raman spectra and for bulk and 1–4 layer BP are presented in Fig. 2.7a. The dependence between the vibrational peaks and the layer number of the FLBP is shown in Fig. 2.7b. Raman spectroscopy can be useful in determining the number of layers for BP samples. In a monolayer, atoms can vibrate freely, but when another layer is added, the vdW forces hinder the oscillation [105]. This results in a shift of the BP peaks. However, the largest change is between mono- and bilayer BP, and for samples thicker than 5 layers, the shift is not noticeable [51]. For samples exfoliated on a silicon substrate, it has been shown that the thickness can be determined with an accuracy of 1–2 nm by measuring the ratio of the Ag^1 peak and the silicon peak [51]. The variation of this ratio with increasing thickness is shown in Fig. 2.7c.

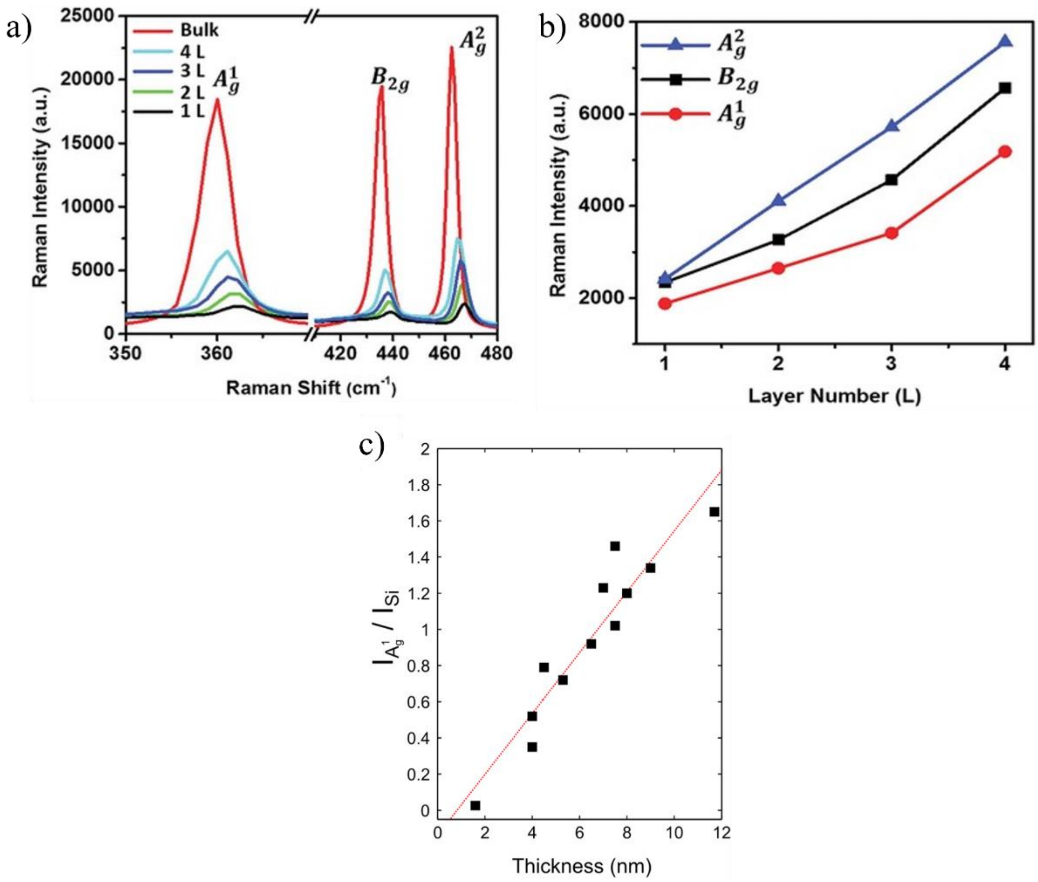

Fig. 2.7 a) Raman spectra of bulk and 1–4L BP, b) layer-dependence of the BP vibrational peaks, c) thickness-dependence of the ratio between A_g^1 mode and silicon peak. Figures a and b was reprinted from [100] with the permission of John Wiley and Sons; Figure c was reprinted from [51], with the permission of IOP Publishing.

The Raman spectrum of phosphorene also strongly depends on the polarisation of the incident light [104]. More about this is discussed in Section 2.3.

Another technique used to characterise BP is photoluminescence (PL). The PL spectra of FLBP also depend on the number of layers [106]. Fig. 2.8 shows the PL characteristics for 1–5 layer-BP. The occurrence of PL peaks is determined by the optical bandgap, which changes with the BP thickness, as was mentioned earlier in this section. However, the difference between the energy peaks for thicker samples, e.g. between 30 nm and 46 nm, is almost imperceptible [107]. This limits the use of the PL technique to determining the thickness of BP to only a few layers.

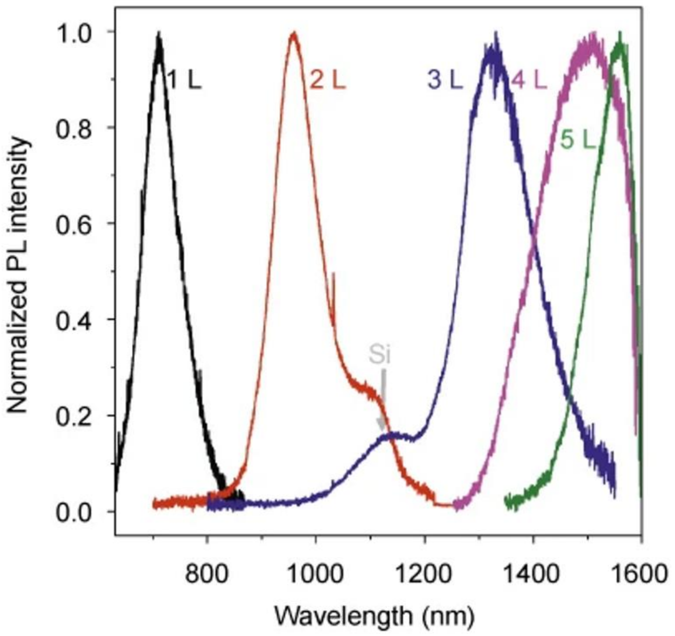

Fig. 2.8 Photoluminescence spectra of 1–5 layer-BP. Reprinted from [106].

The exciton binding energy of phosphorene decreases with the number of layers, reaching 940 meV for monolayer, 160 meV for bilayer, and 110 meV for trilayer [108]. It means that the excitonic effect dominates in the PL spectra of FLBP, even at room temperature. However, the used substrate or encapsulation layers reduce the BP binding energy [109], [110].

In summary, the bandgap of BP is dependent on the number of layers, which consequently affects its optical and electrical properties. UV-VIS spectrometry, Raman spectrometry and PL techniques can be used to study the optical properties of BPs and indirectly determine the thickness of the thin film under study [50], [105], [106]. However, studies focusing on determining the optical constants of BPs, which include the refractive index and extinction coefficient, are rare. Especially if not a single flake is studied, but a layer composed of multiple BP flakes, which may be oriented differently.

2.4 Degradation of few-layer black phosphorus

FLPB is found to degrade upon exposure to ambient conditions. The DFT was calculated to check the interaction between phosphorene and oxide, and phosphorene and water. The results show that, due to the lone pair of electrons left in each phosphorus atom, oxide and phosphorene can react and form a phosphoric oxide layer [59]. In theoretical studies, it was also confirmed that, after dissociation, the atomic oxygen prefers the dangling position [111]. In the interaction of water with phosphorene, the configuration where hydrogen atoms are closest to the BP surface is the most stable one. The hydrogen tends to be near the lone pairs of electrons in phosphorus atoms. The binding energy for water on the BP surface was found to be larger than for H_2O on graphene (180 meV and up to 120 meV, respectively) [59], [112]. However, the DFT calculation shows that water does not interact strongly with FLBP [59]. It prefers to use the hydrogen bond to connect with the surface. Therefore, a layer of FLBP with oxide must be taken into consideration. The phosphoric oxide reacts strongly with water, which was confirmed by a decrease in the endothermic energy. Moreover, according to the DFT calculation, the bilayer structure seems more stable because water molecules only bond with the upper layer [51].

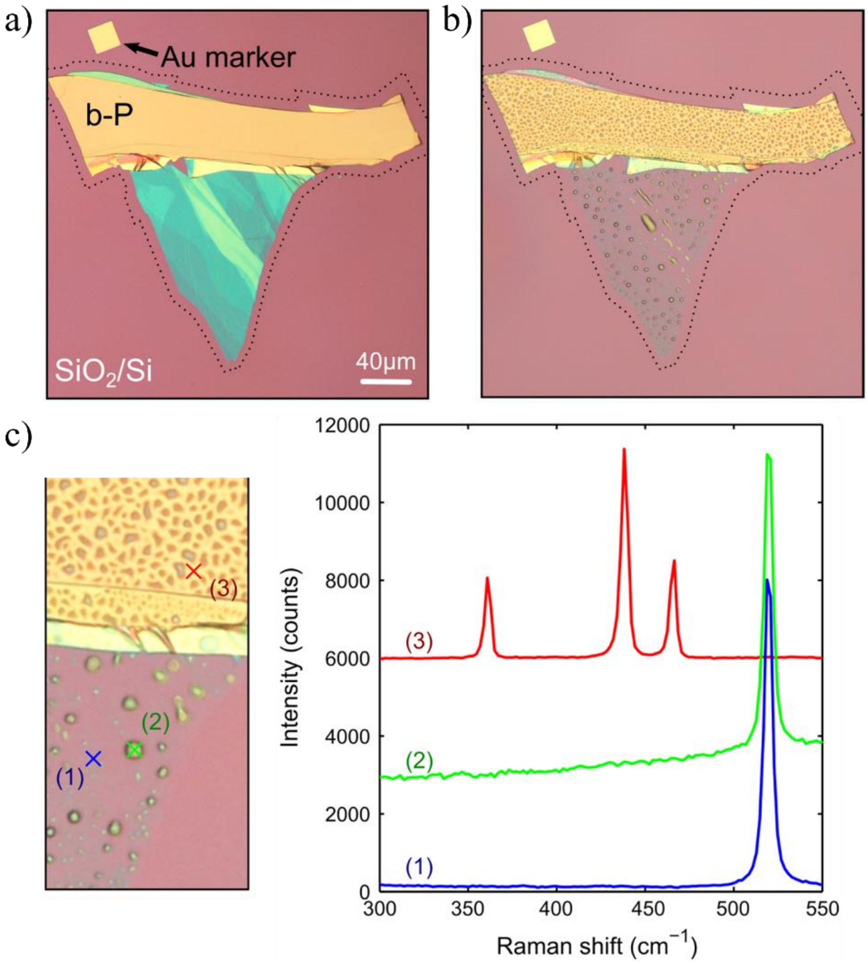

Fig. 2.9 BP flake on a SiO_2/Si substrate a) right after transfer b) after two weeks kept under air. c) Raman spectra for the BP flake in b) at the three points marked in the image on the left. Reprinted from [51], with the permission of IOP Publishing.

Experiments and DFT calculations show that the degradation process starts almost immediately when the sample is exposed to the air [57], [59]. Castellanos et al. present mechanically exfoliated FLBP [51]. After one hour under ambient conditions, droplets start to be visible on the sample surface.

Longer exposure to the air causes complete degradation of the FLBP [51]. Fig. 2.9a shows the sample after exfoliation and after 2 weeks of exposure to the air. The thinnest parts are gone. Fig. 2.9c shows Raman characteristics for different positions on the sample (show on Fig. 2.9b) after two weeks exposed to the air. The Raman spectrum for the point marked as (3) contains all three peaks characteristic of phosphorene. This shows that thicker flakes are more stable under ambient conditions.

The oxidation process can be observed by the A_g^1/ A_g^2 ratio from the Raman spectra [113]. Fig. 2.10 shows how the A_g^1/ A_g^2 ratio change in time the high-ratio region (HRR; Fig. 2.10a) and the low-ratio region (LRR; Fig. 2.10b). HRR and LRR reflected a different crystal orientation of the FLBP. For both orientations of the sample, the A_g^1/ A_g^2 ratio decreases during the oxidation process [113].

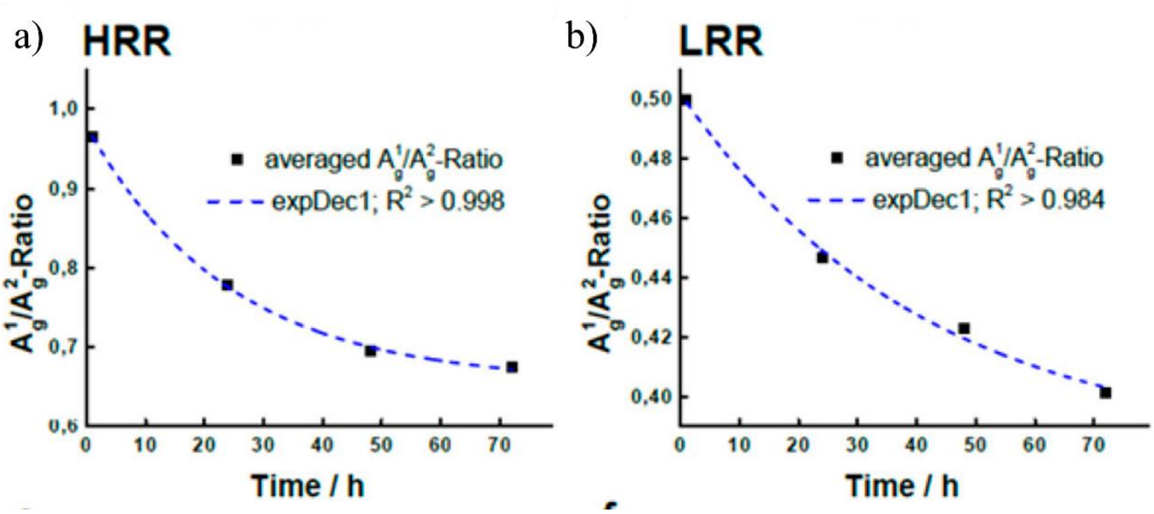

Fig. 2.10 Change of A_g^1/A_g^2 intensity ratio for a) high ratio (HRR) and b) low ratio (LRR) region. Reprinted from [113].

Exposure to light enhances the oxidation of FLBP. Under the illumination of light from a 150 W halogen lamp, the degradation process for a 5 nm thick BP sample is more than 3 times faster compared to an unilluminated sample [113]. For another BP sample illuminated by light with wavelength 532 nm, Raman spectra were collected after 24, 48, 96, and 120 minutes after exfoliation. The intensity of the A_g^1, B_{2g} and A_g^2 peaks successively decreased, reaching almost zero, as was shown in Fig. 2.11 [60].

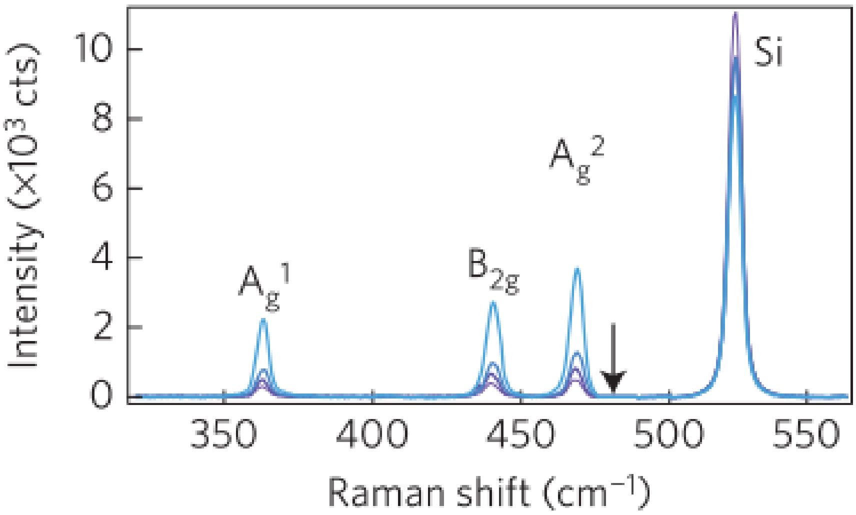

Fig. 2.11 Raman spectra at 532 nm on 5 nm thick FLBP at 24, 48, 96 and 120 min after exfoliation. Reprinted from [60], with the permission of Springer Nature.

The absorbance measurements can give us information about the BP degradation. Especially changes in the phosphoric acid concentration can be easily determined by examining the absorption at 710 nm. The three BP samples were functionalised by (3-aminopropyl)trimethoxysilane (AMPTS), trichloro(dodecyl)silane, (DDTS) and 1H,1H,2H,2H-perfluorooctyltrichlorosilane (PFDTS) [114]. A comparison of the absorbance at 710 nm for pure FLBP, FLBP/AMPTS, FLBP/DDTS and FLBP/PFDTS is shown in Fig. 2.12. As can be seen, the absorbance of the pure FLBP and FLBP/AMPTS increases much faster than for the others, which means these samples degrade faster.

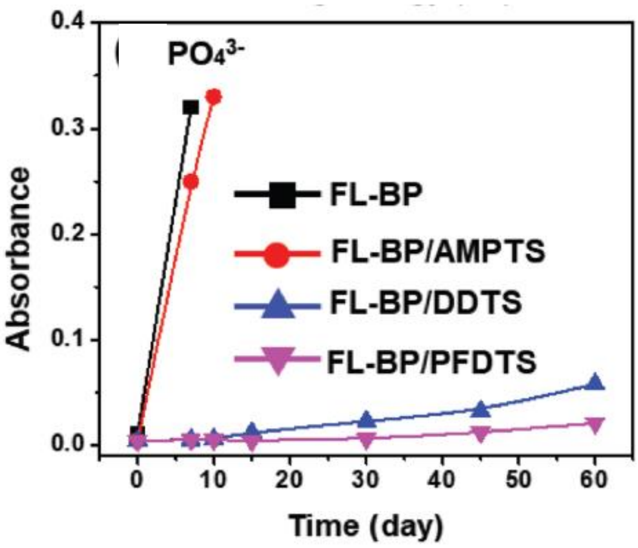

Fig. 2.12 Absorbance at 710 nm for FLBP, and FLBP functionalised by AMPTS, DDTA and PFDTS. Reprinted from [114].

A few different methods can be used to protect the phosphorene layer against degradation [61]. They can be divided into chemical and physical encapsulation, functionalisation, and alloying. The classification was shown in Fig. 2.13.

The chemical encapsulation method is, for example, creation of a metal ion passivation layer. Mixing BP and $AlCl_3$ in ethanol forms an Al^{3+} ion layer on the top of the BP structure. The ions combine with free electrons at the surface, dramatically reducing the reactivity of BP [115].

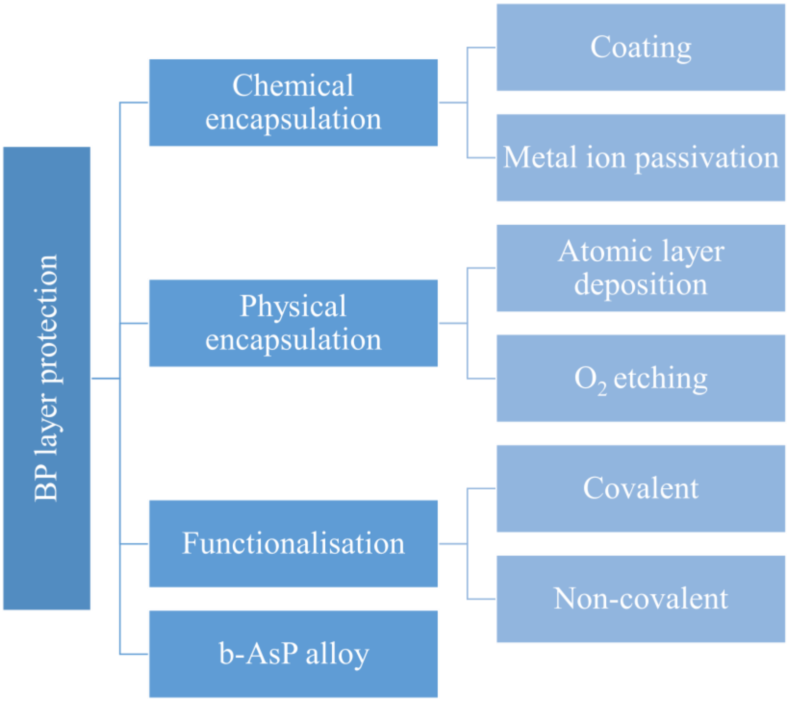

Fig. 2.13 Classification of methods of protecting the BP layer against degradation.

Physical encapsulation methods can include the atomic layer deposition (ALD) technique and the O_2 etching process. AlO_x compound has been shown to be effective as a passivation layer. However, the ALD process, during which the AlOx layer is deposited, can affect the phosphorene structure. Pei et al. produced mono- and bi-layer phosphorene by O_2 plasma etching. At the start of the process, the top layer of mechanically obtained FLBP is etched and forms on the surface of PxOy (Fig. 2.14 a–b). Further etching increases the oxide layer and decreases the thickness of the BP (Fig. 2.14c). At the end, the Al_2O_3 layer was deposited using the ALD technique (Fig. 2.14d). This method also makes it possible to control the number of defects introduced into the structure and so tunes the photon emission range. Oxide on the surface increases the time it takes for the sample to degrade, but it is still quite a short time [91]. To prevent that, the ALD AlOx layer is used. The PxOy layer on the surface protected the BP against further oxidation during the ALD process [57].

The functionalisation methods can be divided into two types: covalent and noncovalent. Covalent methods include, for example, functionalisation with diazonium salt, organolithium compounds or benzoic acid [116]–[118]. The spontaneous modification of FLBP by diazonium molecules not only provides greater stability under ambient conditions but also enhances the on/off ratio [119]. 1H,1H,2H,2H-perfluorooctyltrichlorosilane (PFDTS) reacts with phosphoric oxide on the FLBP surface, forming a protective layer against water and organic solvents [114]. On the other hand, noncovalent functionalisation of FLBP with 1,4-diamine-9,10-anthraquinone was used to design an electrode for detecting ascorbic acid [120].

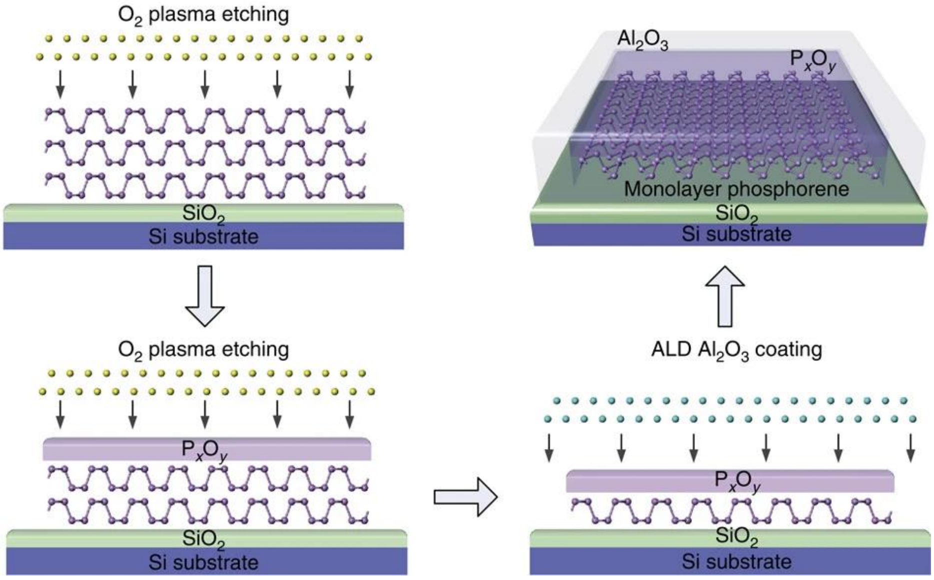

Fig. 2.14 Scheme for the fabrication of very mono- or few-layers phosphorene covered with an Al_2O_3 layer using plasma oxidation and atomic layer deposition.
Reprinted from [91].

The oxidation process of FLBP starts immediately when the BP layer is exposed to air. This affects the FLBP's properties, hence, the degradation process can be studied by various methods such as Raman spectroscopy and absorbance measurement. However, rapid degradation may limit the number of FLBP applications.

2.5 Dichroism and birefringence in few-layer black phosphorus

Optically anisotropic materials, that is, materials in which light propagation depends on the orientation of the material, are characterised by optical dichroism or birefringence. A dichroism is a dependence of the optical absorption on the light polarisation [121]. Two types can be designated: circular and linear. In circular dichroism, absorption varies with circular polarisation. However, this phenomenon is associated with optical activity. Linear dichroism is different absorptions of polarised light in parallel and perpendicular orientations and is related to the anisotropic structure of the material [121]. Materials characterised by optical dichroism are used in, for example, wavelength converters [122], dichroic colour filters [123] and polarisers [124]. Birefringence materials, on the other hand, have a refractive index dependent on the polarisation and propagation direction of light [125].

Currently, the interest in 2D materials in polarisation applications is growing. Due to their small dimensions, they can replace bulk materials by miniaturising optical devices. Some TMDCs are characterised by dichroism. The optical response of palladium diselenide ($PbSe_2$) was measured by polarisation-sensitive Raman spectroscopy and polarised absorption spectroscopy [126]. Anisotropic behaviour from the UV to VIS range was determined. In turn, germanium arsenic (GeAs) is characterised by a high dichroic ratio (~1.49 at 520 nm, and even 4.4 at 830 nm) [127]. Moreover, a photodetector based on this material not only shows a great polarisation-dependent photoresponse but also an excellent on/off ratio.

Dichroism or birefringence can also be induced by applying strain to the material [128]. Oliva-Leyva et al. have presented the influence of strain on the dichroism and absorption characteristic of graphene. They proved that determining the polarisation from only two transmittance measurements is needed to reconstruct the applied strain [128].

Phosphorene exhibits natural optical anisotropy due to its crystal structure [8]. Linear polarised light passing through a BP flake becomes elliptically polarised. However, the strongest polarisation properties can be observed for one or few-layer BP films. Weaker birefringence has been shown even for 6-layer BP because of the higher transition of quantum-well subbands [129]. But it is still much higher than for most TMDCs, e.g. rhenium disulfide (ReS2) and rhenium diselenide (ReSe2) and is comparable with the birefringence of commercially available bulk materials [130].

The polarisation properties in BP not only depend on the thickness but also on the presence of an electric field. Biswas et al. built a Fabry-Perot cavity based on tri-layer BP and demonstrated that optical dichroism in BP can be electrically tuned (Fig. 2.15) [129].

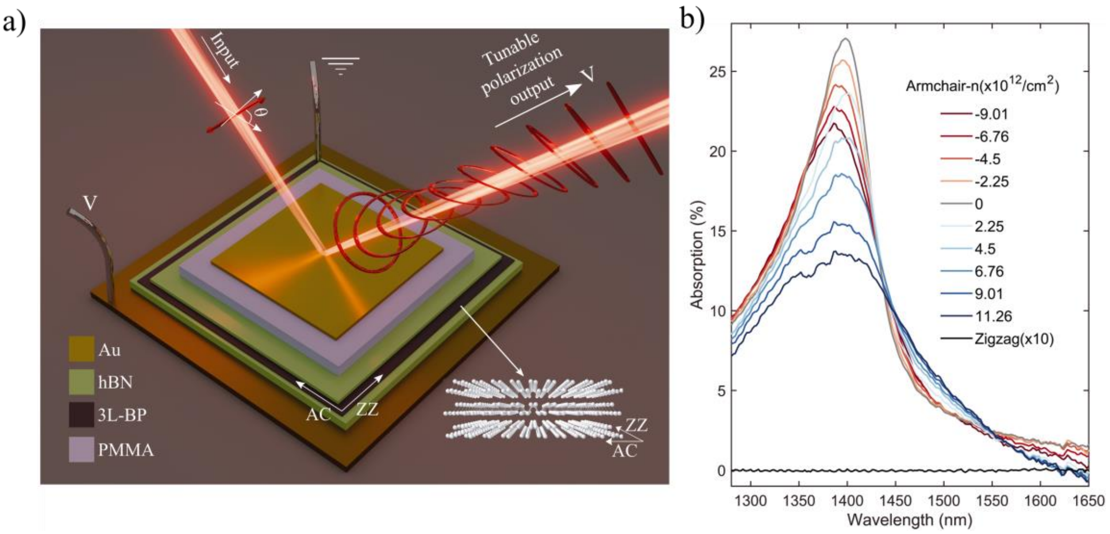

Fig. 2.15 a) Scheme of a Fabry-Perot cavity with 4 layers – hexagonal boron nitride, tri-layer BP, hexagonal boron nitride and gold. b) Polarised absorption from a Fabry-Perot cavity based on tri-layer BP for different doping electrons and holes along the AC direction. Reprinted from [129].

Not only birefringence but also linear dichroism was observed in FLBP. Transmittance in the AC direction was found to be much smaller than that of the ZZ direction [76]. Furthermore, the anisotropic effect in FLBP can be observed across a very broadband range – from VIS to IR [52], [131].

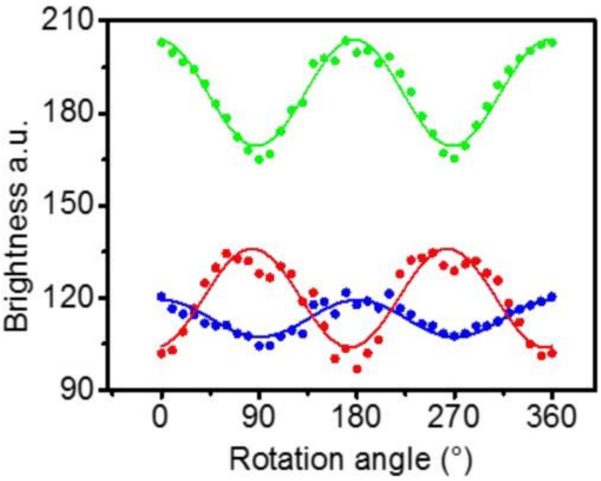

Fig. 2.16 Brightness of the reflected light from a thick BP as a function of the rotation angle from three RGB channels. Reprinted from [131]. Copyright 2016 American Chemical Society.

Mao et al. [131] presented measurements of mechanically exfoliated FLBP using polarisation microscopy with a dichroic beamsplitter. The results showed the dependence between brightness and crystalline directions in the visible range (Fig. 2.16).

The optical anisotropy of FLBP can be tuned by strain, changing the substrate or layer thickness [132]. The Raman modes in BP's response shifted when FLBP is applied under strain [133]. Moreover, the modes reacted differently when strain was applied in different directions, with the B_{2g} mode showing high sensitivity to ZZ strain.

In conclusion, FLBP is defined by its crystal structure, which leads to its strong birefringence and dichroism. It was already reported that BP's optical anisotropy is stronger than in other 2D materials, however, the anisotropic phenomenon diminishes as the BP layer thickness increases. This presents opportunities for using FLBP in polarisation devices, such as photodetectors and polarisers.

2.6 Few-layer black phosphorus as a sensor device

A number of studies have focused on the chemical properties of FLBP and their interaction with other substances. In fact, phosphorene was found an excellent material to detect various gas molecules, humidity, metal ions, and many more. The methods of sensing can be divided into fibre sensing, FET devices, forming of a composite of BP with another material, and fluorescence sensor.

Liu et al. presented an integrated tilted fibre grating (ITFG) configuration based on BP [10]. The device was then used to detect lead ions with a lower LoD at 0.25 ppb. With an increasing concentration of ions, the transmission in the fibre decreased. Furthermore, a theoretical study of BP used in a fibre optic surface plasmon resonance (SPR) sensor was carried out [134]. It was shown that phosphorene increases the sensitivity of the silver sensor for detecting DNA. However, the fast degradation of BP exposed to the air could limit the sensor's applications. To prevent that, the BP layer can be protected by graphene or TMDCs. A simulation showed that it not only protects BP against oxidation but also further increases the sensitivity [134]. Adding DNA molecules causes a change in the refractive index of the detection medium, which affects the sensor transmission shift. Fig. 2.17a and Fig. 2.17b show schematics of both sensor configurations – ITFG and SPR – respectively.

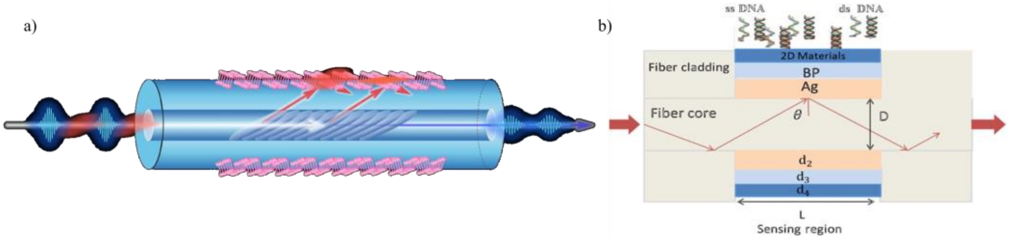

Fig. 2.17 a) Schematic of an integrated tilted fibre grating configuration based on BP. Reprinted from [10], with permission from Elsevier. b) Schematic of a fibre optic surface plasmon resonance based on phosphorene. Reprinted from [134], with permission from Elsevier.

The conductance of BP changes as a result of absorption of gas or humidity molecules [53], [135]. Marmolejo-Tejada et al. demonstrated a NO sensor based on a phosphorene field effect transistor with a LoD at 19 nM/L [135]. Moreover, a BP FET with an Al_2O_3 protective layer was used as a humidity sensor [53]. As the level of water molecules increases, the conductance of the FET device increases, due to the electrostatic gating effect. Furthermore, BP can be used as a NO_2 molecule sensor [136]. However, forming a BP-ZnO composition improved the response speed and sensitivity of the sensor [137].

Detecting metal ions is especially important because they can be found everywhere. Zinc and magnesium are very important in many biological processes in our bodies. Zinc influences cell and connective tissues growth, DNA synthesis, immune system function or bone mineralisation [138]. Magnesium plays an important role in bone mineralisation or muscular relaxation [139]. However, both a lack or excess of either has a negative effect on human health, so it is important that, with the development of industry, we have to deal with higher environmental pollution with heavy metals [140].

Many techniques have been studied to detect metal ions. One such technique involves the use of fluorescence phenomena. Li et al. [141] used Au nanoclusters (Au NC) as a zinc ion sensor. Adding Zn^{2+} ions to a mixture of methylimidazole and Au NC formed a Zn metal-organic framework (Zn-MOF). As a result, Au NC partially aggregate, which enhances the fluorescence. Phosphorene was also found sensitive to metal ions. A radiometric fluorescence sensor based on BP quantum dots was presented to detect mercury ions [82]. It works on the inner filter effects (IFE) between BP and tetraphenylporphyrin tetrasulfonic acid (TPPS). With an increasing concentration of Hg^{2+}, the red fluorescence peak of TPPS decreases, while the blue fluorescence peak of BP QDs increases, as shown in Fig. 2.18. However, very low concentrations of Hg^{2+} (~3 nM) were only detected in river water [82]. Smaller concentrations cannot be detected in pure drinking water or tap water.

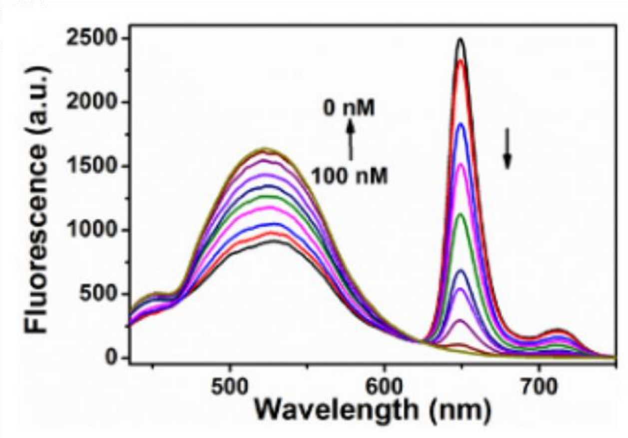

Fig. 2.18 Fluorescence of black phosphorus quantum dots for different concentrations of mercury ions. Reprinted from [82]. Copyright 2017 American Chemical Society.

Another method used for detecting metal ions is electrochemistry. Electrochemically reduced graphene oxide (ERGO) has been used on modified glassy carbon electrode (GCE) [142]. The sensitivity of that prepared electrode was checked using differential pulse voltammetry. Modified GCE has shown three times higher sensitivity for Zn^{2+} ions than GCE without modification and has reached a 0.1 μmol/L limit of detection.

Moreover, multi-walled carbon nanotubes with polydimethylsiloxane were used to determine different concentrations of calcium and magnesium [143]. The change in concentration affected the sensor's resistance. Even 1 ppm of calcium and magnesium are detectable by the sensor. However, electronic device noise and external light may impact the sensitivity of the sensor [143].

In this chapter, the optical and electrical properties of FLBP are described. FLBP is characterised by good carrier mobility and a good on/off ratio, which distinguishes it from other 2D materials. Furthermore, its bandgap can be tuned in a wide range. The crystal structure of FLBP is anisotropic, which affects its interaction with light – FLBP is strongly birefringent and dichroic. Due to all the mentioned properties, FLBP can be found useful in many applications. Because of its reactivity to humidity, DNA, NO_2 and metal ions, FLBP can be used, for example, in sensors. This property renders FLBP highly appealing to researchers; however, knowledge gaps regarding this material still persist. Notably, comprehensive studies are lacking on how to determine optical constants for continuous layers or how degradation impacts the optical properties of FLBP.

Chapter 3. Motivation and aim of the thesis

The aim of this thesis is to develop methods and tools dedicated to the study of optical parameters of FLBP, which are useful for sensing applications. FLBP layers and suspensions were studied using the polarisation microscopic, spectroscopic, and ellipsometric methods, supported by the electrochemical technique. The use of these methods is also aimed at learning the causes and assessing the degree of degradation of FLBP and determining its sensory properties. The use of FLBP structures has allowed the development of a new class of optical sensors for the detection of toxic compounds (e.g., heavy metals).

In view of the stated goal, the first research problem was to determine the refractive index and the extinction coefficient of FLBP. Investigation of these optical constants is the first step in studying the optical properties of a material because they are essential for optical and optoelectronic applications. However, there are few studies on the measurement of these properties for FLBP and they mainly focus on the measurement of a single flake rather than a continuous layer. Spectroscopic ellipsometry (SE) is one of the most powerful tools for studying the thickness and optical parameters of thin films. The measurement is based on the change in the polarisation state of light reflected from the surface of the layer of sample. Hence, the measurement itself is non-invasive to the sample. Moreover, ellipsometry is sensitive to changes for very thin films. FLBP is a very promising optical material due to its structure. Its optical parameters change depending on the thickness and degree of degradation of the layer. With ellipsometric measurements, it is possible to quickly evaluate optical parameters, such as the refractive index and extinction coefficient.

The ability to study polarisation phenomena in the material is also important. Polarised light microscopy is the simplest technique to observe optically anisotropic materials, that is, materials whose refractive index or absorption depend on the propagation direction or polarisation of light. The advantages of this technique are that it is easy to use and non-invasive. In addition, information about the quality of the tested layer can be obtained very quickly. For example, diamond is optically isotropic, but stresses in the layer and imperfections such as dislocations are visible when observed under a polarised light microscope. FLBP is optically anisotropic. It also degrades quickly under ambient conditions. Currently, there is a lack of work showing the effect of oxidation and degradation of FLBP on its polarisation parameters. Polarised light microscopy can be used to study the anisotropy in FLBP and how it changes in time in the presence of air.

2D materials are characterised by reactivity to various substances, such as NO, H_2 and humidity. Their optical and electrical parameters also change when they are exposed to metal ions. Currently, many methods of metal ion detection are known, but new ones are still being investigated. Among the various techniques used in sensors, PL and electrochemistry (EC) can be mentioned. PL is light emission from a material as a result of photon absorption. This technique is widely used in sensors for detecting various substances because it is simple to build and use, and the PL response can be obtained in minutes.

EC sensors have high sensitivity, fast operation and are easy to use, which makes them a preferred technique for the detection of various substances.

Thus, the motivation of this thesis was the development of measurement techniques that provide non-destructive testing of FLBP structures under controlled environmental conditions (atmosphere, humidity) and determination of optical parameters that make it possible to correlate their values with the ageing, oxidation and decomposition of the FLBP, along with an evaluation of the kinetics of these processes. Using these tools, the goal was to develop and optimise sensor designs that enable the detection of various compounds that affect humans and the environment.

New materials are constantly being sought for applications in optical and optoelectronic devices. Development and miniaturisation have forced a switch to 2D materials. FLBP has interesting optical parameters, and due to its structure, it is also strongly anisotropic. This allows FLBP to replace bulk materials in polarisation applications. In addition, depending on the preparation method or thickness, BP responds to radiation over a wide range – from visible light to the deep infrared. The wide spectral range increases the number of applications where FLBP can be used.

FLBP degrades very rapidly when exposed to light, water and oxygen. The oxidation process affects the surface condition of the sample, and the thinner the layer, the faster this process occurs. Consequently, the oxidation process influences the properties of BP. The electrical parameters decline rapidly, while the optical ones demonstrate greater stability against FLBP layer degradation. Hence, observing the layer under polarised light microscopy should make it possible to determine whether the BP has degraded, based on its optical anisotropy.

Furthermore, methods are being sought to protect FLBP from degradation. One approach is to use a protective layer, such as P_xO_y or AlO_x. Another option is to form a composite with another material, such as ZnO. It has been noted that this not only protects FLBP from oxidation, but can also increase its sensory properties. Another method of protecting FLBP is to form a P alloy with As. b-AsP has high stability in air and, like FLBP, a broad response to optical radiation.

One application where FLBP can be used is sensors. Detection of various chemical substances is very important for human health and the condition of the environment. These substances react with certain materials, either attaching to the surface, absorbing, or modifying them. This causes changes in their optical or electrical properties. For example, adsorption can affect the local surface potential, among other things. It has been shown that FLBP is sensitive to various gases (e.g. NO, NO_2, H_2), humidity, and biological substances. In addition, it has been noted that it can be sensitive to the presence of metal ions. Metal ions can be either essential or harmful to humans and the environment. Heavy metal ions such as Hg^{2+}, Pb^{2+}, Cd^{2+} and AsO^{2-} are hazardous to health, while Mg^{2+} and Zn^{2+} ions play important roles in many processes needed for the functioning of human (and animal) organisms. This is why the ability to detect metal ions is so important. Metal ions adsorb on the surface of FLBP, which affects the bandgap and other electronic and optical properties of BP. This indicates that it should be possible to build a BP-based sensor to detect various metal ions. However, the construction of a BP-based PL sensor is problematic, due to the fact that FLBP's PL response is in the deep infrared. Combining BP or b-AsP with ZnO shifts the optical response to the visible range, which is definitely cheaper than working in the infrared range. In addition, ZnO protects the FLBP from oxidation.

Based on the defined aim of the work, the following research hypotheses were proposed:

Hypothesis I: The selection of parameters involved in the deagglomeration and centrifugation processes of BP flakes allows for a significant reduction in both their size and thickness distribution. This reduction facilitates the achievement of optical properties in coatings that closely resemble those found in 2-dimensional phosphorene materials with homogeneity at a millimetre scale.

Hypothesis II: Mapping the optical polarisation parameters at the surface level will enable the assessment of the oxidation and degradation kinetics of FLBP nanostructures.

Hypothesis III: The combination of FLBP and ZnO significantly improves both the efficiency and long-term stability of ZnO-based sensors.

In Chapter 1, an introduction to 2D materials and their exfoliation methods are presented. At the beginning, the electrical and optical parameters of graphene and TMDCs are discussed.

Then, BP’s background is provided, and it is compared to the previously mentioned 2D materials. Applications of 2D materials are also presented in this chapter.

Chapter 2 includes a detailed theoretical introduction to FLBP. First, the electrical and optical properties are discussed. Then, the FLBP degradation process is described. Due to its structure, FLBP is characterised by optical anisotropy, which is also discussed in this chapter. At the end, examples of sensors based on FLBP are presented.

In Chapter 3, the aim, motivation and hypothesis of this dissertation are discussed.

In the study, Chapter 4 introduces various methods used for FLBP preparation. The author participated in the preparation of liquid and electrochemically exfoliated FLBP and was responsible for preparing composite FLBP and b-AsP with ZnO. Chapter 4 also presents the impacts of the exfoliation process on the prepared material. The study also discusses the results of mixing FLBP with zinc oxide (ZnO) nanoparticles and nanorods. Then, the next section describes the determination of the refractive index and extinction coefficient. Spectroscopic ellipsometry (SE) was utilised as a fast and effective technique for measuring the optical properties. The SE measurements were acquired by the author and analysed in collaboration with Professor Łukasz Skowroński from the University of Science and Technology in Bydgoszcz. The following section focuses on measurements using polarised-light microscopy. All the results presented in Section 4.3 were obtained by the author. Firstly, the diamond layer as a reference was measured to optimise the polarisation measurements. Then, changes in the intensity of light reflected on the BP layer over time are presented and discussed. Lastly, the sensors based on FLBP and ZnO are presented. The author conducted all measurements while collaborating with Dr. Roman Viter from the University of Latvia for the sensor designs. The photoluminescence (PL) and electrochemical (EC) methods are used to assess the sensitivity of the prepared materials to varying metal ion concentrations.

Chapter 5 contains a summary of all the studies presented in this dissertation. Conclusions from the experimental section are also presented. Further possible directions for research are also indicated, expanding on those in the dissertation.

Chapter 4. Experiments and results

This chapter encompasses the description of sample preparation, the characterization methods employed to analyze the studied structures, an account of the experimental procedure, the obtained results, and a subsequent discussion.

4.1 Preparation and characterization of few-layer black phosphorus

The properties and application of FLBP differ depending on the exfoliation method [11], [12]. Hence, during my research, electrochemical, liquid, and mechanically exfoliated FLBP were used. Preparation of the black phosphorus-zinc oxide material was the author's responsibility, while the electrochemically and liquid exfoliated BP were prepared in collaboration with Dr. Paweł Jakóbczyk from the Department of Metrology and Optoelectronics. Black arsenic phosphorus was prepared in collaboration with Dr. Łukasz Macewicz. All microscopic and spectroscopic results, except for SEM measurements, were obtained by the author.

4.1.1 Electrochemical exfoliation of few-layer black phosphorus

Electrochemical exfoliation is widely used to fabricate 2D materials [144]. In addition to reducing the thickness of FLBP, the electrochemical exfoliation technique also reduces the oxidation level of the BP [145]. FLBP was prepared by the procedure described in [146] and below. Bulk BP was obtained from Smart Elements (Austria). Dimethyl sulfoxide (DMSO) and tetrabutylammonium tetrafluoroborate (TBABF4) were purchased from Sigma Aldrich (Poland). The BP was used as a cathode, which was immersed with a platinum wire in a 0.01 M solution of TBABF4 in DMSO. A preliminary DC voltage of 2 V was applied for 30 minutes and then increased to 4 V for 12 hours. After that, the obtained solution was sonicated. The exfoliated BP was centrifuged at different speeds and deposited on laboratory glass and Si substrates to obtain BP fractions of different sizes.

Three sets of FLBP with different centrifugation speeds were prepared. Designations of the samples and their characterization methods are shown in Table 4.1.

The first set of FLBP on glass substrates was examined using a Metash UV-9000 spectrophotometer to obtain the dependence between the transmission and centrifugation speeds.

Table 4.1. Designations of all sets of electrochemical exfoliated FLBP samples.

	0k rpm	3k rpm	6k rpm	9k rpm	Characterisation methods
1 set	FLBP-0k-1	FLBP-3k-1	-	FLBP-9k-1	spectrometry
2 set	FLBP-0k-2	FLBP-3k-2	FLBP-6k-2	FLBP-9k-2	polarised light microscopy, SEM
3 set	FLBP-0k-3	FLBP-3k-3	FLBP-6k-3	FLBP-9k-3	Polarised light microscopy,

The transmittances were measured in the range of 300–1000 nm and are shown in Fig. 4.1. FLBP-0k-1 has the smallest transmittance, which rises from 60% at 300 nm to 75% at 1000 nm, while the transmittance for the remaining samples decreases, reaching a peak at ~330 nm, and then increases to 95% and 93% at 1000 nm for FLBP-9k-1 and FLBP-3k-1, respectively.

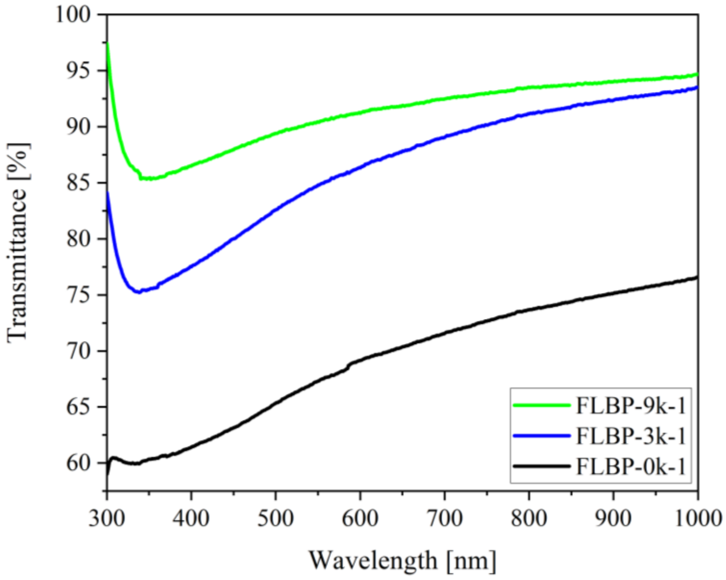

Fig. 4.1 Transmittance curves of FLBP centrifugated at 9000 rpm, 3000 rpm, and 0 rpm.

FLBP-9k-1 is characterised by the highest transmittance across the spectrum. During the centrifugation process, the larger flakes are separated from the smaller ones, resulting in less light being absorbed. This is consistent with previous works showing that the transmittance increases with the decreasing FLBP thickness [147].

Next, two sets of FLBP were prepared at 0 rpm, 3000 pm, 6000 rpm and 9000 rpm centrifugation speeds (Table 4.1) and deposited on a Si substrate. Their microscope (standard view) and polarised images with crossed polarisers (polarisation view) were registered by a LAB 40 POL polarisation microscope from OPTA-TECH. Information about the FLBP's morphology was obtained by a Phenom XL scanning electron microscope (SEM) from Thermo Fisher Scientific. The SEM was working with the operating voltage set at 15 kV.

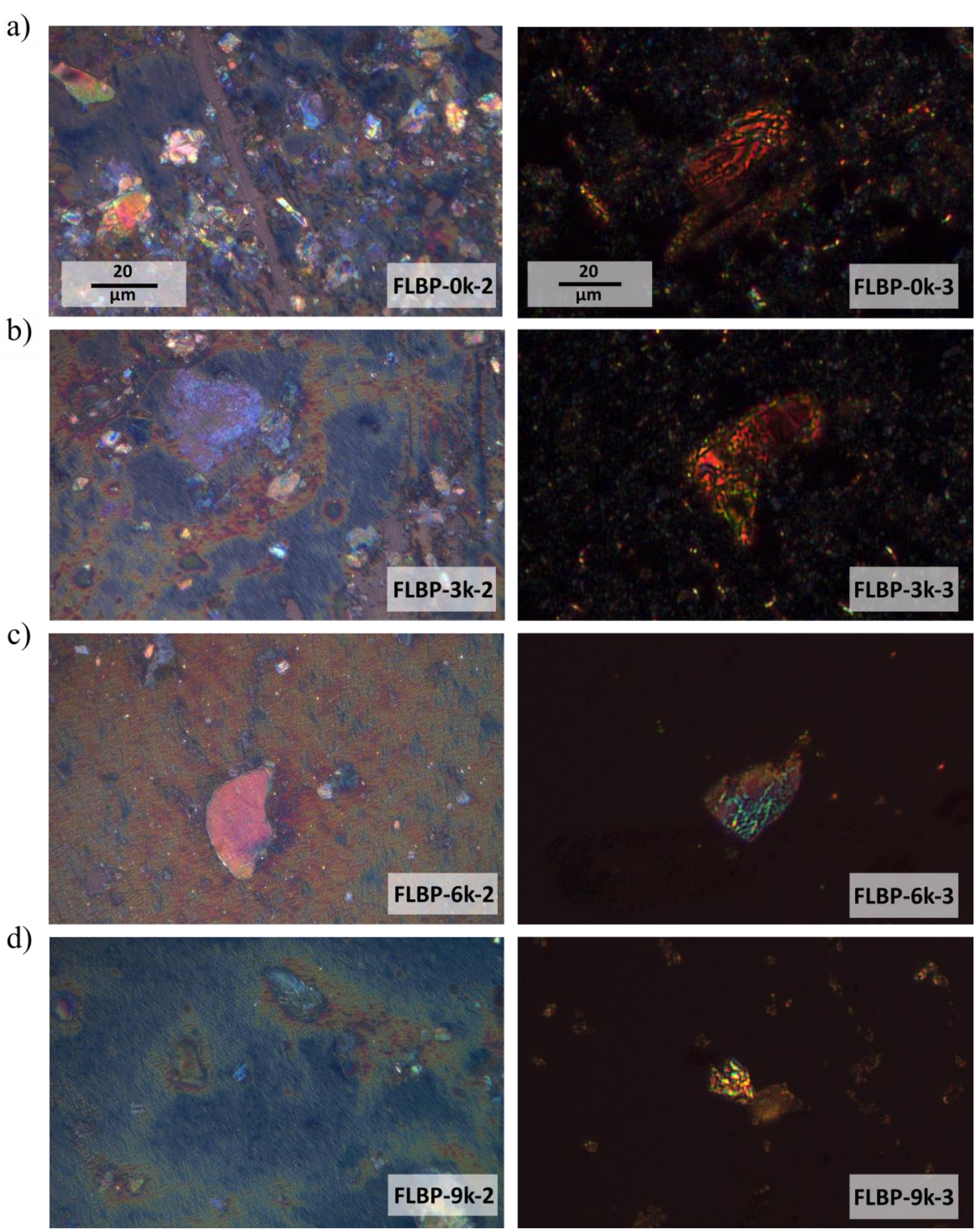

Fig. 4.2 Polarisation images of FLBP centrifuged at a) 0 rpm, b) 3000 rpm, c) 6000 rpm, and d) 9000 rpm for the second and third sets of samples.

The polarisation images of the FLBP are shown in the Fig. 4.2. It can be observed that BP layers consist of many, randomly disoriented flakes, which is indicated by the different intensities and colours on the images [148]. However, these changes could also be attributed to defects such as thickness inhomogeneities, fractures, folding, etc.

The FLBP centrifugated at 0 rpm and 3000 rpm consists of flakes that vary greatly in size (Fig. 4.2a–b), therefore their average layer thickness will be greater than for FLBPs spun at higher speeds, because the largest BP flakes are removed in the centrifugation process [149]. The FLBP spun at 9000 rpm (FLBP-9k-x) did not completely cover the Si substrate because of the lower concentration of flakes and their smaller dimensions (Fig. 4.2d). The same effect is observed for the FLBP sample centrifugated at 6000 rpm from the third set (FLBP-6k-3) (Fig. 4.2c).

The optical anisotropy of FLBP with different centrifugation speeds was also checked. The polarisation images with different rotational angles (angle between sample and crossed polarisers) were collected (Fig. 4.3). For all centrifugation speeds, the intensity of the samples' reflectance change with the rotation angle, which indicates that BP is characterised by birefringence, which is in agreement with previous works [129], [130]. The BP flake is dark when the polarisation of the incident light is oriented along the FLBP crystal axis. Phase retardation increases after rotating the sample and so the intensity of the light reflected from the BP sample also increases [130]. The concentration of BP flakes decreases with the increase in centrifugation speed. FLBP-6k-3 and FLBP-9k-3 have individual flakes scattered over the Si substrate (Fig. 4.3c,d).

SEM images of FLBP-0k-2, FLBP-3k-2, FLBP-6k-2 and FLBP-9k-2 are presented in Fig. 4.4. The FLBP samples are made of many superimposed flakes. With the increasing centrifugation speed, smaller particles and a lower volume are visible. This is consistent with the data described for previous sets of samples and polarisation microscopy results. The ImageJ software was used to determine the average dimensions of the BP flakes from the SEM images. The values obtained are: 4.8±5.6, 2.1±2.0, 1.3±0.52 and 0.72±0.75 μm for FLBP-0k-2, FLBP-3k-2, FLBP-6k-2 and FLBP-9k-2, respectively.

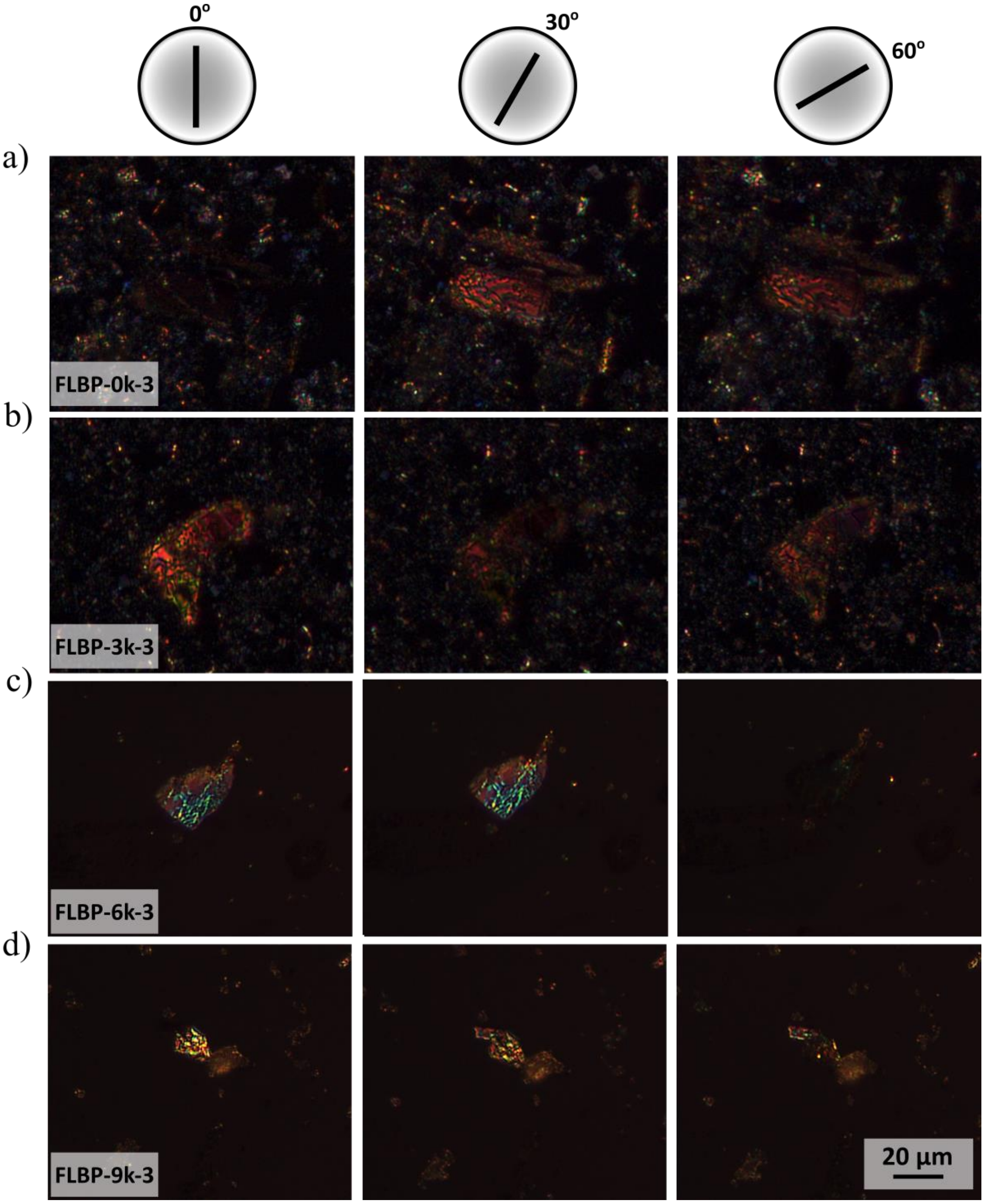

Fig. 4.3 Polarisation images of FLBP centrifuged at a) 0 rpm, b) 3000 rpm, c) 6000 rpm, and d) 9000 rpm with a 0°, 30° and 60° rotational angle.

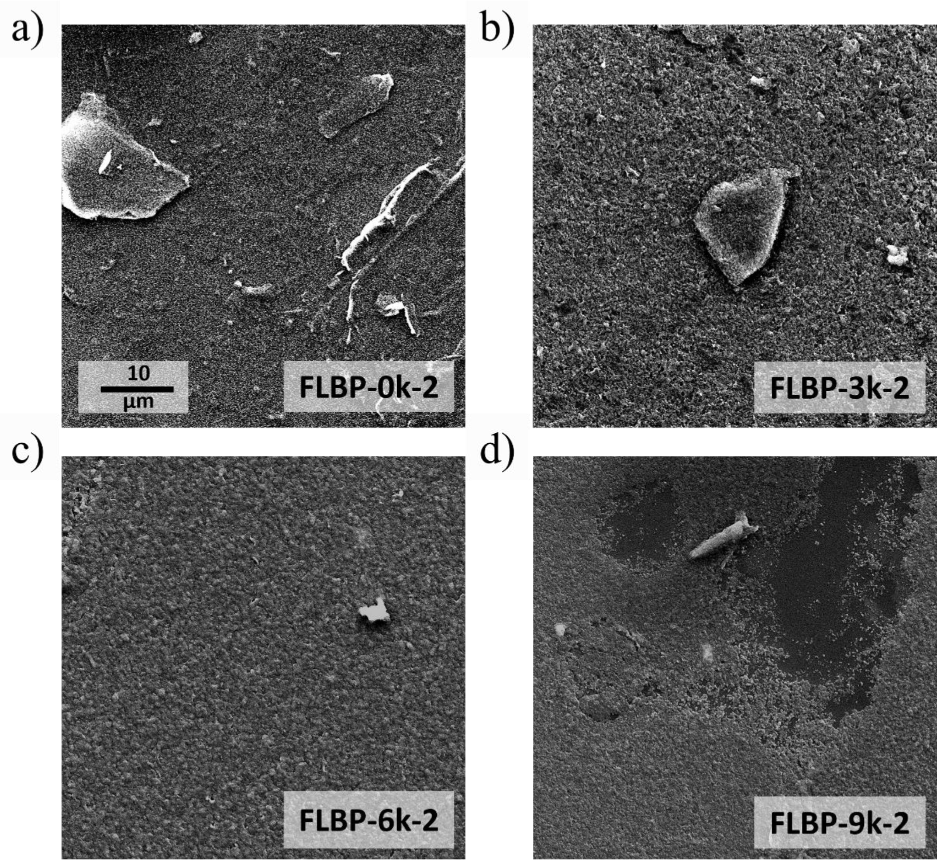

Fig. 4.4 SEM images of FLBP centrifuged at a) 0 rpm, b) 3000 rpm, c) 6000 rpm, and d) 9000 rpm.

Samples vary from one set to the next despite the use of exactly the same parameters during exfoliation. This is because even if a bulk BP of comparable size is utilized, its shape and orientation vary every time, which affects the charge flow through it.

4.1.2 Liquid exfoliation of few-layer black phosphorus

Liquid exfoliation is another very well-known method of obtaining 2D materials [150], [151] that was used in the research described in this dissertation. It uses ultrasonication to insert the energy needed to fragment and eventually exfoliate the layered crystal. The choice of sonication parameters and proper solvent is critical to obtaining a sample without defects [150].

FLBP was prepared using two solvents: DMF and ethanol. 30 mg of preground BP (Smart Elements) was dispersed in 7 ml of anhydrous DMF. The BP dispersion was sonicated for 2 hours using a horn probe ultrasonicator (Bandelin Sonopuls HD2200, 20 kHz). The sonication was carried out under an argon stream with the temperature maintained in the range of 0 to 3 °C using an ice-cooled bath and the power of the tip set at 40 W with a 0.5/0.5 s ON/OFF time. In a set of samples prepared in ethanol, 30 mg of bulk BP was dispersed in 8 mL of deoxygenated 95% ethanol (Sigma Aldrich). The sonication was performed under the same conditions and settings, but it lasted 4 hours. The suspension in DMF was named FLBP-0k$_{DMF}$. The suspensions in ethanol were centrifuged at 3,000, 6,000, 9,000 and 11,000 rpm for 5 minutes to remove the residual unexfoliated BP. The designations of the liquid-exfoliated FLBP in ethanol are presented in Table 4.2.

Table 4.2. Designations of liquid-exfoliated FLBP in ethanol.

Centrifugation speed	3k rpm	6k rpm	9k rpm
Ethanol	FLBP-3k$_{ETH}$	FLBP-6k$_{ETH}$	FLBP-9k$_{ETH}$

The absorbance of the FLBP in ethanol was recorded using Ocean Optics usb2000 spectrometer in the wavelength range of 350 to 1,100 nm (Fig. 4.5). With the increasing centrifugation speed, the absorbance of FLBP decreases. This is as expected as the sizes and concentrations of the BP flakes decrease with the higher spin speed. FLBP-11k is almost completely transparent, indicating that mainly smaller BP flakes remain in the solution after the centrifugation process. The exfoliated FLBP centrifugated at 3000 rpm is characterised by the highest absorbance, which is constant up to 500 nm and then begins to decrease steadily.

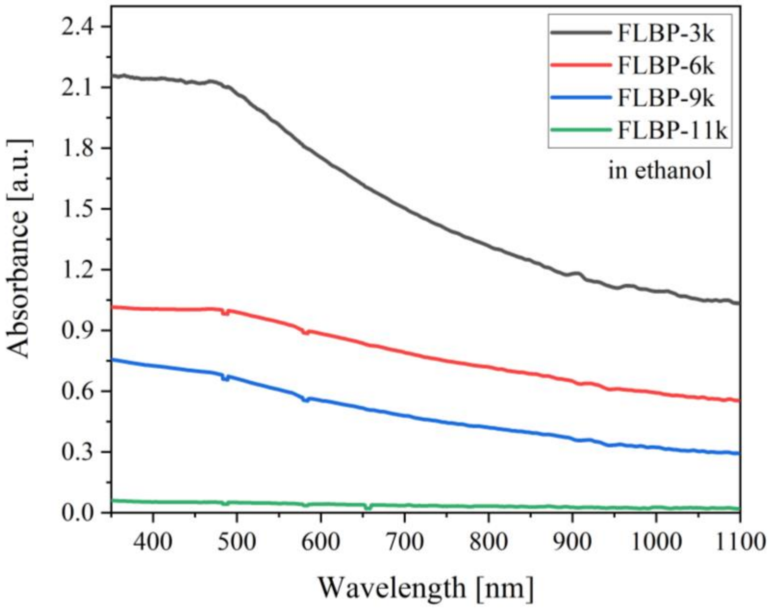

Fig. 4.5 Absorbance of few-layer black phosphorus with different centrifugation speeds.

4.1.3 Mechanical exfoliation of few-layer black phosphorus

Mechanical exfoliation was used to first produce the 2D material. Despite its ineffectiveness in producing larger layers and difficult-to-control results, this method remains the easiest, fastest and most cost-effective exfoliation technique.

Adhesive 3M tape was used to mechanically exfoliate FLBP on a Si substrate directly from bulk BP. The result was single flakes scattered on the Si surface – $\mathrm{FLBP_{MECH}}$. Fig. 4.6 shows a microscopic photo of FLBP on Si after exfoliation.

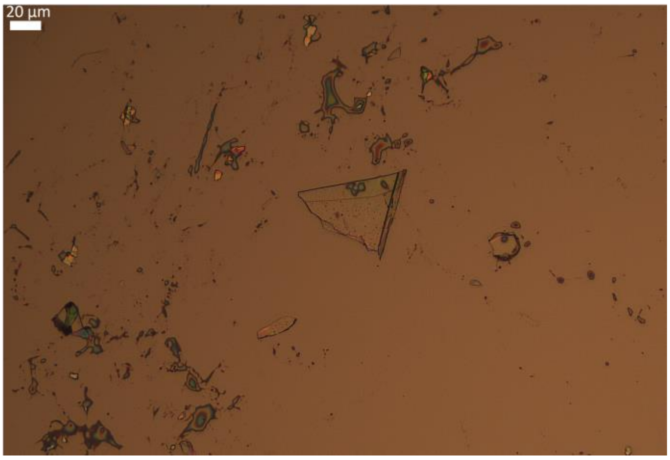

Fig. 4.6 Microscopic image of mechanically exfoliated FLBP on Si substrate.

Since BP degrades when exposed to air [113], even microscopic images show changes due to oxidation. In Fig. 4.7, the images taken immediately after exfoliation and after 30 days are shown. Blisters and other lesions can be seen on the surface of the BP flakes. Similar changes have been observed before, as a result of the oxidation process [57].

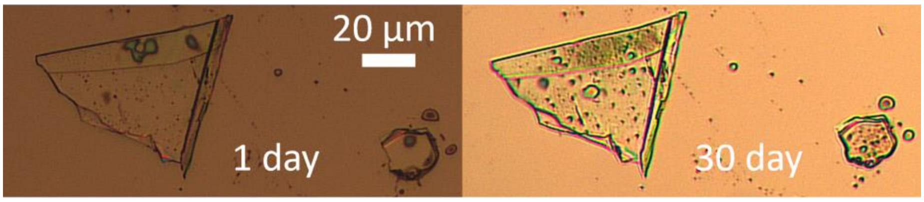

Fig. 4.7 Microscopic image of mechanically exfoliated FLBP on Si substrate immediately after exfoliation and after 30 days.

4.1.4 Black arsenic-phosphorus preparation

The alloying BP with arsenic improves the stability and also affects the parameters. Thanks to this, the range of BP applications is expanding [63], [152]. In my research, b-AsP was used to compare its sensitive properties to FLBP. B-AsP was prepared in cooperation with Łukasz Macewicz from the Faculty of Electronics, Telecommunications and Informatics, Gdańsk University of Technology, using chemical vapour deposition. Red phosphorus (RP), tin (Sn), SnI_4 and arsenic (As) were used as precursors. The reagents and silica substrate were placed under vacuum in a quartz ampule and heated first to a temperature of 610°C, then to 560°C. The substrates were kept at a temperature of 50°C lower than the reagents. Next, the ampule was slowly cooled to room temperature. As a result of the CVD, a column of b-AsP was formed on the silicon, which was sonicated for 10 minutes and then centrifuged at 2000 rpm for 5 minutes to obtain b-AsP nanoribbons. A detailed description of the preparation method can be found in [153]. Amounts of red phosphorus and arsenic were used in different proportions to obtain four compositions of b-AsP: b-$As_{0.1}P_{0.9}$, b-$As_{0.2}P_{0.8}$, b-$As_{0.5}P_{0.95}$ and b-$As_{0.8}P_{0.2}$. Table 4.3 presents the amounts of reagents used in the CVD process.

Table 4.3. Amount of reagents used in CVD process for obtained compositions of b-AsP.

	RP [mg]	Sn [mg]	SnI_4 [mg]	As [mg]
b-$As_{0.1}P_{0.9}$	300	10	5	80
b-$As_{0.2}P_{0.8}$	250	10	5	150
b-$As_{0.5}P_{0.95}$	103	10	5	250
b-$As_{0.8}P_{0.2}$	36	10	5	350

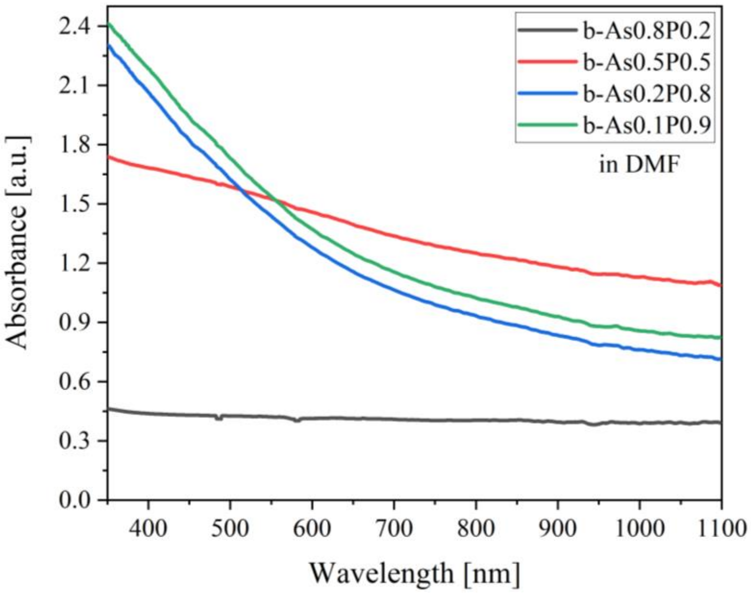

Fig. 4.8 Absorbance of black arsenic-phosphorene with different concentrations of As and BP.

The absorbance of the b-AsP was recorded using Ocean Optics usb2000 spectrometer in the wavelength range of 350–1100 nm (Fig. 4.8). The absorption shape of the b-AsP is affected by both the arsenic and BP. The lowest absorbance is observed for b-$As_{0.8}P_{0.2}$. It is also almost constant over the entire tested range. The absorbance increases with the decreasing amount of As, while the absorbance curve ceases to be constant, but decreases with the increasing wavelength. The absorbance of b-$As_{0.2}P_{0.8}$ and b-$As_{0.1}P_{0.8}$ decrease more rapidly than the absorbance of b-$As_{0.5}P_{0.5}$.

4.1.5 Black phosphorus – zinc oxide preparation

Because of its sensory properties and its potential to increase the stability of FLBP in air, zinc oxide was chosen to be added to pre-prepared FLBP solutions. FLBP-$3k_{ETH}$ and b-$As_{0.1}P_{0.9}$ were selected to be mixed with zinc-oxide nanorods (ZnO NRs) and nanofibres (ZnO NFs) as they represent averaged parameters for liquid-exfoliated FLBP.

The method of mixing BP with ZnO NRs is shown in Fig. 4.9a. 10 mg of ZnO NRs was added to 250 µl of FLBP-$3k_{ETH}$ in ethanol and stirred for 3 days. Next, the solution was centrifuged at 6000 rpm by 3 minutes. The supernatant was removed and 1 ml of ethanol was added to the residual. The same procedure was used to prepare the solution of b-AsP and ZnO NRs, but the ethanol was exchanged for DMF. Furthermore, 10 mg of ZnO NRs was stirred in 1 ml of ethanol. The prepared solutions were deposited on Si substrates and left to dry.

FLBP-$3k_{ETH}$ and b-$As_{0.1}P_{0.9}$ were mixed with ZnO NFs and deposited on conductive ITO glass to produce working electrodes (Fig. 4.9b). First, the glass plates were cleaned in an Ar-O_2 plasma for 15 minutes and 20 µL of 5 mM zinc acetate $Zn(CH_3COO)_2$ in methanol was deposited on them by drop-casting. The glasses were then annealed at 350°C for one hour in an air atmosphere. Meanwhile, FLBP-$3k_{ETH}$ and ZnO NFs were mixed. 250 µl of FLBP-$3k_{ETH}$ was mixed with 750 µl of ethanol (ETOH) and then 10 mg of ZnO NFs was added.

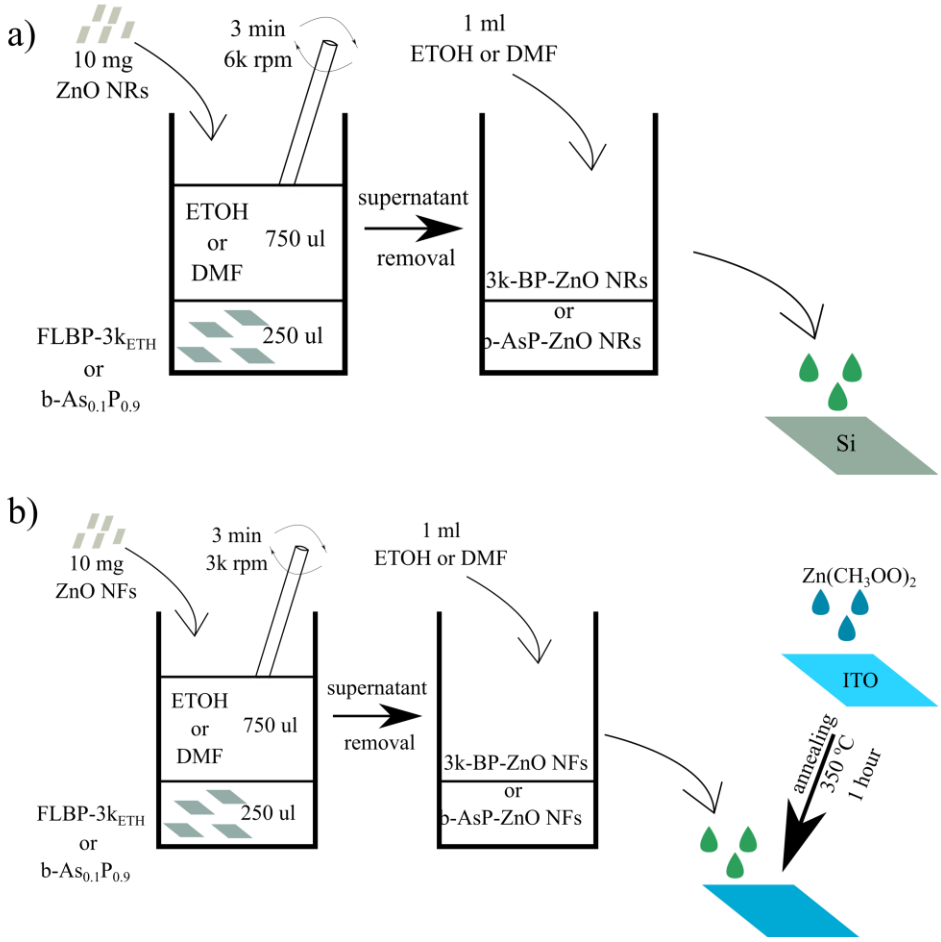

Fig. 4.9 a) 3k-BP-ZnO NRs and b-AsP-ZnO NRs on Si and b) 3k-BP-ZnO NFs and b-AsP-ZnO NFs electrodes preparation.

The prepared solution was stirred overnight and then centrifuged at 3000 rpm for 3 minutes. The supernatant was removed and 1 ml of ethanol was added to the residue. A similar procedure was used to prepare the b-As$_{0.1}$P$_{0.9}$ and ZnO NFs solution but the ethanol was replaced with DMF. Both solutions were then applied to the prepared glass slides and left to dry. The pure ZnO NFs solution was also prepared and deposited on the ITO glass slides.

The designations of the prepared samples are presented in Table 4.4.

Table 4.4. Sample designations

	FLBP-3k$_{ETH}$	b-As$_{0.1}$P$_{0.9}$
ZnO NRs	3kBP-ZnO NRs	b-AsP-ZnO NRs
ZnO NFs	3kBP-ZnO NFs	b-AsP-ZnO NFs

The PL spectra of ZnO NRs, 3kBP-ZnO NRs and b-AsP-ZnO NRs were collected and compared (Fig. 4.10). The spectrum of ZnO NRs has three peaks at ~382 nm, ~480 nm and

~550 nm. Mixing with BP and b-AsP caused a change in the shape of the spectra and merged the first two peaks into one at ~517 nm. The intensity of this peak is the same for both samples with BP.

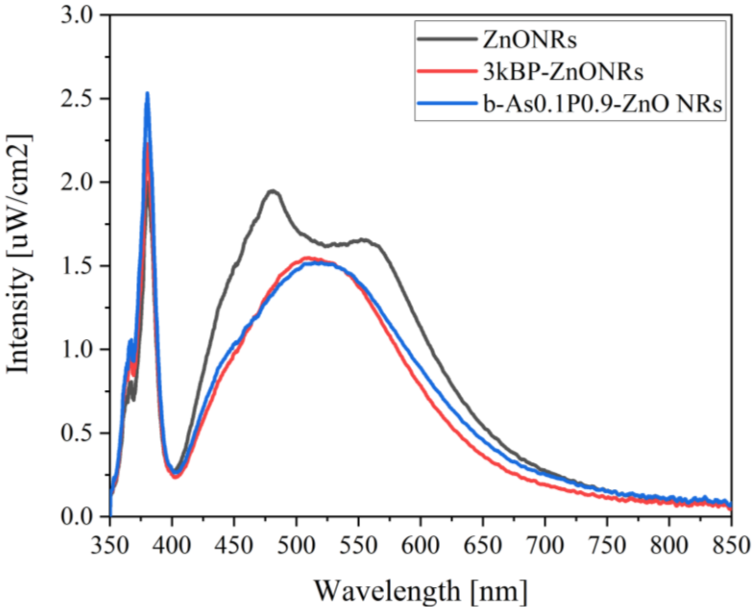

Fig. 4.10 Comparison of PL spectra of ZnONRs, BP-ZnONRs and b-AsP-ZnONRs

The morphology of the 3kBP-ZnO NFs and b-AsP-ZnO NFs were obtained by SEM (FEI Quanta FEG 250) and are shown in Fig. 4.11. The surfaces of both samples are homogeneous, although the b-AsP-ZnO NFs is characterised by higher aggregation with large pores. 3kBP-ZnO NFs has a low level of aggregation. The difference between the electrodes is due to the different structures of BP and b-AsP, but also due to the use of different solvents. At the higher magnification in Fig. 4.11, it can be seen that BP and b-AsP completely covered the ZnO nanofibres.

Depending on the exfoliation method, the resulting samples may differ in parameters and applications. The properties will also be affected by their mixing with other compounds, e.g. As or ZnO. Therefore, in each measurement, the exfoliation method was carefully selected for the needs.

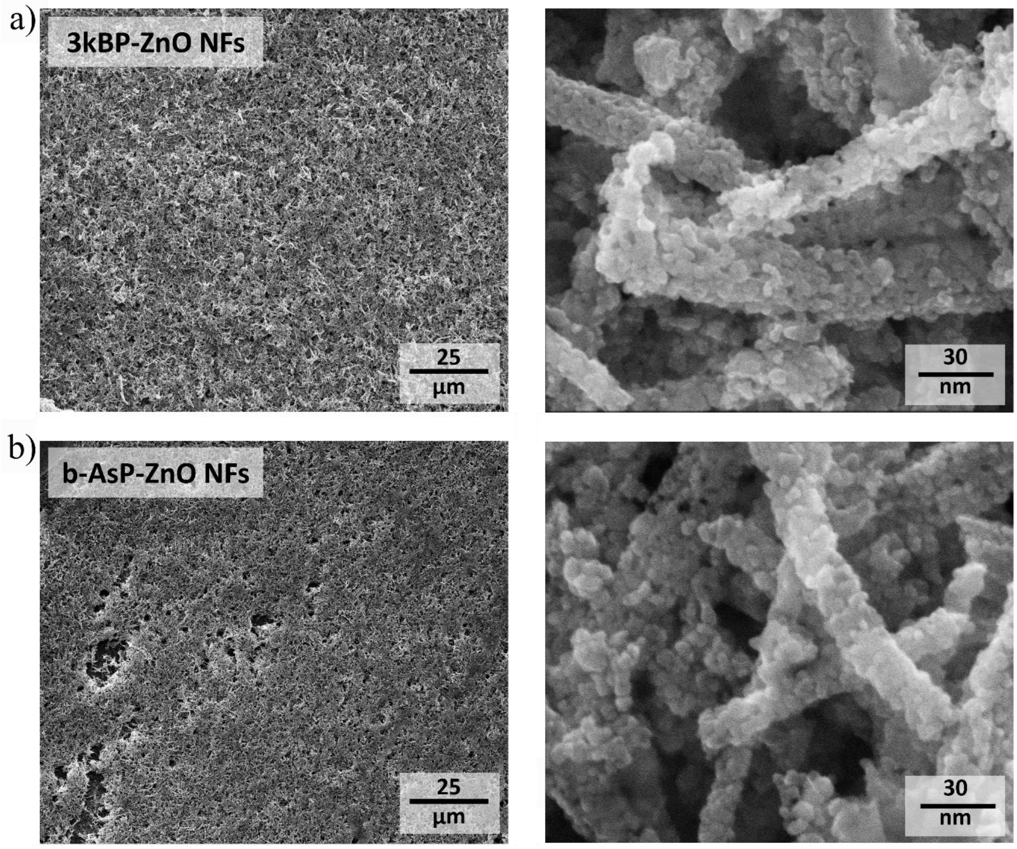

Fig. 4.11 SEM images of a) 3kBP-ZnO NFs and b) b-AsP-ZnO NFs.

4.2 Optical constants of few-layer black phosphorus measured by spectroscopic ellipsometry

The chapter contains characterisation of electrochemically exfoliated FLBP by SE. The SE measurements were obtained by the author, while the analysis was carried out in cooperation with prof. Łukasz Skowroński from Bydgoszcz University of Science and Technology.

In ellipsometry, a polarised light beam illuminates the sample. Then, the reflected light is collected and the change in polarisation state between the in and out beam is measured. In the result, the ratio of the amplitude (called Psi (Ψ)) and the phase shift (called Delta (Δ)) are obtained. The Ψ and Δ parameters are measured for various wavelengths of light. Then, using calculation, the thickness and optical parameters of the sample are studied. The SE was found useful in determining film thicknesses of even to submonolayer coverages [154].

The preparation of the electrochemical exfoliated FLBP is described in section 4.1.1. Ellipsometry measurements were carried out using a Jobin-Yvon UVISEL phase-modulated ellipsometer with the angle of incidence fixed at 70°. All the experiments were carried out at room temperature.

The first set of electrochemically exfoliated FLBP with different centrifugation speeds (FLBP-0k-1, FLBP-3k-1, FLEBP-9k; Table 4.1 section 4.1.1) were used in the SE measurements in the range of 250 nm to 690 nm. Fig. 4.12 presents ellipsometric parameters for the FLBP and Si plates as a reference.

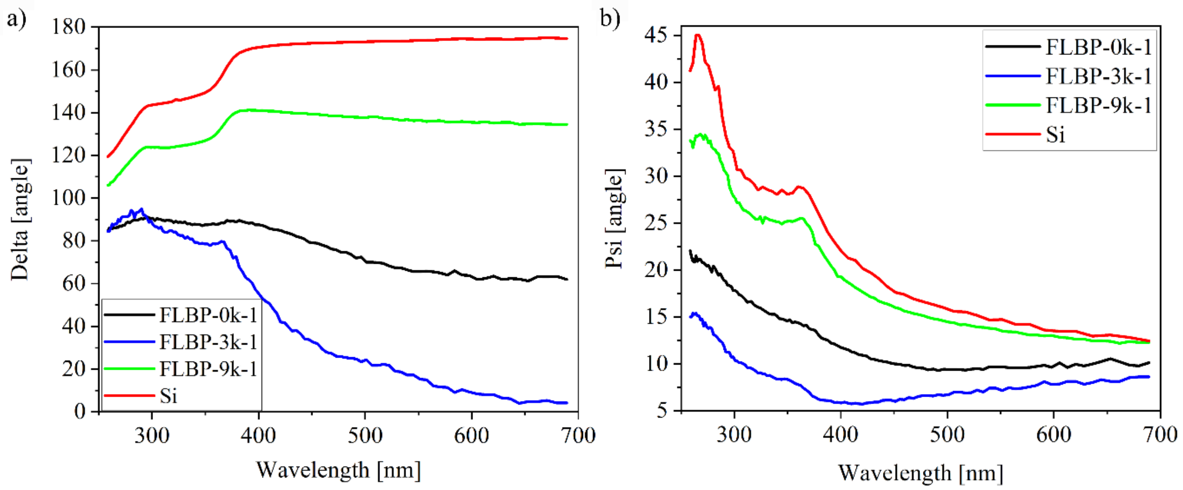

Fig. 4.12 Plot of a) Delta and b) Psi azimuths of Si wafer and FLBP centrifuged centrifugated with 9000 rpm, 3000 rpm, and 0 rpm for the wavelength range of 250 nm to 690 nm.

With the increasing the centrifugation speed, the shapes of the Ψ and Δ characteristics are comparable to the curves for the Si substrate. The Δ and Ψ angles for the FLBP-9k-1 have the same peaks as Si. This is due to the highest transparency of this sample, but it also indicates similar values of optical parameters. Increasing the Ψ angle shows that the absorption decreases with the increasing centrifugation speed (Fig. 4.12b). The Δ angle is sensitive to thickness changes. Therefore, FLBP-9k-1 is the thinnest because only the smallest flakes are left after the centrifugation process. As the centrifuge speed decreases, the Δ angle decreases (Fig. 4.12a). However, the samples' inhomogeneity and surface defects also affect the measurement results.

The second set of the electrochemically exfoliated FLBP centrifugated at 0 rpm, 6000 rpm and 9000 rpm (FLBP-0k-2, FLBP-6k-2 and FLBP-9k-2) were also measured using SE. The wavelength range of 260 nm to 830 nm was selected. The Δ and Ψ parameters are shown in Fig. 4.13. The shape of the characteristics present normal dependence for semiconductors [154]. As a reference, the Si plate was also measured.

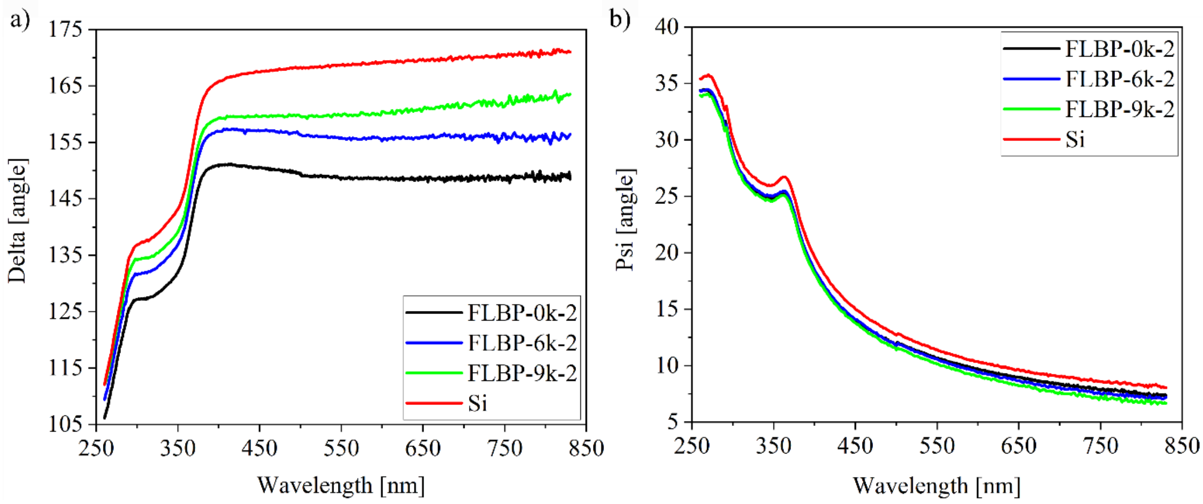

Fig. 4.13 Plot of a) Delta and b) Psi azimuths of Si wafer and FLBP centrifugated at 0 rpm, 6000 rpm and 9000 rpm for wavelength range of 260 nm to 830 nm.

In spectroscopic ellipsometry, a 3 mm wide and 10 mm long spot size is used. It is larger than the size of the BP flakes, hence, it can be assumed that the signal is measured from multiple flakes at once. The Δ angle (Fig. 4.13a) shows a strong dependency on the thickness of the sample. The value for FLBP-9k-2 was closest to the Δ angle of the Si wafer. This is due to the highest transparency and the smallest concentration of BP flakes in the sample. The Ψ angle, in turn, almost does not depend on the centrifugation speed because it depends on the optical constants and absorption of the measured layer. As can be seen in Fig. 4.13b, all curves are nearly identical. Therefore, all samples are characterised by a similar surface quality.

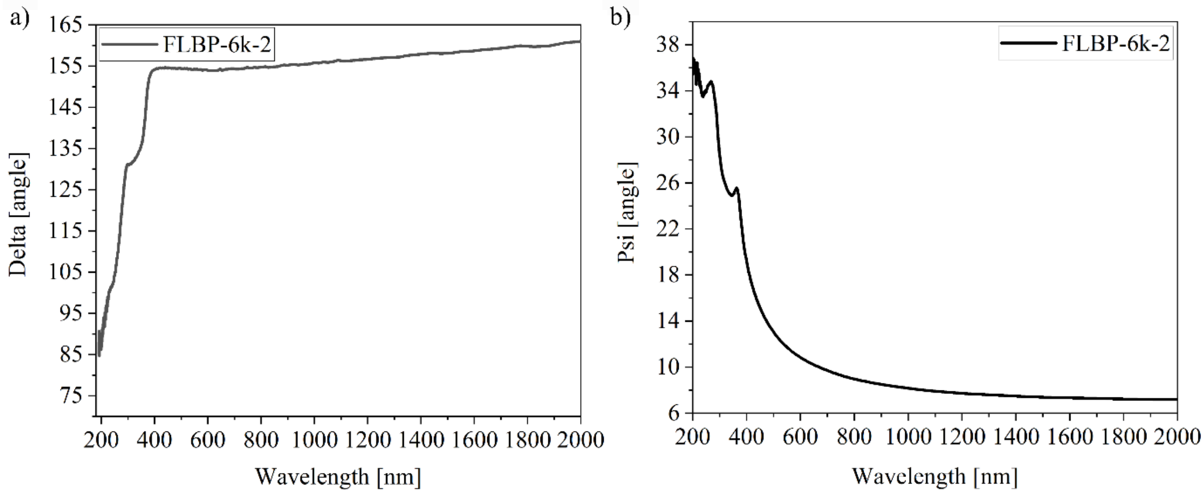

Fig. 4.14 a) Delta and b) psi of FLBP centrifuged at 6000 rpm for wavelength range of 190 nm to 2000 nm.

In the further analyses, the FLBP-6k-2 sample was chosen as it represents the average parameters of the measured FLBP. The ellipsometry measurement was repeated in the wider range of 190–2000 nm. The obtained data are shown in Fig. 4.14. The Δ angle increases rapidly from 200 nm to 500 nm, but above that range, it only slightly rises (Fig. 4.14a). The Ψ angle decreases quickly from 36° at 200 nm to 8° at 1000 nm, then remains almost constant.

To determine the refractive index and extinction coefficient from the ellipsometry data, an analysis is needed. First, a model describing the sample is prepared. In our study, it consists of the silicon substrate, the thin native oxide layer on the substrate – SiO_2 – and a layer representing the BP layer. The BP layer is mixed with air to model the irregularity of the sample surface (Fig. 4.15). The complex refractive index of the Si and SiO_2 layer was taken from the database of optical constants [155]. A Bruggeman Effective Medium Approximation (BEMA) approach was used to model the surface roughness [155], [156]. The optical constants of the FLBP layer were parametrised using a set of oscillators. The standard Mean Squared Error (MSE) was estimated to be 10.

Fig. 4.15 Model used in the analysis of the ellipsometry data.

As a result, the thickness of FLBP was determined to be 38.4 nm. The refractive index and extinction coefficient of the BP layer have also been estimated and are shown in Fig. 4.16.

The extinction coefficient depends on the BP absorption. Hence, as can be observed in Fig. 4.16a, the absorption decreases for wavelengths larger than 400 nm. This tendency was observed in other works, which are described in section 2.1 [100], [101]. Furthermore, the extinction coefficient has three peaks at 226 nm, 290 nm, and 360 nm. There are shifted in comparison to the absorption measurement of the sonication exfoliated FLBP in NMP solution. From 600 nm, the excitation coefficient has levelled off, which is consistent with previous results by Lee et al. [76].

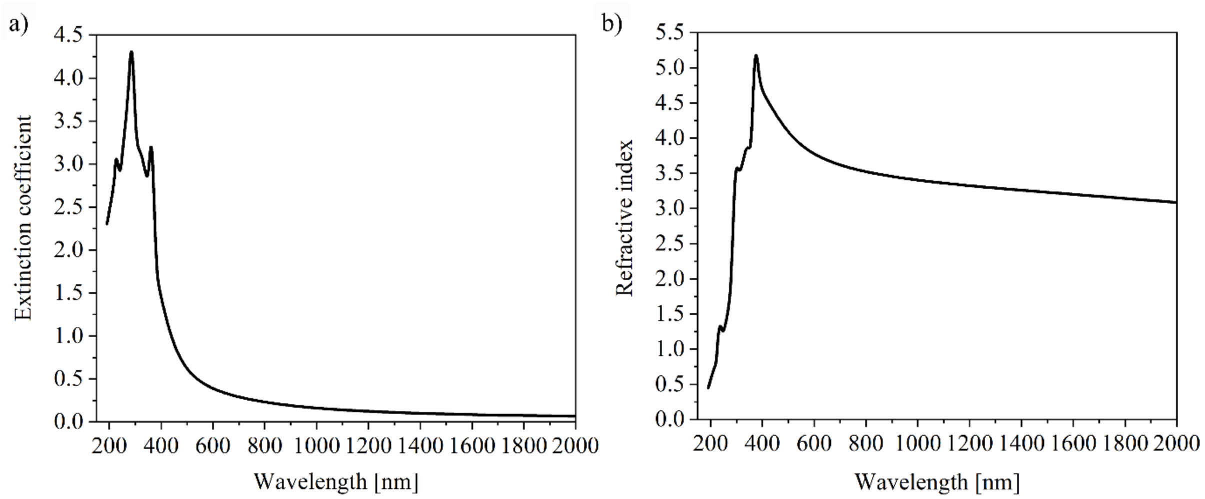

Fig. 4.16 a) Extinction coefficient and b) refractive index of the FLBP-6k sample, obtained from analysis the ellipsometry data.

The refractive index (Fig. 4.16b) increases, reaching peaks at 300 nm, 338 nm, and the largest at 384 nm, then drops sharply to ~4 at 600 nm. Above 600 nm, it starts to stabilise but continues to slightly descend. Lee et al. [76] showed similar results obtained from transmittance and reflectance measurements. The obtained results were further analysed and compared to DFT calculations in [157].

In conclusion, spectroscopic ellipsometry was successfully used to obtain optical constants of electrochemically exfoliated FLBP. It is especially important to know these values if the material is used in optical applications. Separated BP flakes are characterised by optical anisotropy but prepared layers consist of many, randomly oriented flakes whose thickness depends on the centrifugation speed. Hence, it can be assumed that the obtained optical constants represent a quasi-isotropic layer. Furthermore, due to the consistency with previous research on the matter, it can be concluded that the parameters obtained resemble the properties of a 2D phosphorene material (hypothesis I).

4.3 Optimalisation of microscopic measurements of polarisation imaging

In this chapter, polarised light microscopy is used to characterise the polarisation parameter of FLBP. Initially, the well-known surface of diamond was analysed to optimise the polarisation microscopy measurements. Then, in section 4.8.1, the birefringence and dichroism analyses of the FLBP were described. All the presented results were obtained by the author.

Polarisation microscopy is a powerful tool for imaging optically anisotropic materials. It is characterised by fast image acquisition, a submicrometer lateral resolution and a large field of view. The scheme of the measurements by polarised light microscope is presented in Fig. 4.17. To be able to observe the anisotropy of the samples, the microscope is equipped with a polariser positioned upstream of the sample and an analyser upstream of the detector. A LAB 40 POL polarisation microscope from OPTA-TECH was used in our measurements. A sample was placed on the rotational plate and was illuminated by a 50 W halogen lamp or by a green diode pumped laser module (532 nm).

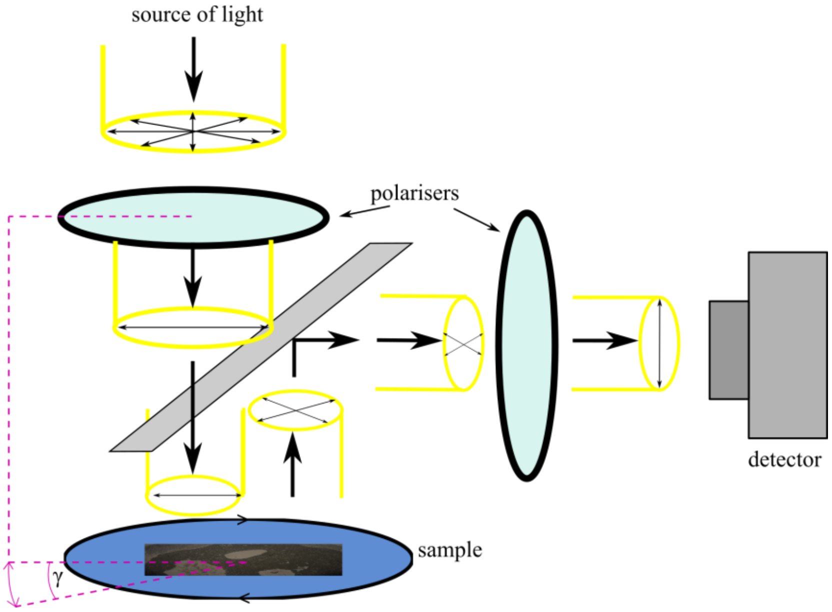

Fig. 4.17 Scheme of a polarised light microscope. The angle γ is a rotational angle between crossed polarisers and sample.

The diamond layer was measured as a reference to check and calibrate the polarised light microscope. Ideal diamond is optically isotropic, however, the occurrence of impurities and dislocations influence its quality. The knowledge about diamond defects is important in optimising the growth conditions. Until now, few techniques were presented to analyse diamond, such as X-ray topography, cathodoluminescence [158], and polarisation microscopy [159]. Polarisation microscopy is widely used to observe the birefringence pattern in diamond, making it possible to identify defects, dislocations, and strain [159], [160].

The quality of two boron (B) and nitrogen (N) co-doped diamonds grown on two types of single crystalline diamond (SCD) were compared. The layer images were registered before and after the annealing process using the polarised light microscope. The measurements were carried out for different angles between the sample and the cross-polarisers. One of the SCD substrates was IIa from New Diamond Technologies with impurity levels of N < 10 ppb and B < 50 ppb. The second one was Ib substrate with impurity levels N < 1 ppb and B < 0.05 ppb. To grow the diamond, a microwave plasma-assisted chemical vapour deposition (MPACVD) system was used (2.45 GHz, Seki Technotron AX5400S, Japan). During the growth process, the N flow was set at 0.02 ppm and three B concentrations were used: 2500 ppm, 5000 ppm, and 7500 ppm. The samples were then annealed in a vacuum at 800°C for 2 h and cleaned using H2SO4:HNO3 (1:1) at 200 °C for 2 h. The process of sample preparation and modification have been described in [161].

The level of impurities in the substrate can affect the quality of the growing layer [162]. The polarisation images of diamond on the SCD IIa substrate are homogeneous (Fig. 4.18). The birefringence pattern is also not visible. Furthermore, increasing the B doping concentration (Fig. 4.18a–c) and the annealing process (Fig. 4.18d–f) do not affect the surface quality of the grown layers. Small areas of discolouration may indicate the presence of defects, such as stacking faults or dislocations. Indeed, hillocks formed by these defects were found in AFM images [161]. However, due to their small size (1–2 μm) relative to the measurement area (~500 μm), these defects do not cause birefringence that would be visible under the microscope used.

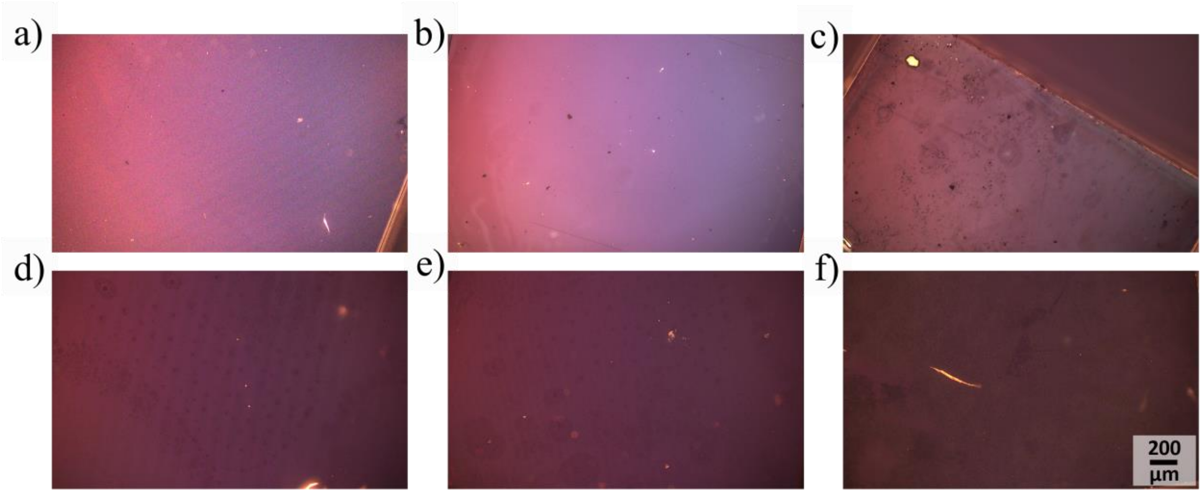

Fig. 4.18 B/N co-doped diamond grown on SCD IIa substrate for different B concentrations before annealing: a) 2,500 ppm, b) 5,000 ppm, and c) 7,500 ppm and for different B concentrations after the annealing: d) 2,500 ppm, e) 5,000 ppm, and f) 7,500 ppm.

The polarisation images of B/N co-doped diamond grown on a SCD Ib substrate with different B concentrations are shown in Fig. 4.19a–c. The cross-shaped birefringence pattern (marked by red lines in Fig. 4.19) is present regardless of the B concentration. The most visible pattern is for the image of the diamond film with a 5,000 ppm B concentration (Fig. 4.19b). Due to impurities on the substrate, during the growth of the diamond layer, tensions are created, which translated into a birefringence pattern [162]. B/N co-doped diamond with the B concentration of 7,500 ppm is characterised by large irregularities (Fig. 4.19c). After annealing, the cross-shaped pattern became even more visible (Fig. 4.19d–f).

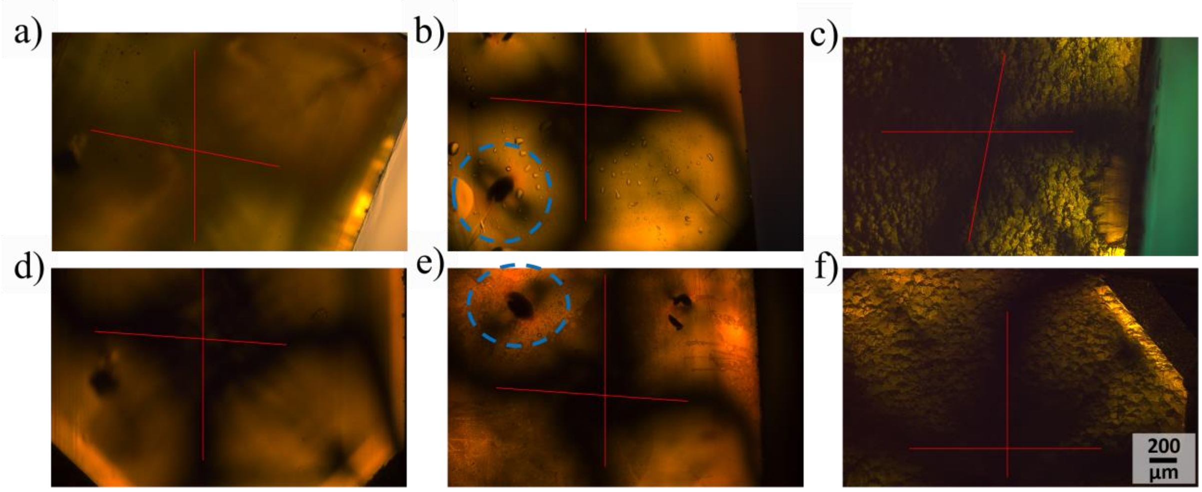

Fig. 4.19 B/N co-doped diamond grown on SCD Ib substrate for different B concentration before annealing: a) 2500 ppm, b) 5000 ppm, and c) 7500 ppm and for different B concentration after the annealing: d) 2500 ppm, e) 5000 ppm, and f) 7500 ppm.

On the surface of the diamond grown on SCD Ib substrate, a petals pattern is also visible (blue marked areas in Fig. 4.19). Their shape changes slightly with the angle of rotation (Fig. 4.20).

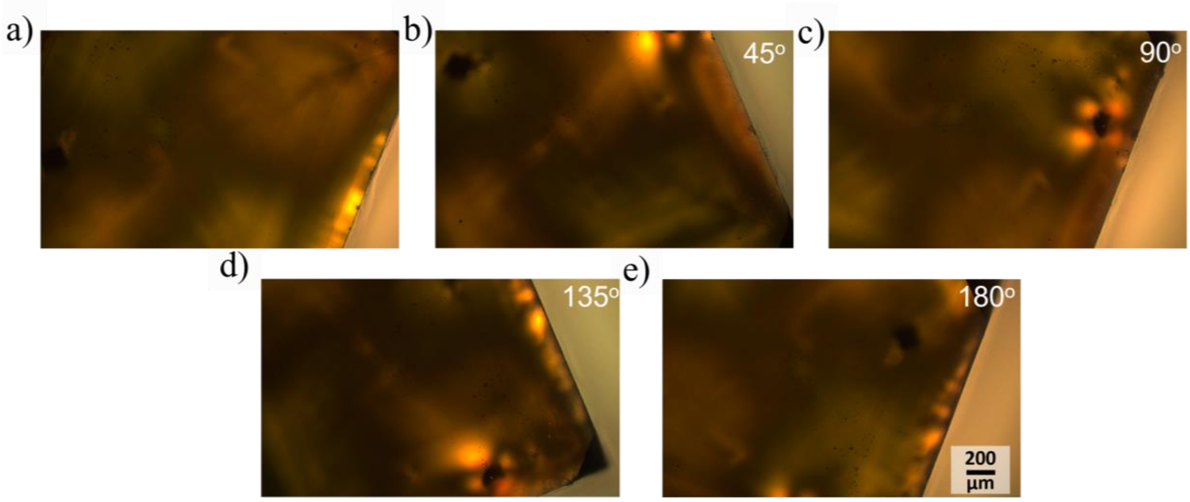

Fig. 4.20 B/N co-doped diamond grown with B concentration 2500 ppm on SCD Ib substrate for different angles between the sample and the polariser: a) 0°, b) 45°, c) 90°, d) 135°, e) 180°.

In the previous works, it was measured and simulated that this kind of pattern is indicated by a bundle of dislocations [160], [163]. L. Hoa et al. [164] modelled dislocations in diamond using Burgers vectors to obtain a similar pattern to the one seen in the measurements. Similar simulations have been presented by H. Pinto et al. [163]. They showed that the shapes and number of petals in the birefringence pattern depend on the dislocation types.

Despite the existence of techniques that will give more qualitative and quantitative information about the structure of grown-diamond, microscopy remains the simplest and a very fast method by which the quality of grown samples can be determined. Furthermore, measurements of the diamond provided an insight into the capabilities of the polarised-light microscope. The microscope also has its limitations. Due to the magnifications available, lesions and defects that are much smaller than the surface under study cannot be seen in the microscopic image. In addition, for inhomogeneous samples with different layer heights, it is not always possible to obtain a sharp image for the highest magnifications. Beyond these limits, the polarised-light microscope is suitable for detecting birefringence with sufficient accuracy to be used for FLBP.

4.3.1 Polarisation analysis of few-layer black phosphorus

The polarised microscopy setup was used to analyse the anisotropic properties of FLBP. Samples were prepared using liquid (FLBP-0k$_{DMF}$) and mechanical (FLBP-0k$_{MEC}$) exfoliations, as described in sections 4.1.2 and 4.1.3, respectively.

Samples were placed between crossed-polarisers and rotated to obtain polarisation images as a function of the rotation angle. A halogen lamp was used to collect information about the birefringence of FLBP. Additionally, mechanically exfoliated FLBP was measured using monochromatic light to observe its dichroic properties. The measurements were repeated over several days to observe how the degradation of the material affects the polarisation properties.

The FLBP-0k$_{DMF}$ deposited on the Si substrate was placed in a chamber (Linkam HFS600) to control the environmental conditions (such as the temperature and the atmosphere) and slow the degradation of the BP layer. For the first three days, FLBP was in a nitrogen atmosphere. Then the chamber was opened, and the FLBP was exposed to ambient conditions to compare the rate of oxidation. Microscopic and birefringence images of the FLBP-0k$_{DMF}$ were collected (Fig. 4.21). The birefringence images were recorded for rotational angles from 0^{o} to 360^{o} with a 10° step. The red rectangle in Fig. 4.21a marks the area shown in the polarised images with different rotation angles (Fig. 4.21b–f). The intensity of the BP flakes changes with the rotation, while the background intensity remains constant. Similar results were observed by H. Yang et al. [130].

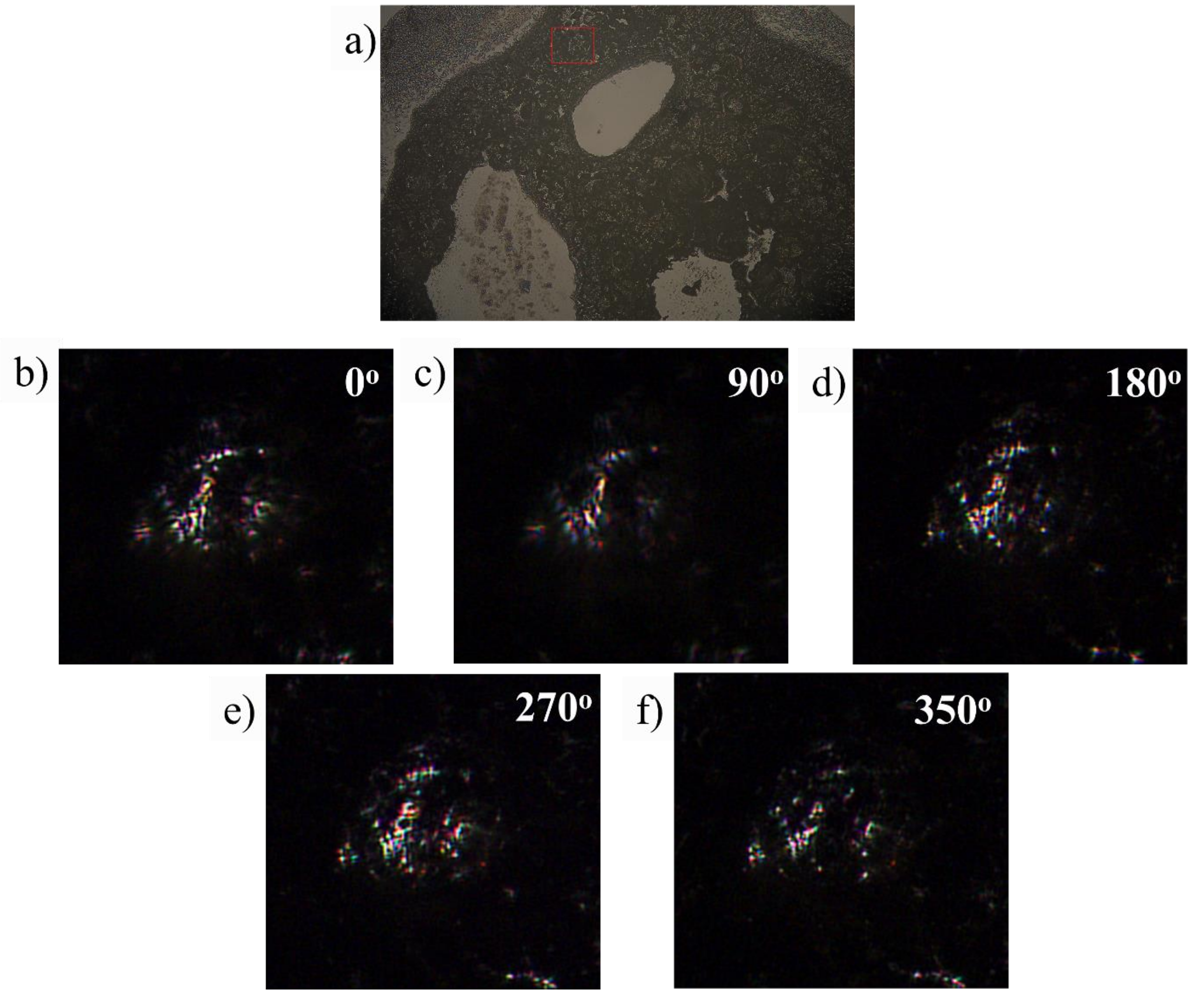

Fig. 4.21 a) Microscopic image of liquid-exfoliated FLBP. B–f) Polarisation images of the region marked with a red rectangle as a function of rotation angle.

The red, green and blue (RGB) values were extracted from the polarisation images of the FLBP-0k$_{DMF}$ (Fig. 4.22) to check changes for different wavelengths. The RGB intensities as a function of the rotational angle are presented in Fig. 4.22e. They are characterised by slow periodic variation, which is in agreement with previous works [130], [131]. Furthermore, the characteristics are almost identical for all channels, only small variations in the intensity are visible. Despite the fact that phosphorene has an anisotropic structure [50], the intensity of individual peaks does not differ significantly from each other. This is due to the fact that the layer prepared by liquid exfoliation consists of multiple flakes superimposed on each other with a random orientation.

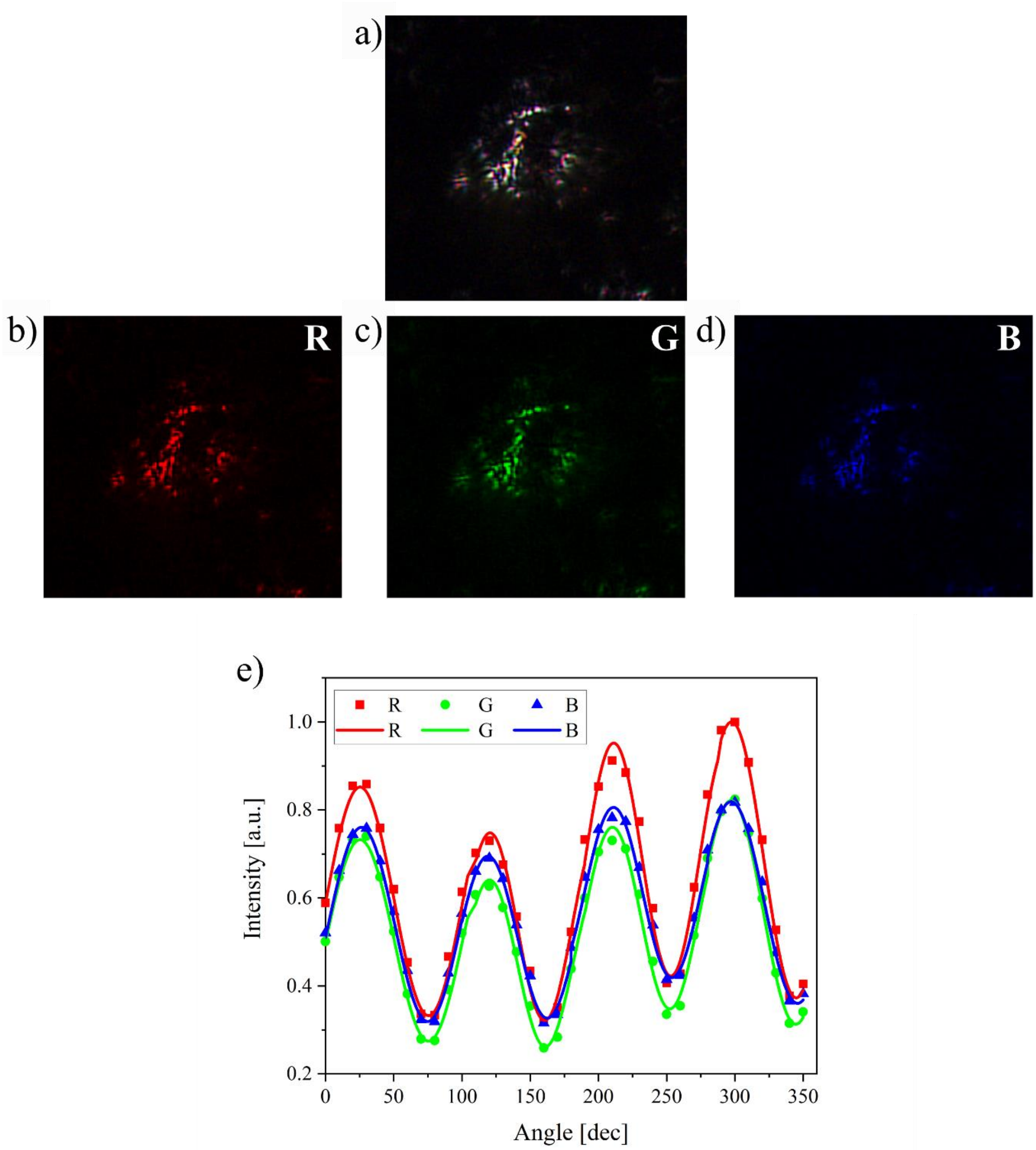

Fig. 4.22 a) Polarisation image of FLBP-0k$_{DMF}$. b) Red (R), c) green (G), and d) blue (B) image extracted from the image at a). e) The intensity of RGB channels as a function of the rotation angle.

The measurements were repeated for several consecutive days (Fig. 4.23). The intensity changes determined from day to day varied similarly for all three channels. For the first 3 days, the signal decreased slightly. On the day 3, the measurement was made with FLBP-0k$_{DMF}$ closed in the chamber controlling the atmosphere. It was then taken out and left in the air for 3 hours and the measurement was repeated (day 3$_B$). The resulting signal differed slightly from those obtained when FLBP was closed in the chamber. On the day 4, the intensity suddenly jumped sharply (Fig. 4.23).

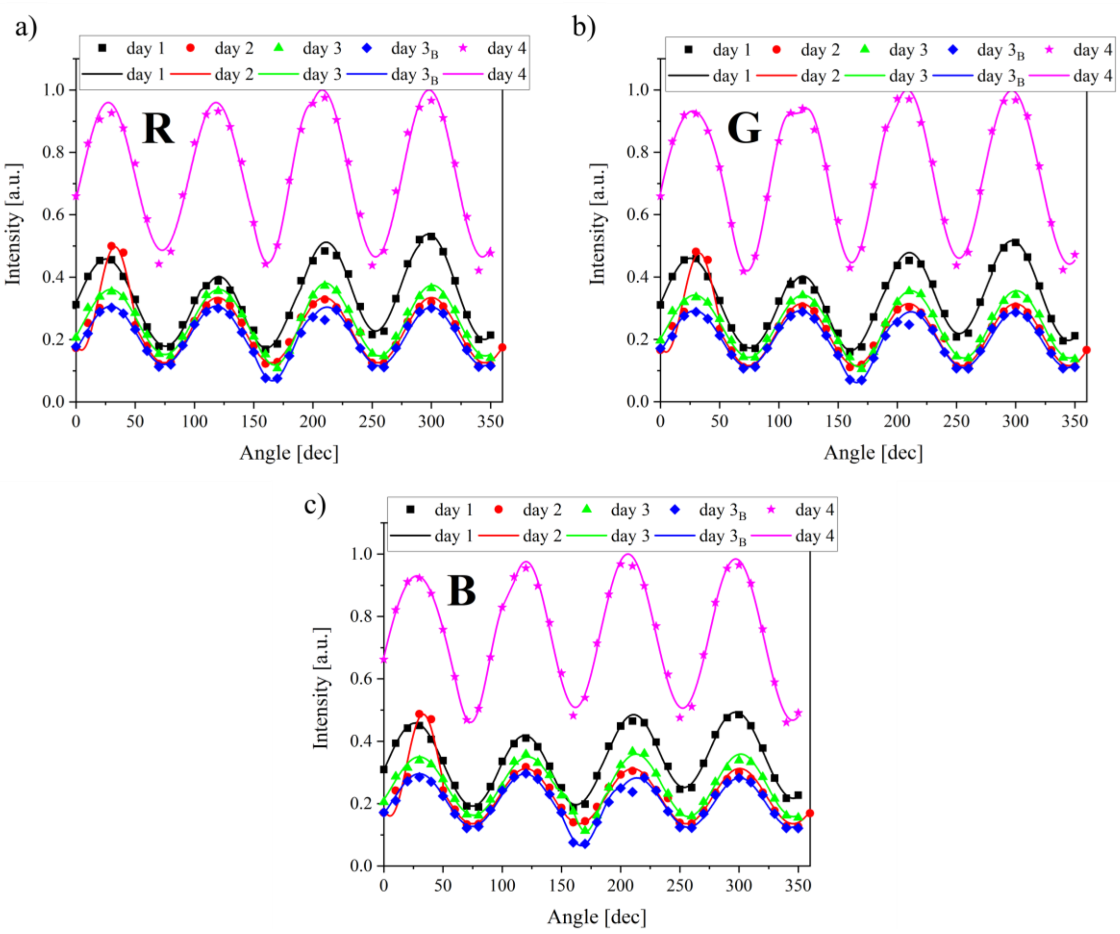

Fig. 4.23 FLBP-0k$_{\mathrm{DMF}}$ averaged intensity values from polarisation images as a function of angle changes in time for a) red (R), b) green (G), and c) blue (B) channel.

The polarisation properties of the FLBP were not significantly affected by the oxidation process, which is consistent with the findings of W. Shen et al. [165]. However, it did cause changes in the intensity. Layer thickness changes during degradation, possibly due to the appearance of a PxOy layer, appear on the BP surface. This could lead to interference of incident light on the sample, which explains the sudden signal spike observed on day 4 of the measurements [165], [166].

The measurements were repeated for mechanically exfoliated FLBP – FLBP$_{\mathrm{MECH}}$ – however, they were carried out entirely under ambient conditions. The exfoliation process is shown in Section 4.1.3. The microscopic and polarisation images are presented in Fig. 4.24. The microscopic image highlights a flake that is transparent in daylight (Fig. 4.24a). Only viewing it through crossed polarisers (Fig. 4.24b–f) shows its optical anisotropy.

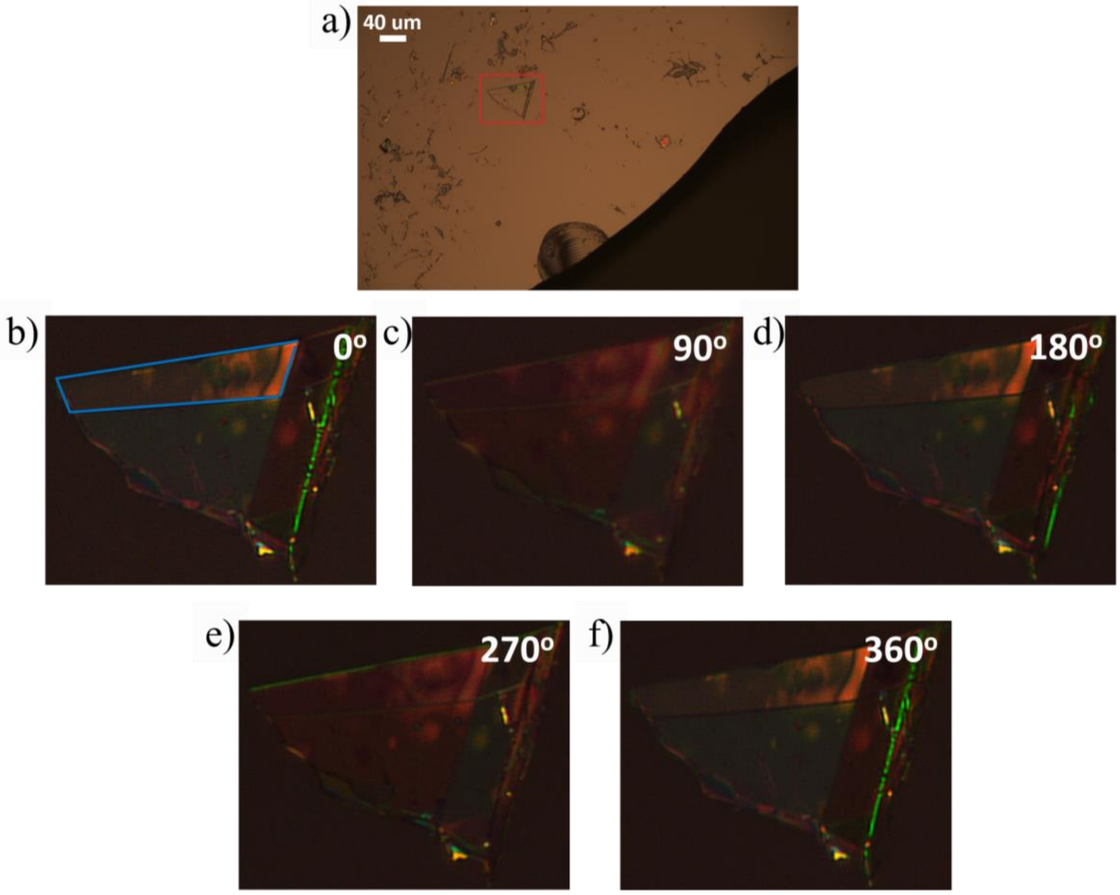

Fig. 4.24 a) Microscopic image of mechanically exfoliated FLBP$_{MECH}$. b–f) Polarisation images of the region marked with a red rectangle as a function of the rotation angle. The region more responsive to changes in the rotation angle is marked with blue rectangle.

The intensity as a function of the rotation angle for the BP flake and the substrate are shown in Fig. 4.25. RGB channels were extracted as the average change from the entire flake. As can be seen, the intensity level for Si is low and changes slightly as a function of the angle. However, the BP flake exhibits an intensity change with respect to the rotation angle, which takes on a periodic shape, indicating the presence of birefringence in FLBP [130], [131]. The highest intensity occurs for an angle of ~125°, which may indicate the AC orientation [167]. The largest intensity changes occurred for the R channel. In contrast, for the G and B channels, these changes are similar. Irregularities on the FLBP surface may be the cause of the difference among the RGB channels. Microscopic images of Fig. 4.7 in Section 4.1.3 show that the studied surface consists of several flakes superimposed on each other. The colour changes in the polarisation images (Fig. 4.24b–f) also indicate the different thickness of the analysed surface.

The upper part of the BP flake (marked in Fig. 4.24b) is more responsive to changes in the rotation angle, which suggests that this area is thinner than the others.

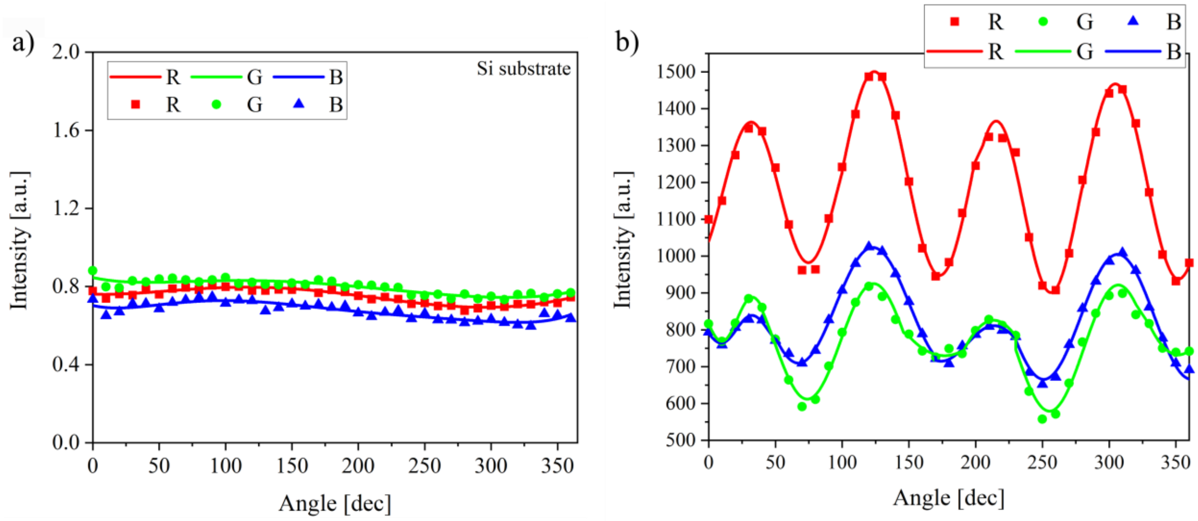

Fig. 4.25 Averaged red-green-blue (RGB) intensity values from polarisation images as a function of the angle for a) the background and b) the BP flake.

Measurements were repeated for several consecutive days, as well as a month later, to observe changes in the intensity over time. The characteristics of the RGB channels are shown in Fig. 4.26a–c, respectively. Variations in the intensity are visible for all channels. However, for the R and G channels, the changes are similar. The most significant intensity changes were noticed in channel B. It’s noteworthy that the intensity increased at the start over time (between days 1 and 2), which is consistent with the measurements for liquid-exfoliated FLBP. In the subsequent days, the signal started decreasing, with the maximum reduction observed after 35 days. As BP degrades, it forms PxOy [57], [59] oxides on its surface. These oxides are thicker than the BP layer. As a result, this interference with reflected light causes a change in its intensity [165].

In the last measurement (after 35 days), the signal was still characterised by periodic variation, however the differences in peak intensity were no longer observed (Fig. 4.26). This may be due to covering the entire FLBP with a layer of phosphorene oxide.

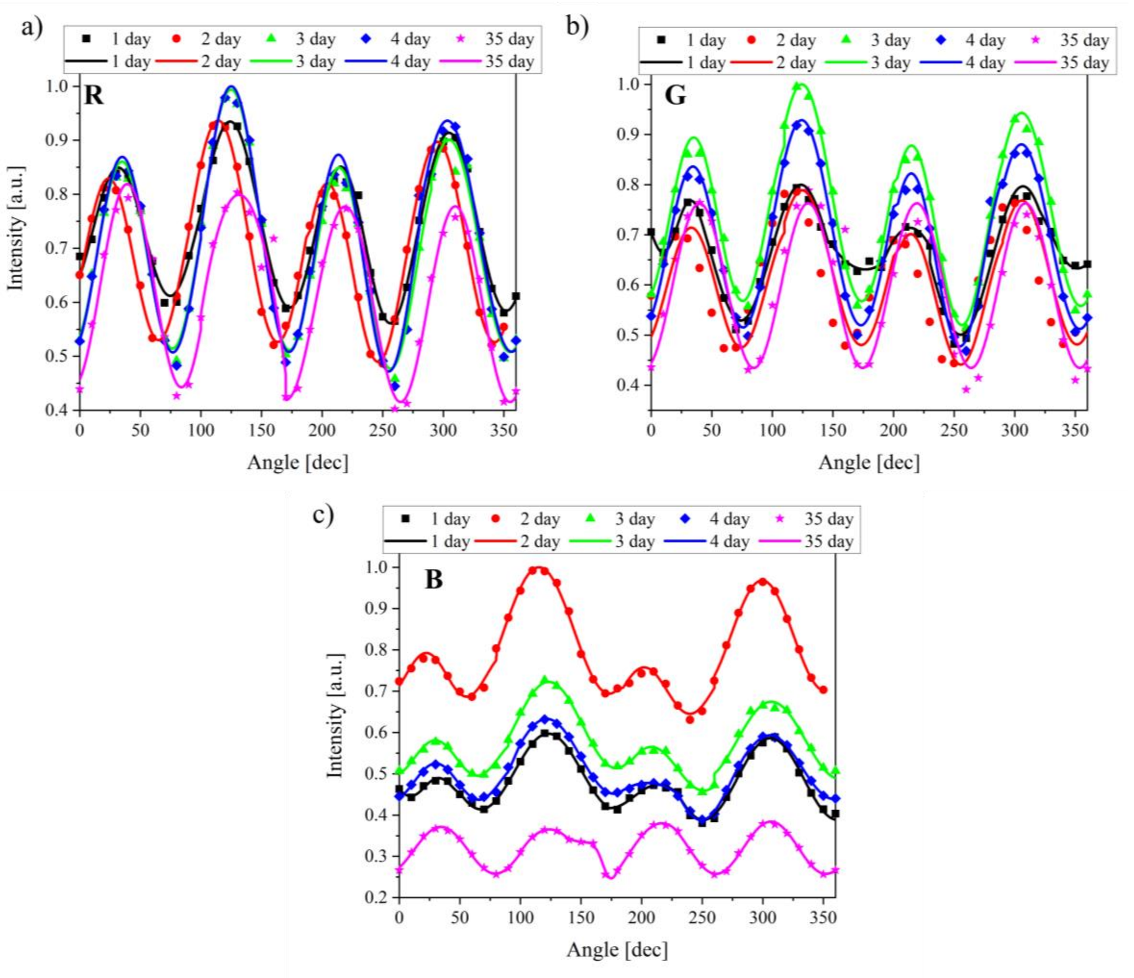

Fig. 4.26 BP flake averaged intensity values from polarisation images as a function of angle changes in time for a) red, b) blue, and c) green channel.

Then, the source of light was changed to the green diode pumped laser modules (532 nm) and mechanically exfoliated FLBP$_{MECH}$ was measured again from 0° to 360° to characterise the dichroism properties. The optical brightness changes significantly with the rotational angle (Fig. 4.27).

The highest intensity was observed at an angle of approximately 161°, which is the angle between the sample and the crossed polarisers. This angle remained constant in subsequent measurements. The direction obtained corresponds to the AC direction on the crystal axis of the BP flake [131]. However, there was a notable decrease in signal intensity between the initial and second measurements. In the following days, the intensity showed a slight increase compared to its value on day 2. The changes occur as a result of BP sample oxidation, which is most significant during the first few hours. After the sample surface has undergone oxidation, the process slows down [168].

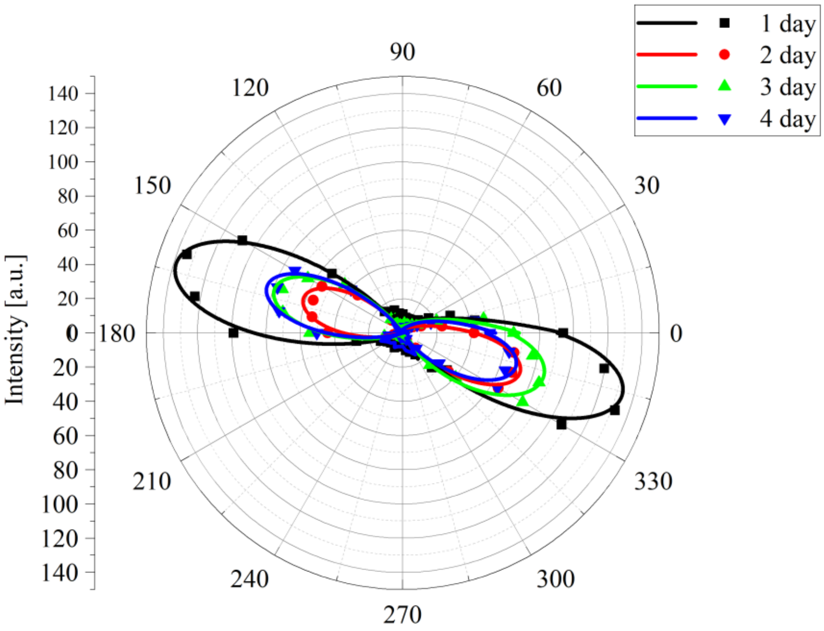

Fig. 4.27 FLBP optical intensity as a function of rotation angle for four consecutive days.

The intensity no longer changed when measured after a 35 days of keeping the $FLBP_{MECH}$ under ambient conditions but without access to light. However, the direction of maximum intensity shifted to 176° (Fig. 4.28).

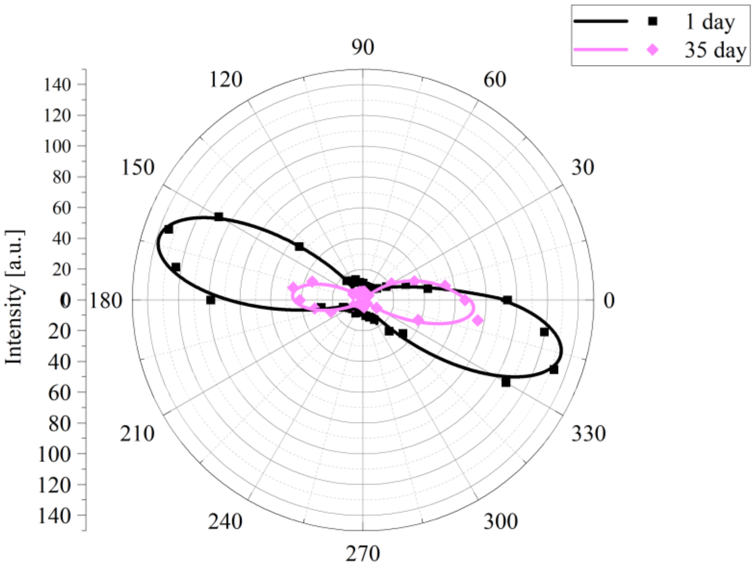

Fig. 4.28 Comparison of FLBP optical intensity as a function of rotation angle on the first day and after 35 days.

At this stage, the surface of the BP flake is completely covered with an oxide layer. It has been shown that when water is present in the air, phosphorus oxide turns to acid, further accelerating the degradation of BP [59]. The acid and oxide layers and the thinning of the BP layer may have influenced the shift in the crystal axis angle. But since the anisotropy is apparent, it can be inferred that the BP has not completely transformed into oxide.

The effect of the oxidation process in the first few days after BP exfoliation on its polarisation properties was demonstrated. The degradation process did not affect the occurrence of anisotropy in the FLBP layer from the onset, as confirmed in W. Shen et al.'s research [165]. Changes in the angle of highest intensity become noticeable only after significant degradation of the layer. The oxidation process, in turn, affects the intensity of the reflected light (hypothesis II) due to the changes in the thickness of the film being studied.

4.4 Black phosphorus – zinc oxide sensors to detect metal ions – design and investigation

In this chapter, a black phosphorus – zinc oxide sensor to detect metal ions with different concentrations is presented. In section 4.9.1, the photoluminescence set-up was described. Section 4.9.2 presents the investigation of electrochemical sensors with zinc oxide – black phosphorus as a working electrode. The sensors' designs were developed in collaboration with Dr. Roman Viter from the University of Latvia, while the author exclusively obtained all results.

4.4.1 Photoluminescence sensor redouts

As was mentioned in section 2.4, metal ions play an important role both in the human body and in the environment. Research is constantly being done to improve and find sensors that detect ions faster and with greater accuracy. Various techniques are used for this purpose, e.g. photoluminescence [138]–[140]. Photoluminescence is the light emitted from a material under optical excitation. Sensors using this technique are characterised by high sensitivity and selectivity [169], [170].

Phosphorene was also found to be sensitive to metal ions [82]. However, the PL of BP with more than three layers is in the far IR range, which can be detected by spectrometer or special detectors but not by, e.g., cheaper silicon detectors. The idea was to develop a material with a PL response in the VIS or NIR and mix it with FLBP. Hence, zinc oxide nanorods (ZnO NRs) were proposed because their PL is the range from 354 nm to 827 nm (Fig. 4.9 in section 4.1.5) and ZnO-decorated BP has already been shown for sensing purposes as well [171]. Finally, zinc is easily absorbed by BP and further increases its stability in air [172]. In the measurements, BP mixed with ZnO NR (3kBP-ZnO NRs) and b-AsP mixed with ZnO NR (b-AsP-ZnO NRs) were used. The sample preparation procedures are described in section 4.1.5.

The designed PL sensor system is presented in Fig. 4.29. It consists of two syringe pumps – one with a probe with different concentrations of metal ions and the second with water. The sample was closed in a special chamber and illuminated by a LED and then the photoluminescence signal was detected by the USB4000 detector from Ocean Optics. At the beginning, water was run through the sample until the signal stabilised. Next, the flow was switched to the syringe with Zn^{2+} and left until the signal stabilised. After recording the signal, the flow was changed to water again.

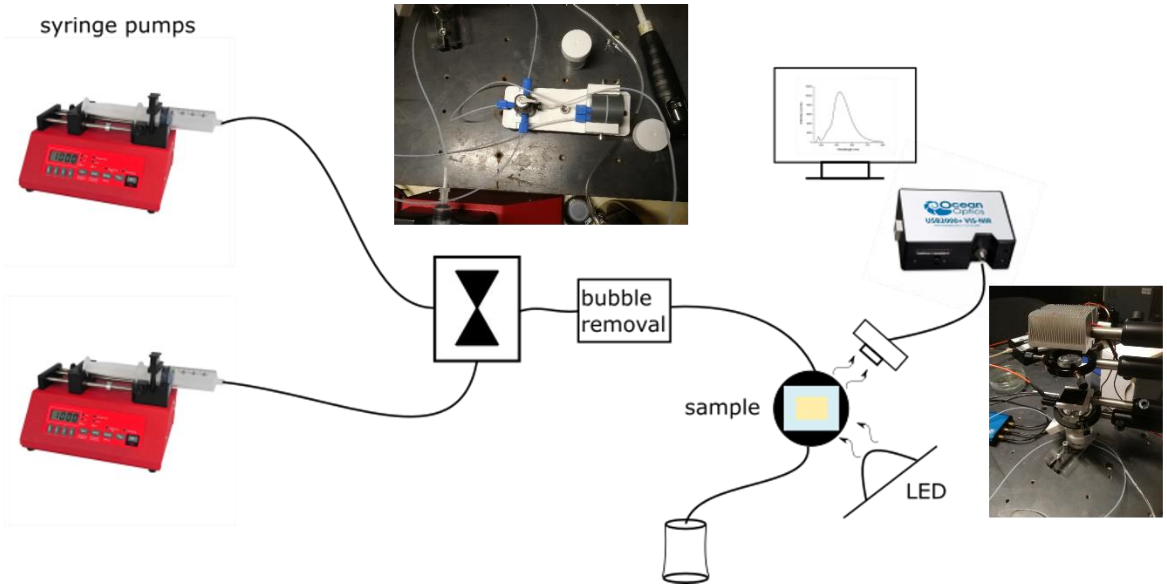

Fig. 4.29 Photoluminescence sensor setup based on ZnO-BP to detect metal ions.

In the research, the sensitivity to zinc, calcium, magnesium, sodium, and copper ions was checked. Different concentrations of them were prepared by mixing water and ZnF_2, $Zn(NO_3)_2$, $Ca(NO_3)_2$, MgCl, NaF, or $CuSO_4$ salts.

ZnO NRs on a Si substrate was used in the measurements as a reference. Its response to three concentrations of Zn^{2+} – 0.3 pM, 0.2 nM, and 65 nM – were recorded and is presented in Fig. 4.30a. After each addition of subsequent concentrations of ions, the sample was left until the signal stabilised to make sure that the changes come from a change in the ion concentration and not from the syringe pump switching itself. In Fig. 4.30a, slight changes in the spectrum can be observed. The black arrows indicate the wavelengths (382 nm, 447 nm, and 520 nm) at which the peaks occur, and which were chosen to check the change in intensity over time, presented in Fig. 4.30b–d. Red arrows indicate when the probe was switched to the syringe with ions and blue arrows when it was switch to the syringe with pure water.

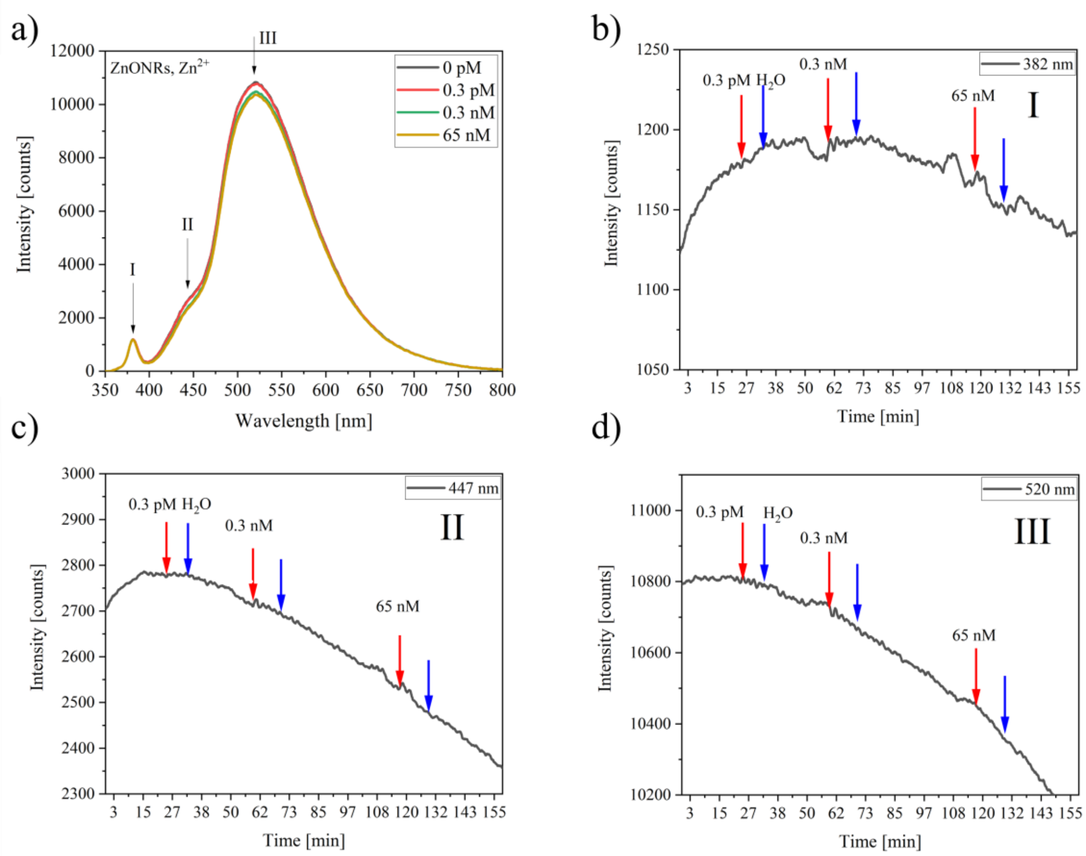

Fig. 4.30 a) Photoluminescence spectra of ZnONRs under the influence of zinc ions of different concentrations, and the PL signal changes in time at b) 382 nm, c) 447 nm, and d) 520 nm. Red arrows indicate when the flow was switched to the syringe with ions; blue arrows – when it was switched to the syringe with pure water.

The intensity constantly decreased in time. Due to the LED power being too high, the photocatalysis [173] process occurred and accelerated the degradation of the sample. This is especially visible for the peak at 447 nm (Fig. 4.30c). The addition of the metal ions also caused no change in the signal, which suggests a lack of sensitivity to Zn^{2+} in small concentrations. Hence, the next step was checked higher concentrations of Zn^{2+} and the sensitivity to other metal ions. The results are shown in Fig. 4.31.

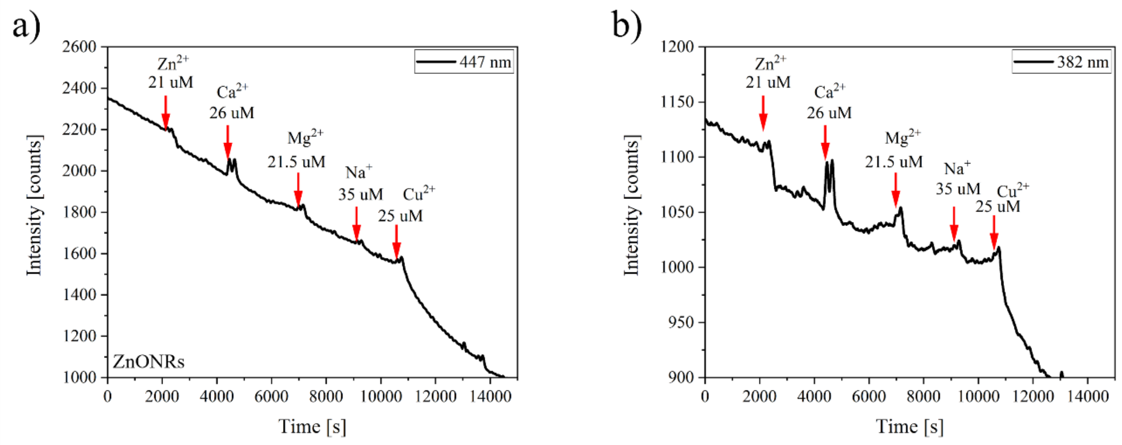

Fig. 4.31 Changes of PL signal of ZnO NRs at a) 382 nm and b) 447 nm the under influence of Zn^{2+}, Ca^{2+}, Mg^{2+}, Na^{+} and Cu^{2+}. Red arrows indicate when it was switched to the syringe with different ions.

When a 21 μM concentration of Zn^{2+} was added, the intensity decreased slightly but did not return to the previous level. After adding Ca^{2+}, the signal increased and formed two peaks, to drop to the previous level a moment later, before the probe was switched to water. For the rest of the metal ions, the PL signal also increased, but this was not as significant as for Ca^{2+} and quickly returned to the previous level. ZnO nanoparticles willingly absorb Zn^{2+} ions, however, the adsorption capacity increases with the increasing ion concentration [174]. Therefore, at low concentrations, no signal changes may have occurred, and a decrease was observed at 21 μM.

Next, the 3kBP-ZnONRs on a Si substrate was measured to check its sensitivity to Zn^{2+} and Mg^{2+}. The spectra recorded for different Zn^{2+} ion concentrations are presented in Fig. 4.32a. With the increasing ion concentrations, the intensity decreased at 520 nm. Simultaneously, changes in the PL signal in time were recorded at 381 nm, 446 nm and 520 nm (Fig. 4.32b–d). After adding 1 pM of Zn^{2+} ions, the signal increased and formed two peaks, and then the intensity dropped to the previous level. Switching the flow to water has no influence on the PL signal. Adding 2 pM and 1 nM of Zn^{2+} ions causes no change in the intensity of the signal for all three peaks (Fig. 4.32b–d).

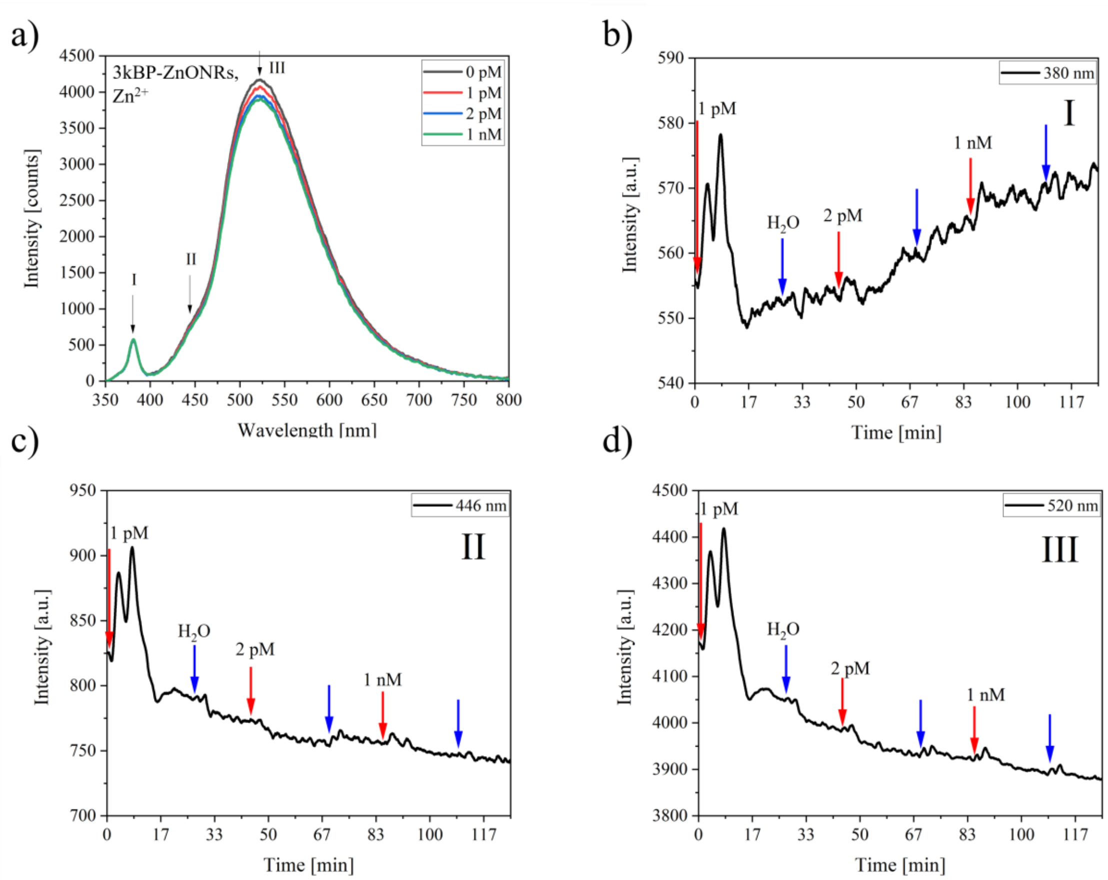

Fig. 4.32 Photoluminescence spectra of 3kBP-ZnO NRs under the influence of zinc ions with different concentrations, and the PL signal changes in time at b) 381 nm, c) 446 nm, and d) 520 nm. Red arrows indicate when the flow was switched to the syringe with ions; blue arrows when it was switched to the syringe with pure water.

Similar results were obtained when detecting Mg^{2+} (Fig. 4.33). Adding the 1 nM of Mg^{2+} caused the PL signal to increase. In contrast to the measurements with Zn^{2+}, here, the intensity level was maintained until switching to the pure water syringe pump, causing the signal to drop. Similar results were observed for the 48 nM of Mg^{2+}, but after changing to pure water, the signal dropped to a higher value than before. For the 8 nM of Mg^{2+} and subsequent concentrations, the PL spectrum stopped changing.

Both the ZnONRs and 3kBP-ZnONRs electrodes were found to be sensitive to metal ions. But the ions reacted with the surface of the samples, modifying them, which resulted in there being no reaction after increasing the ion concentration. This is particularly noticeable when measuring Mg^{2+} using 3kBP-ZnONRs. The signal not only reacted to the appearance of the ions but also to their disappearance (switching to water), but it dropped to a higher level each time until it stopped reacting to the increasing concentration of Mg^{2+} ions.

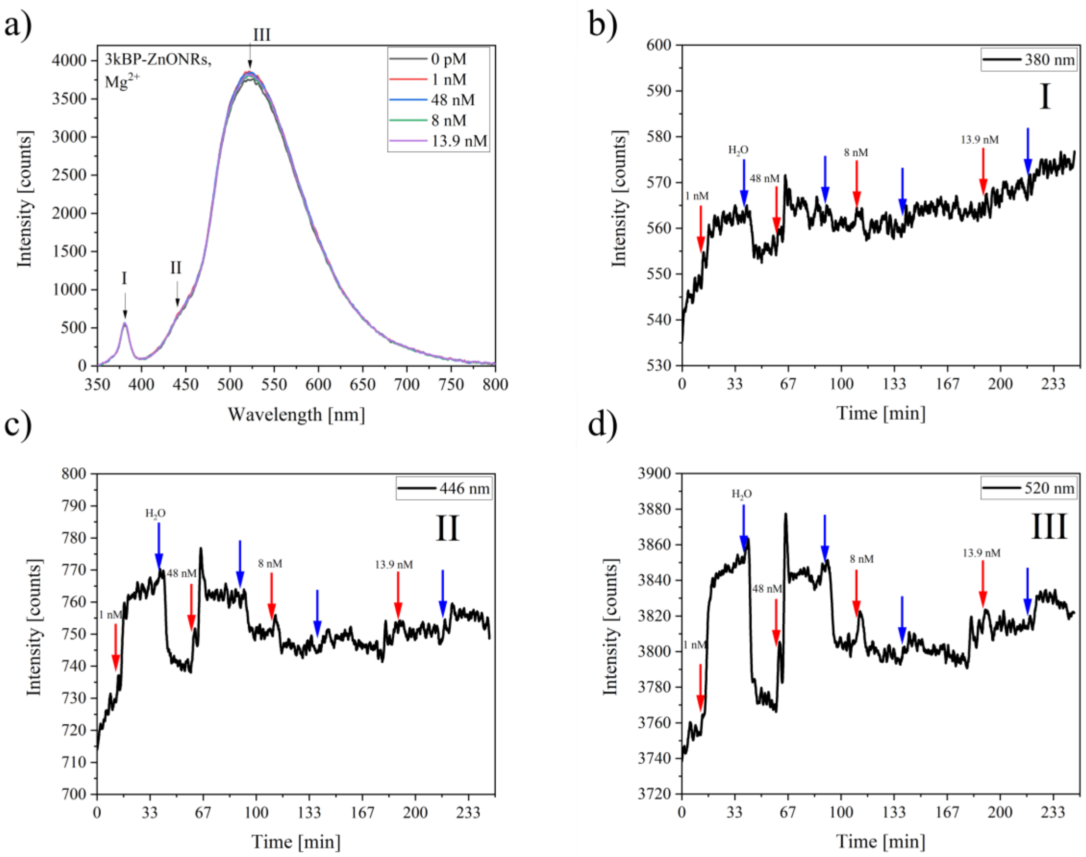

Fig. 4.33 a) Photoluminescence spectra of 3kBP-ZnO NRs under the influence of magnesium ions with different concentrations, and the PL signal changes in time at b) 380 nm, c) 446 nm, and d) 520 nm. Red arrows indicate when the flow was switched to the syringe with ions; blue arrows when it was switched to the syringe with pure water.

The sensitivity of b-AsP-ZnONRs to metal ions was also checked. First, the PL spectra for a 260–580 μM concentration of Zn^{2+} ions were recorded (Fig. 4.34a). With the increasing ion concentration, the PL signals decreased. This is clearly visible at peaks marked II and III in Fig. 4.34a. The PL spectrum for 0 nM of Zn^{2+} ions was recorded at the beginning and the end of the measurements. The intensity decreased during the measurement, indicating unexpected photocatalysis [173] and slight degradation of the b-AsP-ZnONRs under the influence of the ions.

Fig. 4.34b,c,d show changes in the PL signal in time at I-380 nm, II-440 nm and III-520 nm, respectively. After adding the 260 μM of Zn^{2+} ions, the signal dropped to a lower level. Without first switching to the pure water flow, the ion concentration increased first to 360 μM and then to 446 μM. As a result, individual peaks could be observed appearing. Next, after switching the flow to pure water, the signal increased to the initial level, only to decrease again when ions were added (Fig. 4.34b,c,d). b-AsP-ZnONRs shows a strong reaction to Zn^{2+} ions, however, no relationship between the ion concentration and signal changes was not found.

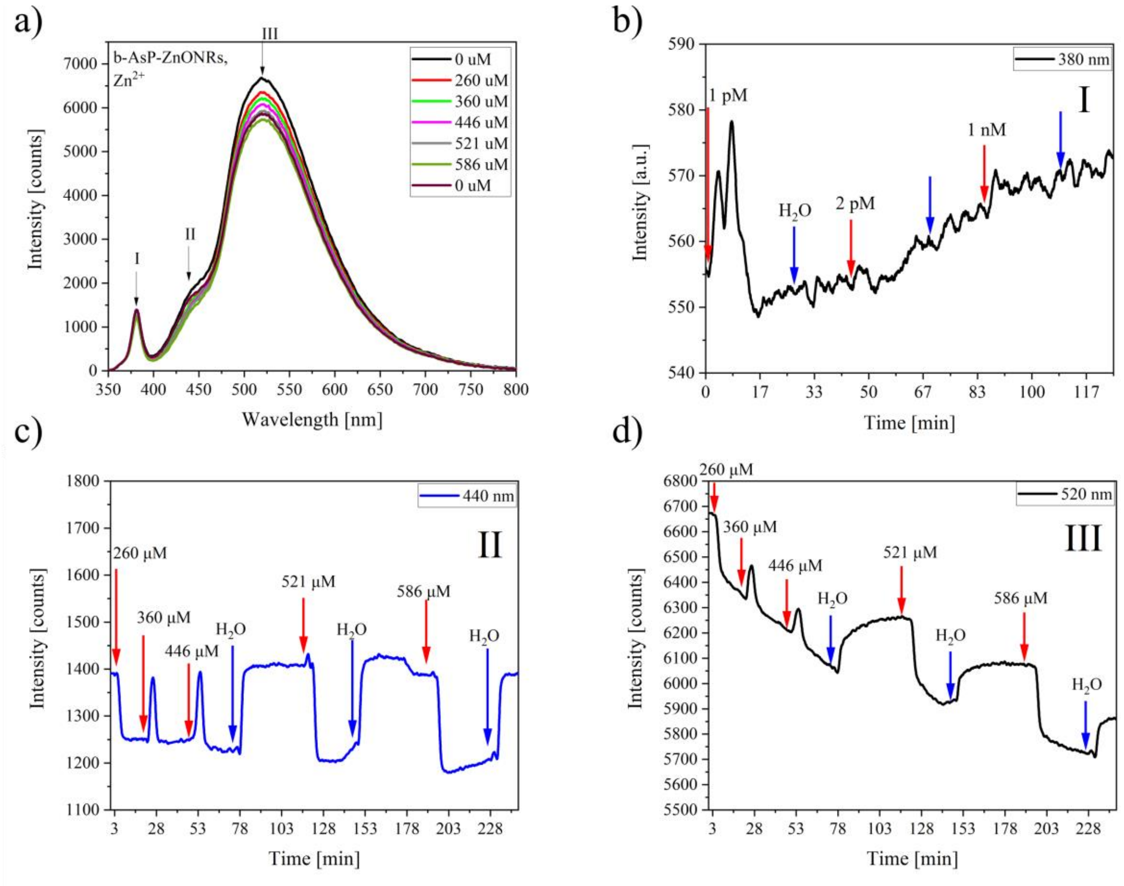

Fig. 4.34 a) Photoluminescence spectra of b-AsBP-ZnONRs under the influence of different concentrations of zinc ions, and the changes in the PL signal in time at b) 380 nm, c) 440 nm, and d) 520 nm. Red arrows indicate when the flow was switched to the syringe with ions; blue arrows when it was switched to the syringe with pure water.

The sensitivity of b-AsBP-ZnONRs to lower concentrations of Zn^{2+} ions was also investigated (Fig. 4.35). The intensity of the PL signal decreases sharply when the flow is switched to a syringe with Zn^{2+} ions. After switching to pure water, the signal returned to the previous level. There was only a successive decrease in the PL intensity for 520 nm (Fig. 4.35a), which could be a result of b-AsBP-ZnONRs degradation due to ion absorption or the LED illumination. However, these effects are not as devastating as for ZnONRs and 3kBP-ZnONRs.

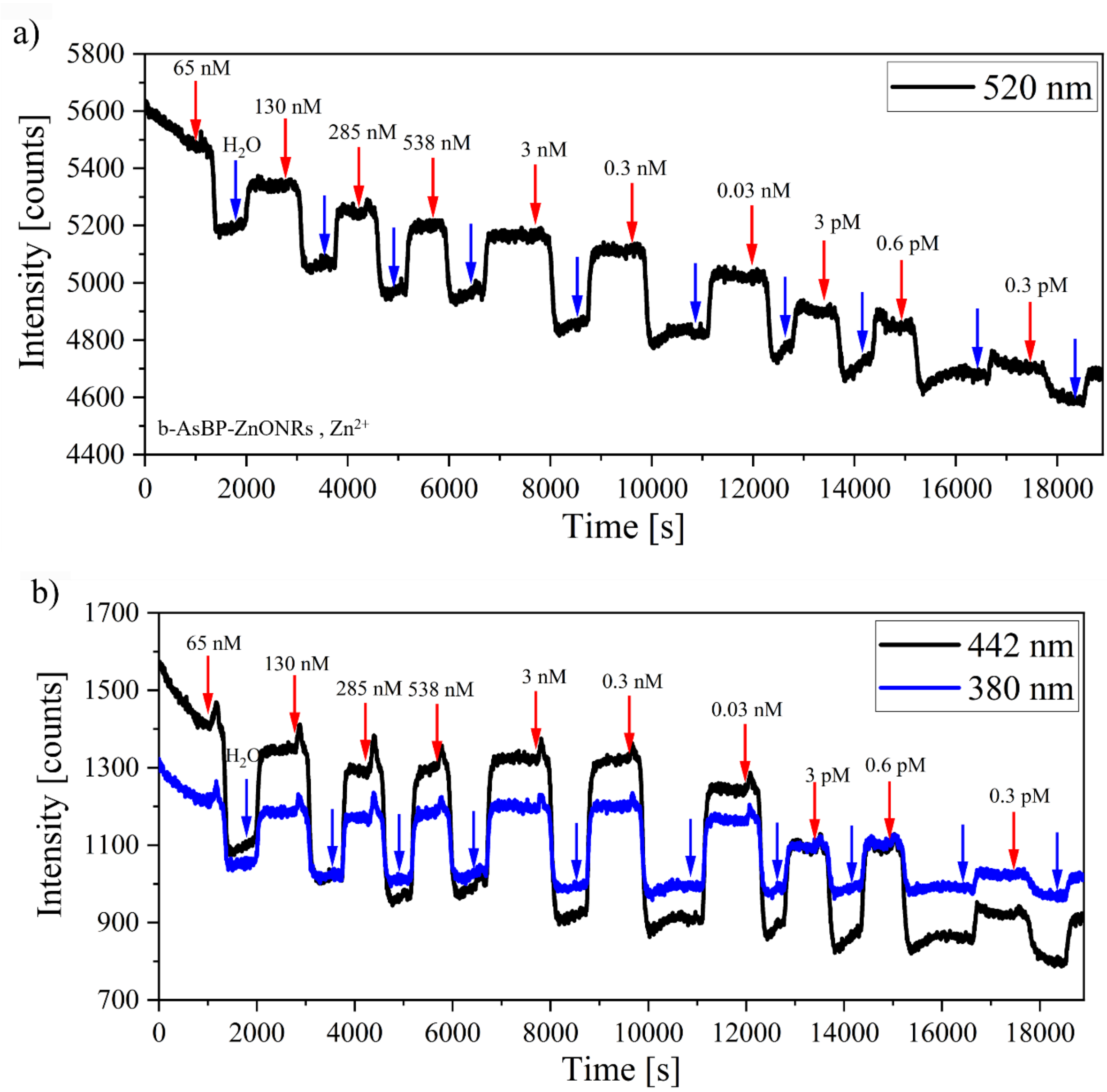

Fig. 4.35 Changes in the photoluminescence signal of b-AsBP-ZnONRs at a) 520 nm, b) 442 nm and 380 nm under the influence of Zn^{2+} with different concentrations. Red arrows indicate when the flow was switched to the syringe with ions; blue arrows when it was switched to the syringe with pure water.

The b-AsBP-ZnONRs was found to be more sensitive than previously known sensors [175]–[177], detecting even 0.6 pM of Zn^{2+} ions. Compared to previously known sensors, this value is lower. For instance, B. Rani and S. John demonstrated a fluorescent sensor that detects Zn^{2+} ions with a LoD of 5.1 nM [175]. However, in the PL sensor presented in this dissertation, no dependence can be determined between the ion concentrations and changes in intensity. In addition, b-AsP-ZnONRs was found to be more stable than ZnONRs and 3kBP-ZnONRs.

In conclusion, PL sensors based on composites of FLBP and b-AsP with ZnO NRs were prepared and their sensitivities to metal ions were checked. The presence of zinc and magnesium ions induces a change in the PL signal of BP as observed in the study. However, the ions modified the sample surface, which caused a reaction only to the first occurrence of ions, even at very low concentrations. The b-AsP with ZnO NRs, in turn, reacts to any change in the concentrations of Zn^{2+} ions (hypothesis III). Although the relationship between the ion concentration and the signal change cannot be determined, it has been shown that a BP- and b-AsP-based PL sensor can detect even small concentrations of ions**.**

4.4.2 Electrochemical sensor redouts

Another experiment focused on the construction and testing of a FLBP-based EC sensor. A typical three electrode system was applied. It consists of a working electrode, a counter electrode, and a reference electrode placed in an electrolyte [83]. Cyclic voltammetry (CV) was used, which involves sweeping the potential applied to the working electrode and observing how the resulting signal changes. The changes correspond to the reduction and oxidation processes of an electroactive species that can be adsorbed at the electrode surface.

To protect the FLBP against degradation, it was mixed with ZnO NFs [172], [178], then 3kBP-ZnO NFs and b-AsP-ZnO NFs deposited on ITO glass plates were used as working electrodes to determine various metal ions with different concentrations using cyclic voltammetry (CV). Their preparation is described in section 4.1.5. The EC setup is presented in Fig. 4.36. It contains a platinum wire as the counter electrode, Ag/AgCl in 3M KCl as the reference electrode and 3 mL of 10 mM $K_4[Fe(CN)_6]$ in 0.1 M phosphate buffer (PBS) as the electrolyte. PBS is widely used in biological sensor measurements [179], [180]. The measurements were made using a Wheeler Lab DStat potentiostat.

The potentiostat applies and controls the voltage to the working electrode vs the reference electrode and measures the current flowing between the counter and working electrodes. The potential range and scan rate were set at -500–800 mV and 50 mV/s, respectively. In one measurement cycle, 5 voltammograms were collected to be sure of the stability of the results.

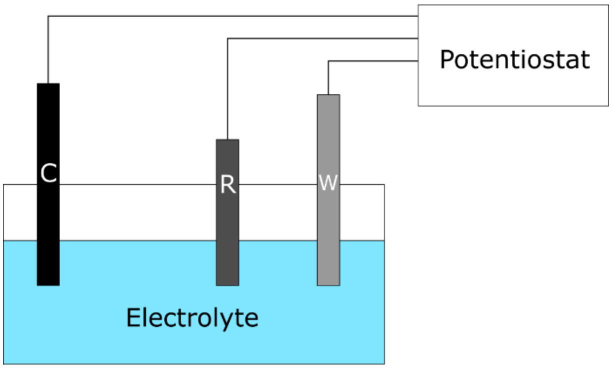

Fig. 4.36 Electrochemical sensor setup with a counter electrode (C), reference electrode (R) and working electrode (W) immersed in electrolyte and connected to a potentiostat.

An FLBP-based EC sensor was employed to identify the presence of Zn^{2+} and Mg^{2+} ions. As certain FLBP parameters can be adjusted through exposure to light [181], a white LED (1W, IPIXEL LED) was used to illuminate the working electrodes during measurements in order to assess the effect of light on BP's sensing capabilities.

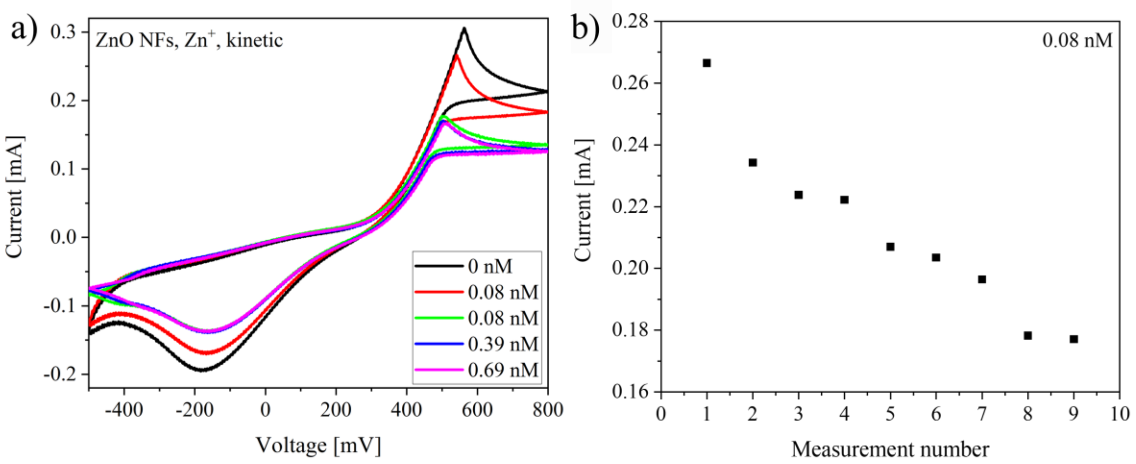

Fig. 4.37 a) CV response of the ZnO NFs electrode in $K_4[Fe(CN)_6]$ PBS electrolyte with different concentration of zinc ions. b) Change of current at the oxidations peak in the presence of 0.08 nM of Zn^{2+}.

At the beginning, the ZnO NFs on ITO glass was used as the working electrode to obtain reference values. Measurements were repeated five times without the presence of ions to check the stability of the electrode. The obtained signals were stable for every voltammogram. After adding 0.08 nM of Zn^{+} ions, the signal began to drop. Measurements were repeated until the signal stabilised (Fig. 4.37b). Next, the Zn^{2+} concentration was increased to 0.38 nM, then to 0.69 nM. Voltammograms from the first and the last cycle with 0.08 nM of Zn^{2+} ions, and from cycles with 0.38 nM and 0.69 nM of Zn^{2+} ions are presented in Fig. 4.37a). Despite the addition of higher concentrations of Zn^{2+} ions, the signal did not change.

Signal changes after the addition of Zn^{2+} ions indicate that the ions react with the electrode surface, but quickly saturate it so that changing the ion concentration does not affect further signal changes. Z. H. Ibupoto et. al have built Zn^{2+} ions sensor based on the ZnO that can detect ions in the range of 100 mM - 1μM with, which can be used several times [182]. The sensor presented here is disposable, but it can detect the presence of Zn^{2+} ions at very low concentrations (0.08 nM).

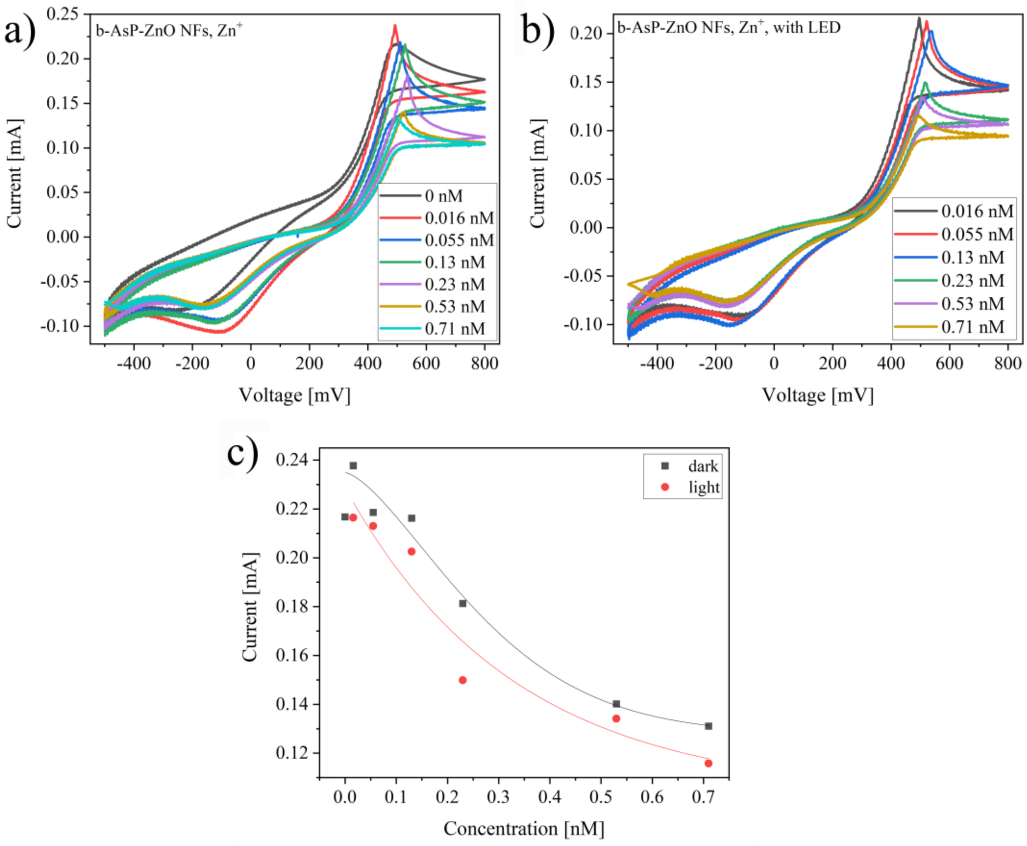

Fig. 4.38 Voltammograms for different concentration of zinc ions (0–0.71 nM) a) without LED and b) with LED illuminating the b-AsP-ZnONFs electrode. c) Current peaks from voltammograms for different concentrations of zinc ions without LED (marked on black) and with LED (marked on red).

Next, the b-AsP – ZnO NFs was used as a working electrode and its sensitivity to Zn^{2+} ions was checked (Fig. 4.38). The voltammograms were collected without (Fig. 4.38a) and with white LED illuminated the working electrode (Fig. 4.38b). The relationship between the peak current and the ions concentration is presented in Fig. 4.38c. The current from measurements with LED is generally lower, but both dependances are not linear.

The measurements with the b-AsP-ZnONFs electrode were repeated for higher concentrations of Zn^{2+} ions (Fig. 4.39). For concentrations lower than 1 nM, the dependency is similar to previous results. For concentrations higher than 1 nM, the current starts to flatten out.

The b-AsP increases the stability of the ZnO NFs-based electrode and changes in the concentration of Zn^{2+} ions can be also detected. But during measurements, the b-AsP-ZnONFs electrode wears out and cannot be used a second time. Nevertheless, it is possible to detect very small concentrations of Zn^{2+} ions (even lower than 1 nM).

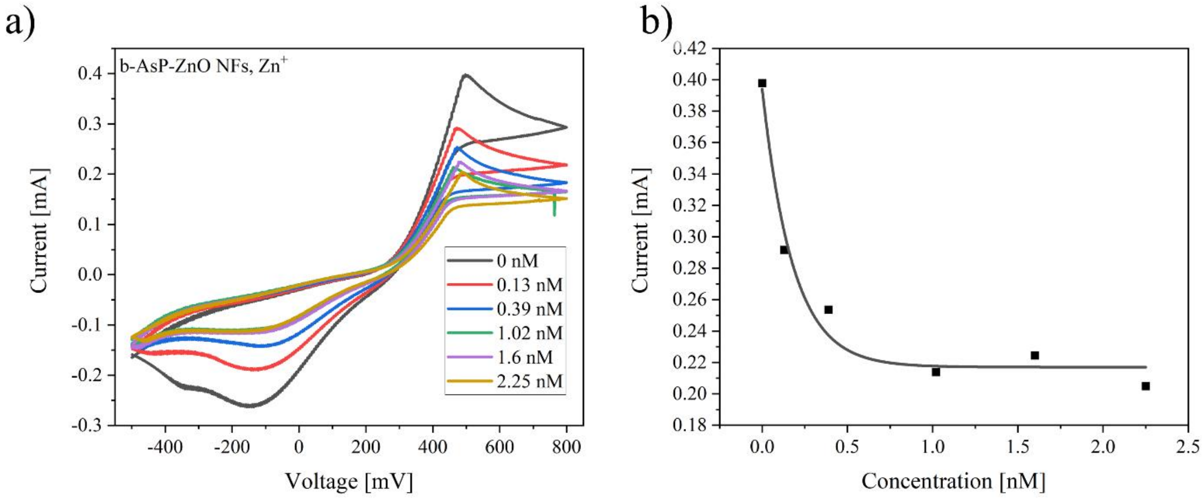

Fig. 4.39 a) Voltammograms for different concentrations of zinc ions (0–2.25 nM) with the b-AsP-ZnO NFs electrode. b) Current peaks from voltammograms for different concentrations of zinc ions.

Finally, how 3kBP affects the ZnO NF-based electrode was checked. Measurements were repeated five times in a pristine electrolyte with a 3kBP-ZnO NFs electrode as the working electrode. The voltammograms obtained were the same each time, indicating the stability of the electrode. Then, 0.16 nM of Zn^{2+} ions was added. The signal decreased compared to the signal collected without Zn^{2+} ions (Fig. 4.40) but stabilised and did not change in subsequent measurements. This suggests that mixing BP with ZnO NFs improved the electrode. The influence of the LED illuminating the working electrode was also checked. The signal decreases further compared to measurements without the LED (Fig. 4.40) but also stabilised at one level and the presence of Zn^{2+} ions did not result in a further decrease in the signal.

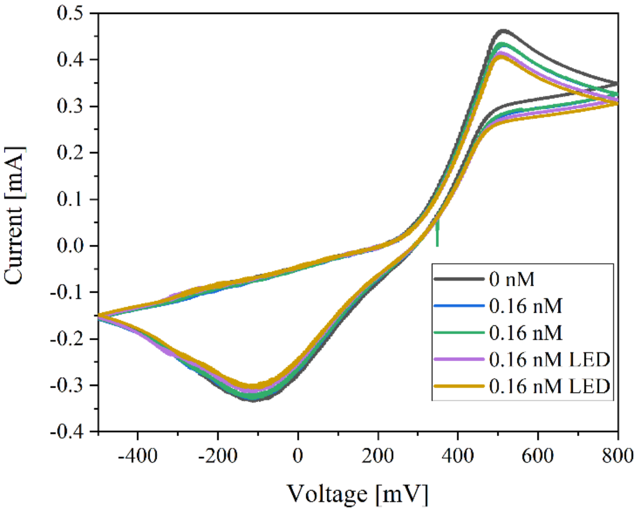

Fig. 4.40 a) CV response of the 3kBP-ZnO NFs electrode in $K_4[Fe(CN)_6]$ PBS electrolyte for a 0 nM and 0.16 nM concentration of Zn^{2+} ions without and with LED illuminating the electrode.

In the next step, the response to a concentration of 0–4 nM of Zn^{2+} ions was checked with the 3kBP-ZnO NFs as the working electrode. Fig. 4.41a,b presents the recorded voltammograms without and with light illuminating the working electrode, respectively. As can be seen the signal changed even at a concentration of 0.16 nM of ions. In both measurements, the current decreases as the ion concentration increases.

The maximum oxidation peaks are shown in Fig. 4.41c as a function of the Zn^{2+} ion concentration. A similar relationship between current and concentration can be observed for measurements without and with electrode illumination, but the current from the measurement under LED illumination is generally lower. For the lower concentrations (0–0.47 nM) the signal changes faster and reaches sensitivity at 0.144 mA/nM. For 0.47 nM and higher concentrations of Zn^{2+} ions, the sensitivity decreases to 0.02174 mA/nM. Moreover, the limit of detection (LoD) was calculated from the formula: $LoD = 3.3 \cdot (\sigma/S)$, where σ –standard deviation, and S – sensitivity. Considering two ranges of ion concentrations (above and below 0.47 nM), a separate LoD can be calculated and reaches: $LoD_{<0.47} = 0.05$ nM and $LoD_{>0.47} = 0.6$ nM. From 4 nM, the response starts to flatten. The results show that ions anchor to the surface of the electrode, influencing the flow of the charge. The calculated LoD is compared with other sensors in Table 4.5.

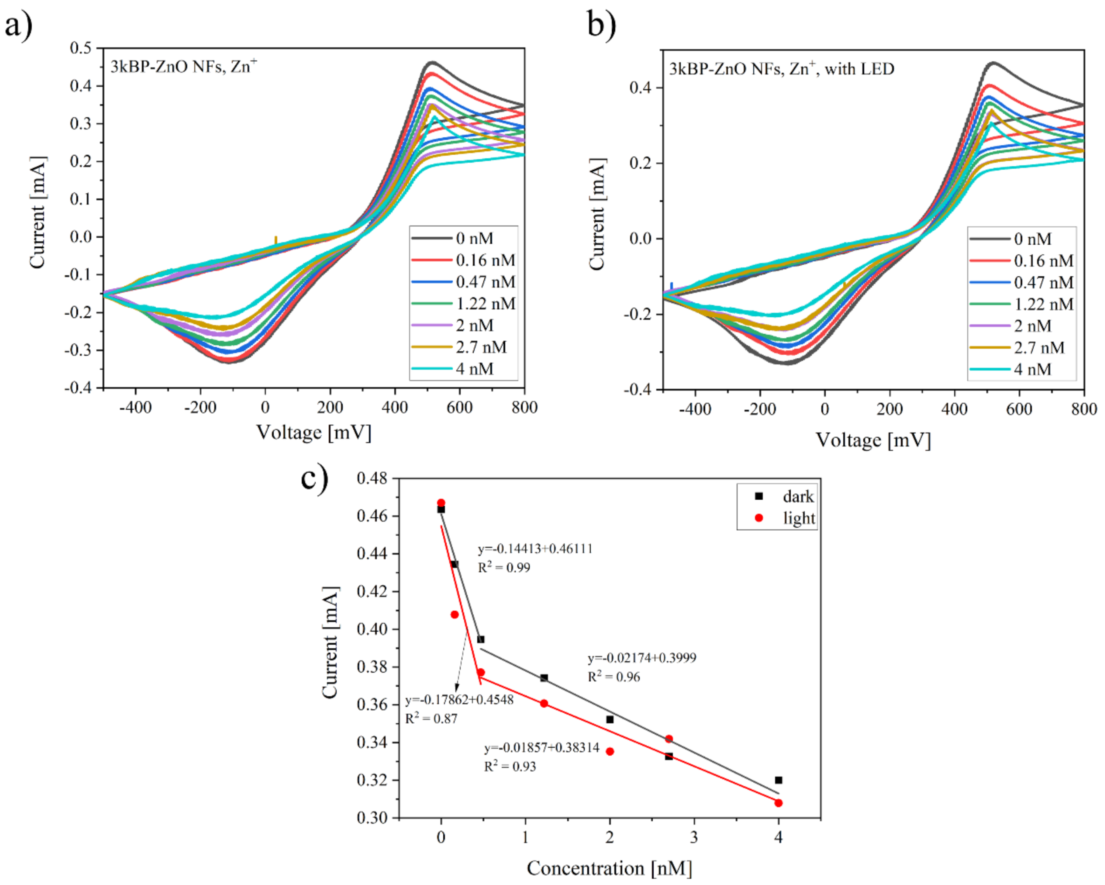

Fig. 4.41 Voltammograms for different concentrations of zinc ions (0–4 nM) a) without LED and b) with LED illuminating the 3kBP-ZnO NFs electrode. c) Current at the oxidation peak from voltammograms for different concentrations of zinc ions without LED (marked as dark) and with LED.

Table 4.5 Range and limit of detection of zinc ions for different method.

Zinc ions detection				
Material	**Range of detection**	**Limit of detection**	**Method**	**REF**
3kBP-ZnO NFs	<0.47 nM	0.05 nM	CV EC	This work
3kBP-ZnO NFs	0.47 nM – 4 nM	0.6 nM	CV EC	This work
ZnO nanorods with ionophore	1 uM - 100 mM		EC	[182]
graphene–polyaniline nanocomposite	1.5 nM – 4.6 µM	15 nM	EC SWASV	[183]
Hg–Bi/single-walled carbon nanotubes composite	7.6 nM – 168 nM	3.5 nM	EC Anodic stripping voltammetry	[184]
bismuth/poly(p-aminobenzene sulfonic acid)	15 nM – 1.7 µM	9.5 nM	EC	[185]
Clioquinol (5-chloro-7-iodo-8-hydroxyquinoline, CQ)	0.5 – 0.6 µM	1 nM	EC adsorptive stripping voltammetry (AdSV)	[186]

Next, 3kBP-ZnO NFs electrode was used to detect Mg^{2+} ions. The obtained voltammograms for a concentration of 0–1.3 nM ions are presented in Fig. 4.42a.

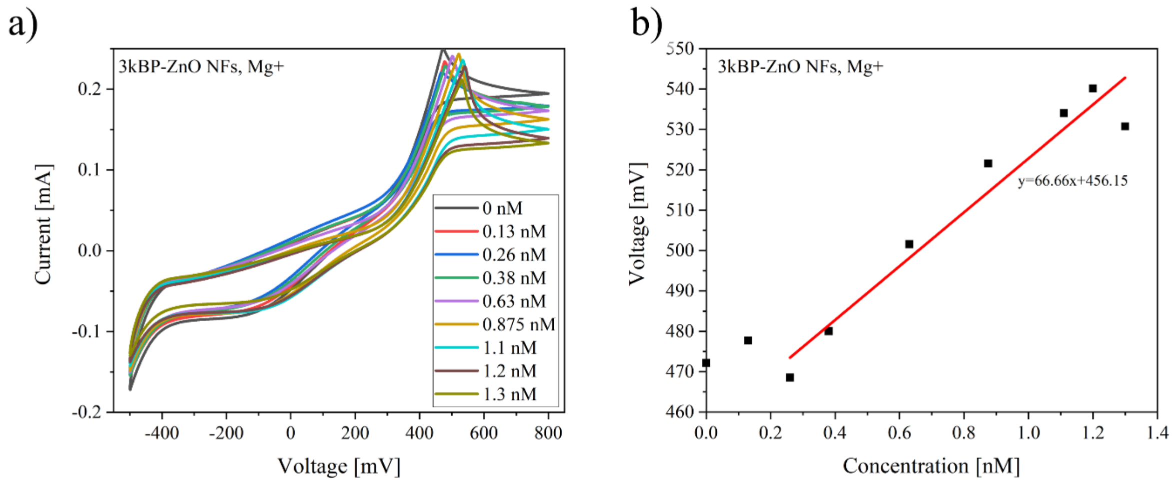

Fig. 4.42 a) Voltammograms for different concentrations of magnesium ions (0–1.3 nM) with the 3kBP-ZnO NFs used as the working electrode. b) Current peaks from voltammograms for different concentrations of $Mg^{2+}$with trendline.

Unlike for the measurement of zinc ions, here, with the increasing the Mg^{2+} ion concentration, the current did not decrease but the maximum current peak shifted to a higher potential (Fig. 4.42b). It happened because the magnesium ions reacted with the electrode surface. For lower concentrations, there is no dependence between the position of the peak and the concentration, but between 0.38 nM and 1.2 nM, there is an almost linear fitting (red line in Fig. 4.42b). The sensitivity of the sensor for that range is 67 mV/nM and the LoD is 0.05 nM.

Table 4.6 Range and limit of detection of magnesium ions for different method.

Magnesium ions detection				
Material	**Range of detection**	**Limit of detection**	**Method**	**REF**
3kBP-ZnO NFs	0.38 – 1.2 nM	0.05 nM	CV EC	This work
Methyl Phenyl Semicarbazone	10 nM – 0.1 M	1.7 nM	Ion-selective electrode - EC	[187]
4,5-Bis(Benzoylthio)-1,3-Dithiole-2- Thione	10 µM- 0.1 M	10 µM	Ion-selective electrode - EC	[188]
5,10,15,20-tetrakis(2-furyl)-21, 23-dithiaporphyrin	9.2 µM – 0.1 M	8 µM	potential	[189]
ZnO nanorod	500 nM – 100 mM	—	EC	[190]
Multi-Walled Carbon Nanotubes	1 ppm	—	EC impendance measurement	[143]

Most of the sensors are tested in a larger range than presented in this work, so their LoDs are also larger than the calculated value for the 3kBP-ZnO NFs electrode [187]–[190] (Table 4.6) Chandra et al. built a sensor based on methyl phenyl semicarbazone. Its LoD was estimated to be 1.2 nM, which is still higher than for the sensor presented in this dissertation, and its sensitivity was 28.4 mV/per decade [187].

To summarise, the electrochemical sensor with an electrode based on ZnO was built. How the addition of b-AsP and BP affected the electrode's sensitivity to Zn^{2+} was tested. The ZnO NFs, b-AsP-ZnO NFs and 3kBP-ZnO NFs are compared in Table 4.7.

Table 4.7 Comparison of properties for ZnO NFs electrodes without and with BP or b-AsP.

Electrode	**Stability**	**Limit of detection (Zn^{2+})**	**Reusability**
ZnO NFs	—	0.08 nM*	Yes (after cleaning)
b-AsP-ZnO NFs	+	0.016 nM*	No
3kBP-ZnO NFs	++	0.05 nM/0.6 nM**	Yes

* lowest measured value
** calculated value from formula LoD = $3.3 \cdot (\sigma/S)$

For the pristine ZnO NFs electrode, the lowest measured ion concentration was 0.08 nM. This value is notably lower than that of the sensors already known [183]–[186]. However, the ZnO NFs reacted only to the presence of Zn^{2+} ions but changing the concentration of ions did not cause further changes in the signal. After mixing b-AsP with ZnO NFs, the stability of the electrode improved. The signal decreased with increasing Zn^{2+} concentrations. The dependence between the ion concentration and the current was not linear, so the LoD could not be calculated, but the smallest measured value was 0.016 nM of Zn^{2+} ions. Unlike the ZnO NFs electrode, which could be reused after washing, the b-AsP-ZnO NFs electrode is disposable.

Adding BP to ZnO NFs improved the electrode's stability even more than b-AsP (hypothesis III**)**. A linear relationship between Zn^{2+} concentrations and the current peak was found, making it possible to calculate the LoD, which was 0.05 nM for ion concentrations below 0.47 nM and 0.6 nM for concentrations above 0.47 nM. These values are smaller than in previous works [183]–[186]. Moreover, compared to the b-AsP-ZnO NFs electrode, 3kBP-ZnO NFs can be used several times. This proves that BP can be used as an EC sensor to detect Zn^{2+} and Mg^{2+}.

Chapter 5. Conclusions

Few-layer black phosphorus (FLBP) shows a versatile bandgap that can be finely adjusted across a broad spectrum, ranging from 0.3 to 2 eV. This characteristic is complemented by its unique structural properties, primarily its pronounced anisotropy, which holds promise for applications in optics and optoelectronics. Phosphorene inherently exhibits optical anisotropy due to its crystalline arrangement. When linearly polarised light traverses a phosphorene flake, it becomes elliptically polarised. However, the most prominent polarisation effects manifest in single or few-layer phosphorus films. It is worth noting that the choice of exfoliation method can influence the resulting material's properties. A single flake may exhibit slightly different characteristics compared to a layer comprising multiple flakes oriented in various directions. Therefore, the selection of the exfoliation method should be tailored to the intended application of the resulting material.

In summary, the bandgap of black phosphorus (BP) is contingent on the number of layers, thereby impacting its optical and electrical attributes. Techniques such as UV-VIS spectrometry, Raman spectrometry, and photoluminescence can be employed to investigate the optical properties of BP and indirectly gauge the thickness of the thin film under scrutiny. However, investigations targeting the determination of BP's optical constants, including the refractive index and extinction coefficient, remain relatively scarce. This scarcity is especially pronounced when studying composite layers comprising multiple BP flakes with varying orientations. One notable drawback of FLBP lies in its susceptibility to rapid degradation in both air and water environments. PxOy compounds were observed on the FLBP surface shortly after exposure to air.

The oxidation process of FLBP commences immediately upon contact with air, substantially affecting its properties. This degradation process can be monitored through various means, including Raman spectroscopy and absorbance measurements. Nevertheless, the rapid degradation may restrict the range of applications for FLBP. Section 1.3 outlines techniques for preserving FLBP. As elucidated in Chapter 2, FLBP exhibits intriguing optoelectronic and optical characteristics, rendering it suitable for a diverse array of applications. However, comprehensive knowledge of its refractive index and extinction coefficient is imperative. BP distinguishes itself with commendable carrier mobility and an on/off ratio, setting it apart from other two-dimensional materials. Moreover, its bandgap's wide tunability further enhances its versatility. FLBP's anisotropic crystal structure profoundly influences its interaction with light, rendering it highly birefringent and dichroic. These exceptional properties position FLBP as a valuable asset across numerous applications. Its reactivity to factors such as humidity, DNA, NO_2, and metal ions makes it particularly suitable for sensor applications.

FLBP's distinctive crystal structure underpins its pronounced birefringence and dichroism. It has been demonstrated that BP's optical anisotropy surpasses that of other two-dimensional materials; however, this anisotropy tends to diminish as the BP layer thickness increases. This optical dichroism also holds potential for mapping and monitoring BP's degradation and decomposition processes.

The primary objective of this thesis is to develop specialised methods and tools for investigating the optical parameters of FLBP, with a particular focus on their relevance to sensing applications. The research involves the study of FLBP layers and suspensions through polarisation microscopy, spectroscopy, and ellipsometry, complemented by electrochemical techniques. These methodologies aim not only to uncover the causes of degradation in FLBP but also to assess the extent of this degradation and evaluate its sensory capabilities. The utilisation of FLBP structures has paved the way for the creation of a new class of optical sensors designed to detect toxic compounds, including heavy metals.

Various exfoliation methods, such as mechanical, liquid, and electrochemical methods, were used to prepare FLBP. The exfoliation method affects the characteristics of the prepared layer, as shown in Chapter 4.1, so it must be carefully selected depending on the application. How certain parameters are affected by a pristine FLBP layer, a b-AsP alloy, and a composite layer of FLBP and ZnO was also compared.

Spectroscopic ellipsometry was applied as an optimal technique used for determining the optical constants and thickness of thin materials. Section 4.2 highlights how SE can also be applied for the analysis of FLBP layers. FLBP was prepared using the liquid exfoliation process, where various centrifugation speeds were employed to obtain layers of varying thicknesses. The SE measurement yielded the Δ and Ψ angles, which indicate that the layer thickness decreases with increased centrifugation speed. The presence of defects in the layer is also visible. After the further analysis, the average values for thickness, refractive index, and extinction coefficient were calculated for the whole BP layer. These results align with previous studies of phosphorene and FLBP that used different measurement techniques (hypothesis 1). This indicates that the chosen parameters of both the deagglomeration and centrifugation processes have produced an FLBP layer whose optical properties closely resemble the values for the 2D layer.

As was mentioned, FLBP is characterised by an anisotropic structure, which makes it optically birefringent and dichroic. Liquid and mechanically exfoliated FLBP layers were observed through a polarised-light microscope, which was described in Section 4.3.1. Changes in the intensity as a function of rotation were observed when viewed through crossed polarisers. The study also investigated the time-dependent changes in the signal when FLBP is exposed to air. The intensity varied with the thickness of the sample during the oxidation process, which makes it possible to determine the oxidation kinetics of the FLBP layer (hypothesis 2). A periodic pattern was consistently visible, indicating the anisotropy of BP. After 30 days, a slight deviation was observed in the angle of maximum intensity, which can be identified with the AC crystalline direction of the BP. This deviation may have been influenced by the acid and oxide layers, as well as the degradation of the first BP layers and the exposure of flakes below it, characterised by a slight shift in the orientation of their crystal lattice.

As noted in Chapter 4, FLBP can be used as a sensor. In this dissertation, whether it is possible to build a PL sensor based on FLBP for metal ion detection was examined. For this purpose, electrochemically exfoliated FLBP, as well as CVT-fabricated b-AsP nanoribbons, were used. Both materials were mixed with ZnO NRs, resulting in a PL response in the visible and NIR range. Next, how the prepared samples deposited on a Si substrate responded to the presence of Zn^{2+} and Mg^{2+} ions were checked, as described in Section 4.4.1. BP responded to the presence of ions even in very low concentrations (1 pM of Zn^{2+}), but the ions modified the sample's surface. Subsequent changes in concentration, or switching pristine water versus water with metal ions, did not result in further changes. B-AsP proved to be much more stable. It responded to any change in the concentration of Zn^{2+} and Mg^{2+} ions. The signal change from the sensor was always consistent, regardless of the ion concentration. Therefore, the sensor can only detect the presence of ions, however even at very low concentrations (hypothesis 3).

The capability of detecting Zn^{2+} ions using an EC sensor that based on ZnO NFs modified by BP and b-AsP was also tested. These results show that the signal varies with the ion concentration when the b-AsP-ZnO NFs is used as the working electrode (hypothesis 3), in contrast to the pristine ZnO NFs electrode, which responded solely to the initial concentration. Moreover, the sensor could identify ions with concentrations as low as 0.016 nM, a value notably lower than the previously known sensors. Regrettably, the b-AsP-based sensor is disposable. The BP-based sensor is considerably more stable. The signal changed with the change in concentration of ions, and a direct correlation was determined, leading to the calculation of the LoD, which was 0.05 nM for concentrations below 0.47 nM of Zn^{2+} and 0.6 nM for higher concentrations, which is less than most previously known sensors, as was shown in Section 4.4.2. The sensor can also be reused multiple times. This summary demonstrates the potential of BP as a sensor for detecting metal ions, specifically Zn^{2+} (hypothesis 3).

Finally, it has been shown that FLBP can be used as an optical and sensor material. Furthermore, the study indicates that variations in spinning parameters during FLBP layer preparation influence its optical properties. Despite experiencing oxidation in air, FLBP retains its anisotropic characteristics over an extended period, thereby showing promise for use in polarisation applications. FLBP also reacts to metal ions, particularly Zn^{2+}, making it possible to develop PL and EC sensors based on FLBP. The detection of metal ions is also possible with the b-AsP alloy, although its sensitivity and stability vary from those achieved with pristine FLBP. These findings confirm all three formulated hypotheses.

The development of FLBP-based sensors for detecting metal ions, particularly Zn^{2+}, is a noteworthy achievement. In the future, researchers can expand the scope of detectable ions and further enhance the sensitivity. The contrasting characteristics of BP-based and b-AsP-based sensors offer intriguing possibilities. BP-based sensors cannot be reused, while b-AsP-based sensors exhibit superior stability. Combining these attributes in hybrid sensor designs could yield versatile solutions for various applications. FLBP’s optical properties and long-term stability make it a valuable material for polarisation applications. We can explore ways to precisely control these properties, potentially leading to advanced optical devices. The integration of both photoluminescence (PL) and electrochemical (EC) sensors based on FLBP creates versatile multi-sensor platforms. These platforms have the potential to simultaneously detect multiple analytes, broadening their utility across various fields. To realise the full potential of FLBP-based sensors, the transition from laboratory research to practical applications is crucial. Collaboration with industry and regulatory bodies will be necessary to bridge the gap and deploy these sensors in real-world scenarios. Finally, FLBP research has paved the way for advancements in sensing technology with diverse applications. Ongoing research will refine these sensors, ultimately providing practical solutions to real-world challenges.

References

[1] K. Myny, “The development of flexible integrated circuits based on thin-film transistors,” *Nat. Electron.*, vol. 1, no. 1, pp. 30–39, 2018, doi: 10.1038/s41928-017-0008-6.

[2] M. Y. Li, S. K. Su, H. S. P. Wong, and L. J. Li, “How 2D semiconductors could extend Moore’s law,” *Nature*, vol. 567, no. 7747. Nature Publishing Group, pp. 169–170, Mar. 12, 2019, doi: 10.1038/d41586-019-00793-8.

[3] “Top Advanced Materials & Technologies in the Electronics Industry.” https://blog.marketresearch.com/the-top-advanced-materials-technologies-in-the-electronics-industry (accessed Feb. 02, 2023).

[4] K. S. Novoselov *et al.*, “Electric field in atomically thin carbon films,” *Science (80-.).*, vol. 306, no. 5696, pp. 666–669, Oct. 2004, doi: 10.1126/science.1102896.

[5] S. Manzeli, D. Ovchinnikov, D. Pasquier, O. V. Yazyev, and A. Kis, “2D transition metal dichalcogenides,” *Nat. Rev. Mater.*, vol. 2, 2017, doi: 10.1038/natrevmats.2017.33.

[6] J. A. Kumar *et al.*, “Methods of synthesis, characteristics, and environmental applications of MXene: A comprehensive review,” *Chemosphere*, vol. 286, no. P1, p. 131607, 2022, doi: 10.1016/j.chemosphere.2021.131607.

[7] H. Liu *et al.*, “Phosphorene: An unexplored 2D semiconductor with a high hole mobility,” *ACS Nano*, vol. 8, no. 4, pp. 4033–4041, Apr. 2014, doi: 10.1021/nn501226z.

[8] J. Qiao, X. Kong, Z. X. Hu, F. Yang, and W. Ji, “High-mobility transport anisotropy and linear dichroism in few-layer black phosphorus,” *Nat. Commun.*, vol. 5, no. 1, pp. 1–7, Jul. 2014, doi: 10.1038/ncomms5475.

[9] F. Schedin *et al.*, “Detection of individual gas molecules adsorbed on graphene,” *Nat. Mater.*, vol. 6, no. 9, pp. 652–655, 2007, doi: 10.1038/nmat1967.

[10] C. Liu *et al.*, “Black phosphorus integrated tilted fiber grating for ultrasensitive heavy metal sensing,” *Sensors Actuators, B Chem.*, vol. 257, pp. 1093–1098, Mar. 2018, doi: 10.1016/j.snb.2017.11.022.

[11] M. Grundmann, *Two-Dimensional Semiconductors*. Wiley-VCH Verlag, 2021.

[12] J. R. Brent, N. Savjani, E. A. Lewis, S. J. Haigh, D. J. Lewis, and P. O’Brien, “Production of few-layer phosphorene by liquid exfoliation of black phosphorus,” *Chem. Commun.*, vol. 50, no. 87, pp. 13338–13341, Oct. 2014, doi: 10.1039/c4cc05752j.

[13] Z. Cai, B. Liu, X. Zou, and H. M. Cheng, “Chemical Vapor Deposition Growth and Applications of Two-Dimensional Materials and Their Heterostructures,” *Chem. Rev.*, vol. 118, no. 13, pp. 6091–6133, Jul. 2018, doi: 10.1021/ACS.CHEMREV.7B00536.

[14] J. Yu, J. Li, W. Zhang, and H. Chang, “Synthesis of high quality two-dimensional materials via chemical vapor deposition,” *Chem. Sci.*, vol. 6, no. 12, pp. 6705–6716, Nov. 2015, doi: 10.1039/c5sc01941a.

[15] A. H. Castro Neto, F. Guinea, N. M. R. Peres, K. S. Novoselov, and A. K. Geim, “The electronic properties of graphene,” *Rev. Mod. Phys.*, vol. 81, no. 1, pp. 109–162, 2009, doi: 10.1103/RevModPhys.81.109.

[16] V. M. Pereira, A. H. Castro Neto, and N. M. R. Peres, “Tight-binding approach to uniaxial strain in graphene,” doi: 10.1103/PhysRevB.80.045401.

[17] P. Rani and V. K. Jindal, “Designing band gap of graphene by B and N dopant atoms,” *RSC Adv.*, vol. 3, no. 3, pp. 802–812, Dec. 2013, doi: 10.1039/c2ra22664b.

[18] Y. Zhang, Y. W. Tan, H. L. Stormer, and P. Kim, “Experimental observation of the quantum Hall effect and Berry’s phase in graphene,” *Nature*, vol. 438, no. 7065, pp. 201–204, Nov. 2005, doi: 10.1038/nature04235.

[19] K. S. Novoselov *et al.*, “Two-dimensional gas of massless Dirac fermions in graphene,” *Nature*, vol. 438, no. 7065, pp. 197–200, Nov. 2005, doi: 10.1038/nature04233.

[20] L. Yang, J. Deslippe, C. H. Park, M. L. Cohen, and S. G. Louie, “Excitonic Effects on the Optical Response of Graphene and Bilayer Graphene,” *Phys. Rev. Lett.*, vol. 103, no. 18, pp. 1–4, 2009, doi: 10.1103/PhysRevLett.103.186802.

[21] G. Pirruccio, L. Martín Moreno, G. Lozano, and J. Gómez Rivas, “Coherent and broadband enhanced optical absorption in graphene,” *ACS Nano*, vol. 7, no. 6, pp. 4810–4817, 2013, doi: 10.1021/nn4012253.

[22] A. Kumar, G. Sachdeva, R. Pandey, and S. P. Karna, “Optical absorbance in multilayer two-dimensional materials: Graphene and antimonene,” *Appl. Phys. Lett.*, vol. 116, no. 26, p. 263102, Jun. 2020, doi: 10.1063/5.0010794.

[23] F. Wang *et al.*, “Gate-variable optical transitions in graphene,” *Science (80-.).*, vol. 320, no. 5873, pp. 206–209, Apr. 2008, doi: 10.1126/science.1152793.

[24] X. Zhang *et al.*, “In-plane anisotropy in twisted bilayer graphene probed by Raman spectroscopy,” *Nanotechnology*, vol. 30, no. 43, 2019, doi: 10.1088/1361-6528/ab33e0.

[25] A. H. Castro Neto and F. Guinea, “Electron-phonon coupling and Raman spectroscopy in graphene,” *Phys. Rev. B - Condens. Matter Mater. Phys.*, vol. 75, no. 4, 2007, doi: 10.1103/PhysRevB.75.045404.

[26] L. Liu, M. Qing, Y. Wang, and S. Chen, “Defects in Graphene: Generation, Healing, and Their Effects on the Properties of Graphene: A Review,” *J. Mater. Sci. Technol.*, vol. 31, no. 6, pp. 599–606, 2015, doi: 10.1016/j.jmst.2014.11.019.

[27] T. Xu and L. Sun, “Structural defects in graphene,” in *Defects in Advanced Electronic Materials and Novel Low Dimensional Structures*, vol. 5, no. 1, 2018, pp. 137–160.

[28] P. O. Lehtinen, A. S. Foster, A. Ayuela, A. Krasheninnikov, K. Nordlund, and R. M. Nieminen, “Magnetic Properties and Diffusion of Adatoms on a Graphene Sheet,” *Phys. Rev. Lett.*, vol. 91, no. 1, pp. 1–4, 2003, doi: 10.1103/PhysRevLett.91.017202.

[29] P. Koskinen, S. Malola, and H. Häkkinen, “Self-passivating edge reconstructions of graphene,” *Phys. Rev. Lett.*, vol. 101, no. 11, pp. 1–4, 2008, doi: 10.1103/PhysRevLett.101.115502.

[30] L. Tapasztó, G. Dobrik, P. Nemes-Incze, G. Vertesy, P. Lambin, and L. P. Biró, “Tuning the electronic structure of graphene by ion irradiation,” *Phys. Rev. B*, vol. 78, no. 23, pp. 1–4, 2008, doi: 10.1103/physrevb.78.233407.

[31] R. Wang *et al.*, “Strategies on Phase Control in Transition Metal Dichalcogenides,” *Adv. Funct. Mater.*, vol. 28, no. 47, 2018, doi: 10.1002/adfm.201802473.

[32] J. Li, Z. Wei, and J. Kang, *Two-dimensional semiconductors: Synthesis, physical properties and applications*. wiley, 2020.

[33] A. Splendiani *et al.*, “Emerging photoluminescence in monolayer MoS2,” *Nano Lett.*, vol. 10, no. 4, pp. 1271–1275, 2010, doi: 10.1021/nl903868w.

[34] R. Frisenda *et al.*, “Biaxial strain tuning of the optical properties of single-layer transition metal dichalcogenides,” *npj 2D Mater. Appl.*, vol. 1, no. 1, pp. 1–7, May 2017, doi: 10.1038/s41699-017-0013-7.

[35] Y. Gong *et al.*, “Band Gap Engineering and Layer-by-Layer Mapping of Selenium-Doped Molybdenum Disulfide,” *Nano Lett*, vol. 14, 2014, doi: 10.1021/nl4032296.

[36] B. Radisavljevic, A. Radenovic, J. Brivio, V. Giacometti, and A. Kis, “Single-layer MoS2 transistors,” *Nat. Nanotechnol.*, vol. 6, no. 3, pp. 147–150, 2011, doi: 10.1038/nnano.2010.279.

[37] M. M. Bernal *et al.*, “Luminescent transition metal dichalcogenide nanosheets through one-step liquid phase exfoliation,” *2D Mater.*, vol. 3, no. 3, p. 035014, Sep. 2016, doi: 10.1088/2053-1583/3/3/035014.

[38] N. Ansari, E. Mohebbi, and F. Gholami, “Nearly perfect and broadband optical absorption by TMDCs in cover/TMDC/spacer/Au/substrate multilayers,” *Appl. Phys. B Lasers Opt.*, vol. 126, no. 1, pp. 1–6, Jan. 2020, doi: 10.1007/s00340-019-7352-3.

[39] M. A. Khan, M. Erementchouk, J. Hendrickson, and M. N. Leuenberger, “Electronic and optical properties of vacancy defects in single-layer transition metal dichalcogenides,” *Phys. Rev. B*, vol. 95, no. 24, pp. 1–12, 2017, doi: 10.1103/PhysRevB.95.245435.

[40] K. He *et al.*, “Tightly bound excitons in monolayer WSe2,” *Phys. Rev. Lett.*, vol. 113, no. 2, pp. 1–5, 2014, doi: 10.1103/PhysRevLett.113.026803.

[41] C. Zhang, A. Johnson, C. L. Hsu, L. J. Li, and C. K. Shih, “Direct imaging of band profile in single layer MoS2 on graphite: Quasiparticle energy gap, metallic edge states, and edge band bending,” *Nano Lett.*, vol. 14, no. 5, pp. 2443–2447, 2014, doi: 10.1021/nl501133c.

[42] H. P. Komsa and A. V. Krasheninnikov, “Effects of confinement and environment on the electronic structure and exciton binding energy of MoS2 from first principles,” *Phys. Rev. B - Condens. Matter Mater. Phys.*, vol. 86, no. 24, pp. 1–6, 2012, doi: 10.1103/PhysRevB.86.241201.

[43] A. R. Klots *et al.*, “Probing excitonic states in suspended two-dimensional semiconductors by photocurrent spectroscopy,” *Sci. Reports 2014 41*, vol. 4, no. 1, pp. 1–7, Oct. 2014, doi: 10.1038/srep06608.

[44] O. B. Aslan, D. A. Chenet, A. M. Van Der Zande, J. C. Hone, and T. F. Heinz, “Linearly Polarized Excitons in Single- and Few-Layer ReS2 Crystals,” *ACS Photonics*, vol. 3, no. 1, pp. 96–101, 2016, doi: 10.1021/acsphotonics.5b00486.

[45] A. M. Shafi *et al.*, “Inducing Strong Light-Matter Coupling and Optical Anisotropy in Monolayer MoS2with High Refractive Index Nanowire,” *ACS Appl. Mater. Interfaces*, vol. 14, no. 27, pp. 31140–31147, 2022, doi: 10.1021/acsami.2c07705.

[46] Q. Zhang, A. T. S. Wee, Q. Liang, X. Zhao, and M. Liu, “Defect engineering of two-dimensional transition-metal dichalcogenides: Applications, challenges, and

opportunities," *ACS Nano*, vol. 15, no. 2. pp. 2165–2181, 2021, doi: 10.1021/acsnano.0c09666.

[47] Z. Lin *et al.*, "Defect engineering of two-dimensional transition metal dichalcogenides," *2D Materials*, vol. 3, no. 2. IOP Publishing, p. 022002, Apr. 13, 2016, doi: 10.1088/2053-1583/3/2/022002.

[48] A. N. Enyashin, M. Bar-Sadan, L. Houben, and G. Seifert, "Line Defects in Molybdenum Disulfide Layers," 2013, doi: 10.1021/jp403976d.

[49] A. M. Van Der Zande *et al.*, "Grains and grain boundaries in highly crystalline monolayer molybdenum disulphide," *Nat. Mater.*, vol. 12, no. 6, pp. 554–561, 2013, doi: 10.1038/nmat3633.

[50] L. Li *et al.*, "Direct observation of the layer-dependent electronic structure in phosphorene," *Nat. Nanotechnol.*, vol. 12, no. 1, pp. 21–25, 2017, doi: 10.1038/nnano.2016.171.

[51] A. Castellanos-Gomez *et al.*, "Isolation and characterization of few-layer black phosphorus," *2D Mater.*, vol. 1, no. 2, p. 025001, Sep. 2014, doi: 10.1088/2053-1583/1/2/025001.

[52] V. Tran, R. Soklaski, Y. Liang, and L. Yang, "Layer-controlled band gap and anisotropic excitons in few-layer black phosphorus," *Phys. Rev. B - Condens. Matter Mater. Phys.*, vol. 89, no. 23, p. 235319, 2014, doi: 10.1103/PhysRevB.89.235319.

[53] J. Miao, L. Cai, S. Zhang, J. Nah, J. Yeom, and C. Wang, "Air-Stable Humidity Sensor Using Few-Layer Black Phosphorus," *ACS Appl. Mater. Interfaces*, vol. 9, no. 11, pp. 10019–10026, Mar. 2017, doi: 10.1021/acsami.7b01833.

[54] X. Wang, Y. P. Chen, and D. D. Nolte, "Strong anomalous optical dispersion of graphene: complex refractive index measured by Picometrology," *Opt. Express*, vol. 16, no. 26, p. 22105, 2008, doi: 10.1364/oe.16.022105.

[55] X. Wang and S. Lan, "Optical properties of black phosphorus," *Adv. Opt. Photonics*, vol. 8, no. 4, p. 618, 2016, doi: 10.1364/aop.8.000618.

[56] T. Low *et al.*, "Tunable optical properties of multilayer black phosphorus thin films," *Phys. Rev. B - Condens. Matter Mater. Phys.*, vol. 90, no. 7, p. 75434, Aug. 2014, doi: 10.1103/PhysRevB.90.075434.

[57] J. D. Wood *et al.*, "Effective passivation of exfoliated black phosphorus transistors against ambient degradation," *Nano Lett.*, vol. 14, no. 12, pp. 6964–6970, 2014, doi: 10.1021/nl5032293.

[58] X. Ling, H. Wang, S. Huang, F. Xia, and M. S. Dresselhaus, "The renaissance of black phosphorus," *Proceedings of the National Academy of Sciences of the United States of America*, vol. 112, no. 15. National Academy of Sciences, pp. 4523–4530, Apr. 14, 2015, doi: 10.1073/pnas.1416581112.

[59] G. Wang, W. J. Slough, R. Pandey, and S. P. Karna, "Degradation of phosphorene in air: Understanding at atomic level," *2D Mater.*, vol. 3, no. 2, pp. 1–7, 2016, doi: 10.1088/2053-1583/3/2/025011.

[60] A. Favron *et al.*, "Photooxidation and quantum confinement effects in exfoliated black phosphorus," *Nat. Mater.*, vol. 14, no. 8, pp. 826–832, 2015, doi: 10.1038/nmat4299.

[61] D. K. Sang, H. Wang, Z. Guo, N. Xie, and H. Zhang, “Recent Developments in Stability and Passivation Techniques of Phosphorene toward Next-Generation Device Applications,” *Adv. Funct. Mater.*, vol. 29, no. 45, pp. 1–22, 2019, doi: 10.1002/adfm.201903419.

[62] J. Sun, N. Lin, H. Ren, C. Tang, L. Yang, and X. Zhao, “The electronic structure, mechanical flexibility and carrier mobility of black arsenic-phosphorus monolayers: A first principles study,” *Phys. Chem. Chem. Phys.*, vol. 18, no. 14, pp. 9779–9787, Mar. 2016, doi: 10.1039/c6cp00047a.

[63] S. Yang, J. Peng, H. Huang, Z. Li, H. Dong, and F. Wu, “The tunable bandgap of phosphorus-arsenic alloys for mid-and long-infrared regime photodetectors,” *Mater. Sci. Semicond. Process.*, vol. 144, 2022, doi: 10.1016/j.mssp.2022.106552.

[64] M. Long *et al.*, “Room temperature high-detectivity mid-infrared photodetectors based on black arsenic phosphorus,” *Sci. Adv.*, vol. 3, no. 6, Jun. 2017, doi: 10.1126/sciadv.1700589.

[65] B. Liu *et al.*, “Black Arsenic-Phosphorus: Layered Anisotropic Infrared Semiconductors with Highly Tunable Compositions and Properties,” *Adv. Mater.*, vol. 27, no. 30, pp. 4423–4429, 2015, doi: 10.1002/adma.201501758.

[66] H. Fang, S. Chuang, T. C. Chang, K. Takei, T. Takahashi, and A. Javey, “High-performance single layered WSe 2 p-FETs with chemically doped contacts,” *Nano Lett.*, vol. 12, no. 7, pp. 3788–3792, 2012, doi: 10.1021/nl301702r.

[67] L. Li *et al.*, “Black phosphorus field-effect transistors,” *Nat. Nanotechnol.*, vol. 9, no. 5, pp. 372–377, 2014, doi: 10.1038/nnano.2014.35.

[68] J. Lin, H. Li, H. Zhang, and W. Chen, “Plasmonic enhancement of photocurrent in MoS2 field-effect-transistor,” *Appl. Phys. Lett.*, vol. 102, no. 20, p. 203109, May 2013, doi: 10.1063/1.4807658.

[69] Z. Cheng, T. Zhao, and H. Zeng, “2D Material-Based Photodetectors for Infrared Imaging,” *Small Sci.*, vol. 2, no. 1, p. 2100051, Jan. 2022, doi: 10.1002/SMSC.202100051.

[70] O. Lopez-Sanchez, D. Lembke, M. Kayci, A. Radenovic, and A. Kis, “Ultrasensitive photodetectors based on monolayer MoS 2,” *Nat. Nanotechnol.*, vol. 8, no. 7, pp. 497–501, 2013, doi: 10.1038/nnano.2013.100.

[71] J. Miao *et al.*, “High-responsivity graphene/InAs nanowire heterojunction near-infrared photodetectors with distinct photocurrent on/off ratios,” *Small*, vol. 11, no. 8, pp. 936–942, Feb. 2015, doi: 10.1002/smll.201402312.

[72] P. Zhang, F. Wang, M. Yu, X. Zhuang, and X. Feng, “Two-dimensional materials for miniaturized energy storage devices: from individual devices to smart integrated systems,” *Chemical Society Reviews*, vol. 47, no. 19. Royal Society of Chemistry, pp. 7426–7451, Oct. 01, 2018, doi: 10.1039/c8cs00561c.

[73] M. A. Bissett, S. D. Worrall, I. A. Kinloch, and R. A. W. Dryfe, “Comparison of Two-Dimensional Transition Metal Dichalcogenides for Electrochemical Supercapacitors,” *Electrochim. Acta*, vol. 201, pp. 30–37, May 2016, doi: 10.1016/j.electacta.2016.03.190.

[74] Y. Chen *et al.*, “In-situ selective surface engineering of graphene micro-supercapacitor chips,” *Nano Res.*, vol. 15, no. 2, pp. 1492–1499, Aug. 2022, doi: 10.1007/s12274-021-

3693-4.

[75] H. Lin *et al.*, “Diffraction-limited imaging with monolayer 2D material-based ultrathin flat lenses,” *Light Sci. Appl.*, vol. 9, no. 1, pp. 2047–7538, 2020, doi: 10.1038/s41377-020-00374-9.

[76] S. Y. Lee and K. J. Yee, “Black phosphorus phase retarder based on anisotropic refractive index dispersion,” *2D Mater.*, vol. 9, no. 1, p. 015020, Nov. 2022, doi: 10.1088/2053-1583/ac3a99.

[77] Y. Fang, Y. Ge, C. Wang, and H. Zhang, “Mid-Infrared Photonics Using 2D Materials: Status and Challenges,” *Laser Photonics Rev.*, vol. 14, no. 1, pp. 1–31, 2020, doi: 10.1002/lpor.201900098.

[78] Q. Bao *et al.*, “Atomic-layer craphene as a saturable absorber for ultrafast pulsed lasers,” *Adv. Funct. Mater.*, vol. 19, no. 19, pp. 3077–3083, 2009, doi: 10.1002/adfm.200901007.

[79] J. Sotor, G. Sobon, M. Kowalczyk, W. Macherzynski, P. Paletko, and K. M. Abramski, “Ultrafast thulium-doped fiber laser mode locked with black phosphorus,” 2015, doi: 10.1364/OL.40.003885.

[80] C. Lin, R. Grassi, T. Low, and A. S. Helmy, “Multilayer Black Phosphorus as a Versatile Mid-Infrared Electro-optic Material,” *Nano Lett.*, vol. 16, no. 3, pp. 1683–1689, Mar. 2016, doi: 10.1021/acs.nanolett.5b04594.

[81] M. Pumera, “Phosphorene and black phosphorus for sensing and biosensing,” *TrAC - Trends in Analytical Chemistry*, vol. 93. pp. 1–6, 2017, doi: 10.1016/j.trac.2017.05.002.

[82] W. Gu *et al.*, “Black Phosphorus Quantum Dots as the Ratiometric Fluorescence Probe for Trace Mercury Ion Detection Based on Inner Filter Effect,” *ACS Sensors*, vol. 2, no. 4, pp. 576–582, Apr. 2017, doi: 10.1021/acssensors.7b00102.

[83] M. Israr-Qadir, S. Jamil-Rana, O. Nur, and M. Willander, “Zinc Oxide-Based Self-Powered potentiometric chemical sensors for biomolecules and metal ions,” *Sensors (Switzerland)*, vol. 17, no. 7, 2017, doi: 10.3390/s17071645.

[84] C. Wang, W. Li, M. Guo, and J. Ji, “Ecological risk assessment on heavy metals in soils: Use of soil diffuse reflectance mid-infrared Fourier-transform spectroscopy,” *Sci. Rep.*, vol. 7, no. 1, pp. 1–11, Feb. 2017, doi: 10.1038/srep40709.

[85] H. Geiger and C. Wanner, “Magnesium in disease,” *CKJ: Clinical Kidney Journal*, vol. 5, no. SUPPL. 1. pp. 25–38, 2012, doi: 10.1093/ndtplus/sfr165.

[86] V. Fedorenko *et al.*, “Application of polydopamine functionalized zinc oxide for glucose biosensor design,” *Polymers (Basel).*, vol. 13, no. 17, p. 2918, Aug. 2021, doi: 10.3390/polym13172918.

[87] Y. Huang, X. Dong, Y. Shi, C. M. Li, L. J. Li, and P. Chen, “Nanoelectronic biosensors based on CVD grown graphene,” *Nanoscale*, vol. 2, no. 8, pp. 1485–1488, Aug. 2010, doi: 10.1039/c0nr00142b.

[88] Y. T. Yew, Z. Sofer, C. C. Mayorga-Martinez, and M. Pumera, “Black phosphorus nanoparticles as a novel fluorescent sensing platform for nucleic acid detection,” *Mater. Chem. Front.*, vol. 1, no. 6, pp. 1130–1136, 2017, doi: 10.1039/c6qm00341a.

[89] D. E. C. Corbridge, *Phosphorus: Chemistry, Biochemistry and Technology, Sixth Edition (6th ed.)*, 6th ed. Boca Raton: CRC Press, 2016, 2016.

[90] P. W. Bridgman, “Two new modifications of phosphorus,” *J. Am. Chem. Soc.*, vol. 36, no. 7, pp. 1344–1363, 1914.

[91] J. Pei *et al.*, “Producing air-stable monolayers of phosphorene and their defect engineering,” *Nat. Commun.*, vol. 7, 2016, doi: 10.1038/ncomms10450.

[92] E. Kovalska *et al.*, “Non-aqueous solution-processed phosphorene by controlled low-potential electrochemical exfoliation and thin film preparation,” *Nanoscale*, vol. 12, no. 4, pp. 2638–2647, Jan. 2020, doi: 10.1039/c9nr10257d.

[93] A. Ambrosi, Z. Sofer, and M. Pumera, “Electrochemical Exfoliation of Layered Black Phosphorus into Phosphorene,” *Angew. Chemie - Int. Ed.*, vol. 56, no. 35, pp. 10443–10445, Aug. 2017, doi: 10.1002/anie.201705071.

[94] H. Huang *et al.*, “Rapid and scalable production of high-quality phosphorene by plasma-liquid technology,” *Chem. Commun.*, vol. 56, no. 2, pp. 221–224, Dec. 2019, doi: 10.1039/c9cc07640a.

[95] L. Sun *et al.*, “Chemical vapour deposition,” *Nat. Rev. Methods Prim. 2021 11*, vol. 1, no. 1, pp. 1–20, Jan. 2021, doi: 10.1038/s43586-020-00005-y.

[96] J. B. Smith, D. Hagaman, and H. F. Ji, “Growth of 2D black phosphorus film from chemical vapor deposition,” *Nanotechnology*, vol. 27, no. 21, pp. 1–8, 2016, doi: 10.1088/0957-4484/27/21/215602.

[97] Q. Jiang, J. Li, N. Yuan, Z. Wu, and J. Tang, “Black phosphorus with superior lithium ion batteries performance directly synthesized by the efficient thermal-vaporization method,” *Electrochim. Acta*, vol. 263, pp. 272–276, Feb. 2018, doi: 10.1016/J.ELECTACTA.2018.01.012.

[98] H. Yuan *et al.*, “Polarization-sensitive broadband photodetector using a black phosphorus vertical p-n junction,” *Nat. Nanotechnol.*, vol. 10, no. 8, pp. 707–713, 2015, doi: 10.1038/nnano.2015.112.

[99] J. Tao *et al.*, “Mechanical and Electrical Anisotropy of Few-Layer Black Phosphorus,” *ACS Nano*, vol. 9, no. 11, pp. 11362–11370, 2015, doi: 10.1021/acsnano.5b05151.

[100] Z. Guo *et al.*, “From Black Phosphorus to Phosphorene: Basic Solvent Exfoliation, Evolution of Raman Scattering, and Applications to Ultrafast Photonics,” *Adv. Funct. Mater.*, vol. 25, no. 45, pp. 6996–7002, Dec. 2015, doi: 10.1002/adfm.201502902.

[101] X. Zhang *et al.*, “Black phosphorus quantum dots,” *Angew. Chemie - Int. Ed.*, vol. 54, no. 12, pp. 3653–3657, Mar. 2015, doi: 10.1002/anie.201409400.

[102] Z. Sun *et al.*, “Ultrasmall Black Phosphorus Quantum Dots: Synthesis and Use as Photothermal Agents,” *Angew. Chemie - Int. Ed.*, vol. 54, no. 39, pp. 11526–11530, 2015, doi: 10.1002/anie.201506154.

[103] M. Akhtar *et al.*, “Bilayer phosphorene under high pressure: In situ Raman spectroscopy,” *Phys. Chem. Chem. Phys.*, vol. 21, no. 14, pp. 7298–7304, Apr. 2019, doi: 10.1039/c9cp00816k.

[104] S. Liu *et al.*, “Thickness-dependent Raman spectra, transport properties and infrared photoresponse of few-layer black phosphorus,” *J. Mater. Chem. C*, vol. 3, no. 42, pp. 10974–10980, 2015, doi: 10.1039/c5tc01809a.

[105] Y. Feng *et al.*, “Raman spectra of few-layer phosphorene studied from first-principles

calculations," *J. Phys. Condens. Matter*, vol. 27, no. 18, p. 185302, 2015, doi: 10.1088/0953-8984/27/18/185302.

[106] J. Yang *et al.*, "Optical tuning of exciton and trion emissions in monolayer phosphorene," *Light Sci. Appl.*, vol. 4, no. 7, pp. e312–e312, Jul. 2015, doi: 10.1038/lsa.2015.85.

[107] C. Chen *et al.*, "Bright Mid-Infrared Photoluminescence from Thin-Film Black Phosphorus," *Nano Lett.*, vol. 19, no. 3, pp. 1488–1493, 2019, doi: 10.1021/acs.nanolett.8b04041.

[108] R. Tian *et al.*, "Observation of excitonic series in monolayer and few-layer black phosphorus," *Phys. Rev. B*, vol. 101, no. 23, p. 235407, 2020, doi: 10.1103/PhysRevB.101.235407.

[109] S. Yoon *et al.*, "Electrical control of anisotropic and tightly bound excitons in bilayer phosphorene," *Phys. Rev. B*, vol. 103, no. 4, p. 41407, 2021, doi: 10.1103/PhysRevB.103.L041407.

[110] D. Y. Qiu, F. H. Da Jornada, and S. G. Louie, "Environmental Screening Effects in 2D Materials: Renormalization of the Bandgap, Electronic Structure, and Optical Spectra of Few-Layer Black Phosphorus," *Nano Lett.*, vol. 17, no. 8, pp. 4706–4712, 2017, doi: 10.1021/acs.nanolett.7b01365.

[111] J. Plutnar, Z. Sofer, and M. Pumera, "Products of degradation of black phosphorus in protic solvents," *ACS Nano*, vol. 12, no. 8, pp. 8390–8396, 2018, doi: 10.1021/acsnano.8b03740.

[112] A. Ambrosetti and P. L. Silvestrelli, "Adsorption of rare-gas atoms and water on graphite and graphene by van der waals-corrected density functional theory," *J. Phys. Chem. C*, vol. 115, no. 9, pp. 3695–3702, 2011, doi: 10.1021/jp110669p.

[113] G. Abellán *et al.*, "Fundamental Insights into the Degradation and Stabilization of Thin Layer Black Phosphorus," *J. Am. Chem. Soc.*, vol. 139, no. 30, pp. 10432–10440, 2017, doi: 10.1021/jacs.7b04971.

[114] X. Liu *et al.*, "Robust Amphiphobic Few-Layer Black Phosphorus Nanosheet with Improved Stability," *Adv. Sci.*, vol. 6, no. 23, p. 1901991, Dec. 2019, doi: 10.1002/ADVS.201901991.

[115] X. Liu *et al.*, "Regulating the reactivity of black phosphorus via protective chemistry," *Sci. Adv.*, vol. 6, no. 46, pp. 4359–4370, Nov. 2020, doi: 10.1126/sciadv.abb4359.

[116] Z. Sofer *et al.*, "The Covalent Functionalization of Layered Black Phosphorus by Nucleophilic Reagents," *Angew. Chemie - Int. Ed.*, vol. 56, no. 33, pp. 9891–9896, Aug. 2017, doi: 10.1002/anie.201705722.

[117] V. Nagarajan, R. Ramesh, and R. Chandiramouli, "Chemical sensing properties of σ-PXene sheets towards dioxin vapours – a first-principles insight," *Comput. Theor. Chem.*, p. 114300, Aug. 2023, doi: 10.1016/J.COMPTC.2023.114300.

[118] S. Yang *et al.*, "Azide Passivation of Black Phosphorus Nanosheets: Covalent Functionalization Affords Ambient Stability Enhancement," *Angew. Chemie*, Dec. 2018, doi: 10.1002/ange.201813218.

[119] C. R. Ryder *et al.*, "Covalent functionalization and passivation of exfoliated black phosphorus via aryl diazonium chemistry," *Nat. Chem.*, vol. 8, no. 6, pp. 597–602, 2016,

doi: 10.1038/nchem.2505.

[120] P. Jakóbczyk, A. Dettlaff, G. Skowierzak, T. Ossowski, J. Ryl, and R. Bogdanowicz, “Enhanced stability of electrochemical performance of few-layer black phosphorus electrodes by noncovalent adsorption of 1,4-diamine-9,10-anthraquinone,” 2022, doi: 10.1016/j.electacta.2022.140290.

[121] P. Schattschneider, S. Rubino, and C. Hébert, “Circular Dichroism in the Transmission Electron Microscope,” *Ref. Modul. Mater. Sci. Mater. Eng.*, no. June 2015, pp. 1–14, 2016, doi: 10.1016/b978-0-12-803581-8.03437-8.

[122] L. Q. Guo and M. J. Connelly, “Signal-induced birefringence and dichroism in a tensile-strained bulk semiconductor optical amplifier and its application to wavelength conversion,” *J. Light. Technol.*, vol. 23, no. 12, pp. 4037–4045, 2005, doi: 10.1109/JLT.2005.858214.

[123] G. Park, Y. S. Choi, H. S. Yun, and D. K. Yoon, “Fabrication of Bilayer Dichroic Films Using Liquid Crystal Materials for Multiplex Applications,” *ACS Appl. Mater. Interfaces*, vol. 12, no. 40, pp. 45315–45321, 2020, doi: 10.1021/acsami.0c13663.

[124] F. Xiong, J. Zhang, Z. Zhu, X. Yuan, and S. Qin, “Strong anisotropic perfect absorption in monolayer black phosphorous and its application as tunable polarizer,” *J. Opt. (United Kingdom)*, vol. 19, no. 7, p. 075002, Jun. 2017, doi: 10.1088/2040-8986/aa7292.

[125] M. Fox, *Optical Properties of Solid*. New York: Oxford University Press, 2001.

[126] J. Yu *et al.*, “Direct Observation of the Linear Dichroism Transition in Two-Dimensional Palladium Diselenide,” *Nano Lett.*, vol. 20, no. 2, pp. 1172–1182, 2020, doi: 10.1021/acs.nanolett.9b04598.

[127] Z. Zhou *et al.*, “Perpendicular Optical Reversal of the Linear Dichroism and Polarized Photodetection in 2D GeAs,” *ACS Nano*, vol. 12, no. 12, pp. 12416–12423, 2018, doi: 10.1021/acsnano.8b06629.

[128] M. Oliva-Leyva and G. G. Naumis, “Tunable dichroism and optical absorption of graphene by strain engineering,” *2D Mater.*, vol. 2, no. 2, 2015, doi: 10.1088/2053-1583/2/2/025001.

[129] S. Biswas, M. Y. Grajower, K. Watanabe, T. Taniguchi, and H. A. Atwater, “Broadband electro-optic polarization conversion with atomically thin black phosphorus,” *Science (80-.).*, vol. 374, no. 6566, pp. 448–453, 2021, doi: 10.1126/science.abj7053.

[130] H. Yang *et al.*, “Optical Waveplates Based on Birefringence of Anisotropic Two-Dimensional Layered Materials,” *ACS Photonics*, vol. 4, no. 12, pp. 3023–3030, 2017, doi: 10.1021/acsphotonics.7b00507.

[131] N. Mao *et al.*, “Optical Anisotropy of Black Phosphorus in the Visible Regime,” *J. Am. Chem. Soc.*, vol. 138, no. 1, pp. 300–305, 2016, doi: 10.1021/jacs.5b10685.

[132] D. Dong, Y. Liu, Y. Fan, Y. Fei, J. Li, and Y. Fu, “Tunable THz reflection-type polarizer based on monolayer phosphorene,” *Appl. Opt.*, vol. 58, no. 35, p. 9643, 2019, doi: 10.1364/ao.58.009643.

[133] Y. Li, Z. Hu, S. Lin, S. K. Lai, W. Ji, and S. P. Lau, “Giant Anisotropic Raman Response of Encapsulated Ultrathin Black Phosphorus by Uniaxial Strain,” *Adv. Funct. Mater.*, vol. 27, no. 19, 2017, doi: 10.1002/adfm.201600986.

[134] M. S. Rahman, M. S. Anower, and L. F. Abdulrazak, "Utilization of a phosphorene-graphene/TMDC heterostructure in a surface plasmon resonance-based fiber optic biosensor," *Photonics Nanostructures - Fundam. Appl.*, vol. 35, p. 100711, Jul. 2019, doi: 10.1016/j.photonics.2019.100711.

[135] J. M. Marmolejo-Tejada and A. Jaramillo-Botero, "Partially-oxidized phosphorene sensor for the detection of sub-nano molar concentrations of nitric oxide: A first-principles study," *Phys. Chem. Chem. Phys.*, vol. 21, no. 35, pp. 19083–19091, Sep. 2019, doi: 10.1039/c9cp03912k.

[136] A. N. Abbas *et al.*, "Black phosphorus gas sensors," *ACS Nano*, vol. 9, no. 5, pp. 5618–5624, 2015, doi: 10.1021/acsnano.5b01961.

[137] Y. Wang *et al.*, "Room-Temperature and Humidity-Resistant Trace Nitrogen Dioxide Sensing of Few-Layer Black Phosphorus Nanosheet by Incorporating Zinc Oxide Nanowire," *Anal. Chem*, vol. 10, p. 17, 2021, doi: 10.1021/acs.analchem.9b05623.

[138] C. T. Chasapis, C. A. Spiliopoulou, A. C. Loutsidou, and M. E. Stefanidou, "Zinc and human health: An update," *Archives of Toxicology*, vol. 86, no. 4. Springer, pp. 521–534, Nov. 10, 2012, doi: 10.1007/s00204-011-0775-1.

[139] A. M. Al Alawi, S. W. Majoni, and H. Falhammar, "Magnesium and Human Health: Perspectives and Research Directions," *International Journal of Endocrinology*, vol. 2018. Hindawi Limited, 2018, doi: 10.1155/2018/9041694.

[140] P. B. Tchounwou, C. G. Yedjou, A. K. Patlolla, and D. J. Sutton, "Heavy metal toxicity and the environment," *EXS*, vol. 101. Springer, Basel, pp. 133–164, 2012, doi: 10.1007/978-3-7643-8340-4_6.

[141] Y. Li, X. Hu, X. Zhang, H. Cao, and Y. Huang, "Unconventional application of gold nanoclusters/Zn-MOF composite for fluorescence turn-on sensitive detection of zinc ion," *Anal. Chim. Acta*, vol. 1024, pp. 145–152, 2018, doi: 10.1016/j.aca.2018.04.016.

[142] J. Kudr *et al.*, "Improved electrochemical detection of zinc ions using electrode modified with electrochemically reduced graphene oxide," *Materials (Basel).*, vol. 9, no. 1, p. 31, Jan. 2016, doi: 10.3390/ma9010031.

[143] F. Akhter, A. Nag, M. E. E. Alahi, H. Liu, and S. C. Mukhopadhyay, "Electrochemical detection of calcium and magnesium in water bodies," *Sensors Actuators, A Phys.*, vol. 305, p. 111949, 2020, doi: 10.1016/j.sna.2020.111949.

[144] S. Yang, P. Zhang, A. S. Nia, and X. Feng, "Emerging 2D Materials Produced via Electrochemistry," *Adv. Mater.*, vol. 32, no. 10, 2020, doi: 10.1002/adma.201907857.

[145] H. Xiao *et al.*, "Electrochemical cathode exfoliation of bulky black phosphorus into few-layer phosphorene nanosheets," *Electrochem. commun.*, vol. 89, no. 2017, pp. 10–13, 2018, doi: 10.1016/j.elecom.2018.02.010.

[146] A. Wieloszyńska, P. Jakobczyk, and R. Bogdanowicz, "Polarization-dependent optical absorption in phosphorene flakes," in *Low-Dimensional Materials and Devices 2019*, Sep. 2019, vol. 11085, no. 9, p. 39, doi: 10.1117/12.2528860.

[147] Y. Lee *et al.*, "Atomic-scale imaging of few-layer black phosphorus and its reconstructed edge," *J. Phys. D. Appl. Phys.*, vol. 50, no. 8, p. 84003, 2017, doi: 10.1088/1361-6463/aa5583.

[148] H. Jiang, H. Shi, X. Sun, and B. Gao, “Optical Anisotropy of Few-Layer Black Phosphorus Visualized by Scanning Polarization Modulation Microscopy,” *ACS Photonics*, vol. 5, no. 6, pp. 2509–2515, 2018, doi: 10.1021/acsphotonics.8b00341.

[149] U. Khan, A. O’Neill, H. Porwal, P. May, K. Nawaz, and J. N. Coleman, “Size selection of dispersed, exfoliated graphene flakes by controlled centrifugation,” *Carbon N. Y.*, vol. 50, no. 2, pp. 470–475, 2012, doi: 10.1016/j.carbon.2011.09.001.

[150] C. Huo, Z. Yan, X. Song, and H. Zeng, “2D materials via liquid exfoliation: a review on fabrication and applications,” *Science Bulletin*, vol. 60, no. 23. Ó Science China Press and Springer-Verlag, pp. 1994–2008, 2015, doi: 10.1007/s11434-015-0936-3.

[151] F. I. Alzakia and S. C. Tan, “Liquid-Exfoliated 2D Materials for Optoelectronic Applications,” *Adv. Sci.*, vol. 8, no. 11, 2021, doi: 10.1002/advs.202003864.

[152] J. Liang *et al.*, “2D layered black arsenic-phosphorus materials: Synthesis, properties, and device applications,” *Nano Res.*, vol. 15, no. 4, pp. 3737–3752, 2022, doi: 10.1007/s12274-021-3974-y.

[153] L. Macewicz, K. Pyrchla, R. Bogdanowicz, G. Sumanasekera, and J. B. Jasinski, “Chemical Vapor Transport Route toward Black Phosphorus Nanobelts and Nanoribbons,” *J. Phys. Chem. Lett.*, vol. 12, no. 34, pp. 8347–8354, 2021, doi: 10.1021/acs.jpclett.1c02064.

[154] H. G. Tompkins and J. N. Hilfiker, *Spectroscopic ellipsometry: Practical Application to Thin Film Characterization*. New York, 2015.

[155] J. A. W. Company, *Guide to Using WVASE32*, vol. 30, no. 1. New York, 2010.

[156] H. Fujiwara, *Spectroscopic Ellipsometry: Principles and Applications*. New York, 2007.

[157] A. Wieloszyńska *et al.*, “Tailoring optical constants of few-layer black phosphorus coatings: Spectroscopic ellipsometry approach supported by ab-initio simulation,” *J. Ind. Eng. Chem.*, vol. 127, pp. 579–589, 2023, doi: 10.1016/j.jiec.2023.07.043.

[158] H. Umezawa, Y. Kato, H. Watanabe, A. M. M. Omer, H. Yamaguchi, and S. I. Shikata, “Characterization of crystallographic defects in homoepitaxial diamond films by synchrotron X-ray topography and cathodoluminescence,” *Diam. Relat. Mater.*, vol. 20, no. 4, pp. 523–526, Apr. 2011, doi: 10.1016/j.diamond.2011.02.007.

[159] D. Howell, “Strain-induced birefringence in natural diamond: a review,” *Eur. J. Mineral.*, vol. 24, no. 4, pp. 575–585, 2012, doi: 10.1127/0935-1221/2012/0024-2205.

[160] L. T. M. Hoa, T. Ouisse, D. Chaussende, M. Naamoun, A. Tallaire, and J. Achard, “Birefringence microscopy of unit dislocations in diamond,” *Cryst. Growth Des.*, vol. 14, no. 11, pp. 5761–5766, Nov. 2014, doi: 10.1021/cg5010193.

[161] S. Kunuku *et al.*, “Influence of B/N co-doping on electrical and photoluminescence properties of CVD grown homoepitaxial diamond films,” *Nanotechnology*, vol. 33, no. 12, p. 16, 2022, doi: 10.1088/1361-6528/ac4130.

[162] A. Secroun *et al.*, “Dislocation imaging for electronics application crystal selection,” *Phys. Status Solidi Appl. Mater. Sci.*, vol. 204, no. 12, pp. 4298–4304, 2007, doi: 10.1002/pssa.200776331.

[163] H. Pinto and R. Jones, “Theory of the birefringence due to dislocations in single crystal CVD diamond,” *J. Phys. Condens. Matter*, vol. 21, no. 36, 2009, doi: 10.1088/0953-

8984/21/36/364220.

[164] L. T. M. Hoa, T. Ouisse, and D. Chaussende, “Critical assessment of birefringence imaging of dislocations in 6H silicon carbide,” *J. Cryst. Growth*, vol. 354, no. 1, pp. 202–207, 2012, doi: 10.1016/j.jcrysgro.2012.06.009.

[165] W. Shen, Z. Sun, S. Huo, and C. Hu, “Directly Evaluating the Optical Anisotropy of Few-Layered Black Phosphorus during Ambient Oxidization,” *Adv. Opt. Mater.*, vol. 10, no. 6, pp. 1–10, 2022, doi: 10.1002/adom.202102018.

[166] K. L. Utt *et al.*, “Intrinsic defects, fluctuations of the local shape, and the photo-oxidation of black phosphorus,” *ACS Cent. Sci.*, vol. 1, no. 6, pp. 320–327, 2015, doi: 10.1021/acscentsci.5b00244.

[167] A. Islam, A. van den Akker, and P. X.-L. Feng, “Polarization sensitive black phosphorus nanomechanical resonators,” *Opt. Mater. Express*, vol. 9, no. 2, p. 526, 2019, doi: 10.1364/ome.9.000526.

[168] J. O. Island, G. A. Steele, H. S. J. Van Der Zant, and A. Castellanos-Gomez, “Environmental instability of few-layer black phosphorus,” *2D Mater.*, vol. 2, no. 1, 2015, doi: 10.1088/2053-1583/2/1/011002.

[169] P. C. Chen, A. P. Periasamy, S. G. Harroun, W. P. Wu, and H. T. Chang, “Photoluminescence sensing systems based on copper, gold and silver nanomaterials,” *Coord. Chem. Rev.*, vol. 320–321, pp. 129–138, 2016, doi: 10.1016/j.ccr.2015.12.002.

[170] W. Yan, C. Zhang, S. Chen, L. Han, and H. Zheng, “Two lanthanide metal−organic frameworks as remarkably selective and sensitive bifunctional luminescence sensor for metal ions and small organic molecules,” *ACS Appl. Mater. Interfaces*, vol. 9, no. 2, pp. 1629–1634, Jan. 2017, doi: 10.1021/acsami.6b14563.

[171] M. Ghashghaee, Z. Azizi, and M. Ghambarian, “Theoretical insights into hydrogen sensing capabilities of black phosphorene modified through ZnO doping and decoration,” *Int. J. Hydrogen Energy*, vol. 45, no. 33, pp. 16918–16928, 2020, doi: 10.1016/j.ijhydene.2020.04.138.

[172] X. Jiang, H. Jin, and R. Gui, “Visual bio-detection and versatile bio-imaging of zinc-ion-coordinated black phosphorus quantum dots with improved stability and bright fluorescence,” *Biosens. Bioelectron.*, vol. 165, p. 112390, 2020, doi: 10.1016/j.bios.2020.112390.

[173] C. Cao, B. Zhang, and S. Lin, “P-type ZnO for photocatalytic water splitting,” *APL Mater.*, vol. 10, no. 3, Mar. 2022, doi: 10.1063/5.0083753.

[174] T. Sheela, Y. A. Nayaka, R. Viswanatha, S. Basavanna, and T. G. Venkatesha, “Kinetics and thermodynamics studies on the adsorption of Zn(II), Cd(II) and Hg(II) from aqueous solution using zinc oxide nanoparticles,” *Powder Technol.*, vol. 217, pp. 163–170, Feb. 2012, doi: 10.1016/j.powtec.2011.10.023.

[175] B. K. Rani and S. A. John, “A highly selective turn-on fluorescent chemosensor for detecting zinc ions in living cells using symmetrical pyrene system,” *J. Photochem. Photobiol. A Chem.*, vol. 418, pp. 1010–6030, 2021, doi: 10.1016/j.jphotochem.2021.113372.

[176] P. Wang, D. Zhou, and B. Chen, “High selective and sensitive detection of Zn(II) using tetrapeptide-based dansyl fluorescent chemosensor and its application in cell imaging,”

Spectrochim. Acta - Part A Mol. Biomol. Spectrosc., vol. 204, pp. 735–742, Nov. 2018, doi: 10.1016/j.saa.2018.07.001.

[177] H. Xu, W. Chen, W. Zhang, L. Ju, and H. Lu, “A selective purine-based fluorescent chemosensor for the ‘naked-eye’ detection of zinc ions (Zn2+): applications in live cell imaging and test strips,” *New J. Chem.*, vol. 44, no. 35, pp. 15195–15201, Sep. 2020, doi: 10.1039/d0nj02687e.

[178] L. Hu *et al.*, “Phosphorene/ZnO Nano-Heterojunctions for Broadband Photonic Nonvolatile Memory Applications,” *Adv. Mater.*, vol. 30, no. 30, pp. 1–9, 2018, doi: 10.1002/adma.201801232.

[179] P. Jakóbczyk *et al.*, “Low-power microwave-induced fabrication of functionalised few-layer black phosphorus electrodes: A novel route towards Haemophilus Influenzae pathogen biosensing devices,” *Appl. Surf. Sci.*, vol. 539, 2021, doi: 10.1016/j.apsusc.2020.148286.

[180] D. Nidzworski *et al.*, “A rapid-response ultrasensitive biosensor for influenza virus detection using antibody modified boron-doped diamond,” *Sci. Rep.*, vol. 7, no. 1, pp. 1–10, Nov. 2017, doi: 10.1038/s41598-017-15806-7.

[181] J. Li *et al.*, “Ultrafast Electrochemical Expansion of Black Phosphorus toward High-Yield Synthesis of Few-Layer Phosphorene,” *Chem. Mater.*, vol. 30, no. 8, pp. 2742–2749, 2018, doi: 10.1021/acs.chemmater.8b00521.

[182] Z. H. Ibupoto, S. M. Usman Ali, C. O. Chey, K. Khun, O. Nur, and M. Willander, “Selective zinc ion detection by functionalised ZnO nanorods with ionophore,” in *Journal of Applied Physics*, 2011, vol. 110, no. 10, p. 104702, doi: 10.1063/1.3662107.

[183] N. Ruecha, N. Rodthongkum, D. M. Cate, J. Volckens, O. Chailapakul, and C. S. Henry, “Sensitive electrochemical sensor using a graphene-polyaniline nanocomposite for simultaneous detection of Zn(II), Cd(II), and Pb(II),” *Anal. Chim. Acta*, vol. 874, pp. 40–48, 2015, doi: 10.1016/j.aca.2015.02.064.

[184] R. Ouyang, Z. Zhu, C. E. Tatum, J. Q. Chambers, and Z. L. Xue, “Simultaneous stripping detection of Zn(II), Cd(II) and Pb(II) using a bimetallic Hg-Bi/single-walled carbon nanotubes composite electrode,” *J. Electroanal. Chem.*, vol. 656, no. 1–2, pp. 78–84, 2011, doi: 10.1016/j.jelechem.2011.01.006.

[185] Y. Wu, N. B. Li, and H. Q. Luo, “Simultaneous measurement of Pb, Cd and Zn using differential pulse anodic stripping voltammetry at a bismuth/poly(p-aminobenzene sulfonic acid) film electrode,” *Sensors Actuators, B Chem.*, vol. 133, no. 2, pp. 677–681, 2008, doi: 10.1016/j.snb.2008.04.001.

[186] E. Herrero, V. Arancibia, and C. Rojas-Romo, “Simultaneous determination of Pb2+, Cd2+ and Zn 2+ by adsorptive stripping voltammetry using Clioquinol as a chelating-adsorbent agent,” *J. Electroanal. Chem.*, vol. 729, pp. 9–14, 2014, doi: 10.1016/j.jelechem.2014.06.039.

[187] S. Chandra, K. Sharma, and A. Kumar, “Mg(II) selective PVC membrane electrode based on methyl phenyl semicarbazone as an ionophore,” *J. Chem.*, vol. 2013, 2013, doi: 10.1155/2013/189464.

[188] H. A. Zamani, A. Nezhadali, and M. Saghravanian, “Magnesium-PVC membrane sensor based on 4,5-Bis(benzoylthio)-1,3-dithiole-2- thione,” *Anal. Lett.*, vol. 41, no. 14, pp.

2727–2742, 2008, doi: 10.1080/00032710802363560.

[189] P. Kumar and Y. B. Shim, "A novel Mg(II)-selective sensor based on 5,10,15,20-tetrakis(2-furyl)-21, 23-dithiaporphyrin as an electroactive material," *J. Electroanal. Chem.*, vol. 661, no. 1, pp. 25–30, 2011, doi: 10.1016/j.jelechem.2011.07.005.

[190] M. H. Asif, S. M. U. Ali, O. Nur, M. Willander, U. H. Englund, and F. Elinder, "Functionalized ZnO nanorod-based selective magnesium ion sensor for intracellular measurements," *Biosens. Bioelectron.*, vol. 26, no. 3, pp. 1118–1123, 2010, doi: 10.1016/j.bios.2010.08.017.

List of figures

Fig. 1.1 Top and side views of atomic structure of graphene. 9

Fig. 1.2 a) Measured and calculated absorptance of graphene with 10 layers, 5 layers and monolayer (circle, square and triangle, respectively). b) Absorbance of graphene from 1 to 4 layers. 10

Fig. 1.3 a) Isometric and b) top and side views of atomic structure of $MoSe_2$. The yellow and blue balls represent Mo and Se atoms, respectively. c) Calculated band structures of a – bulk, b – 4-layer, c – 2-layer, and d – monolayer MoS2. 11

Fig. 1.4 a) Absorption spectra of various gold thicknesses, specifically 40 nm, 60 nm, and 80 nm (dashed lines), suspended TMDC (green line) and TMDC on three substrates of Si (blue line), SiO2 (red line) and SiO2 (50 nm)/Si (black line), for a) MoS2 and c) MoSe2. The gold layer is placed between the TMDC and the substrate for b) MoS2 and d) MoSe2 TMDCs. 12

Fig. 1.5 a) Isometric and b) top and side views of atomic structure of phosphorene. 14

Fig. 1.6 a) Photoluminescence spectra of monolayer phosphorene. Reprinted from [50], with permission from Springer Nature. b) Absorption coefficient as a function of the light polarisation angle of a 40 nm BP film. 15

Fig. 1.9 a) Isometric and b) top and side views of atomic structure of b-AsP structure. The orange and purple balls represent P and As atoms, respectively. 15

Fig. 1.10 Example applications for 2D materials. 17

Fig. 1.11 a) Optical microscope image and b) Raman intensity image of WSe_2 lens. 17

Fig. 1.12 Input light at 630 nm and that of the output after passing through a 488 nm thick BP flake. 18

Fig. 2.1 Classification of methods of BP exfoliation. 21

Fig. 2.2 a) XPS spectra of bulk BP (black) and electrochemically exfoliated BP (blue). b) High-resolution XPS spectra of the P 2p signal for bulk BP and electrochemically exfoliated BP. 22

Fig. 2.3 Absorbance spectra for 1–5 layers and bulk BP among a) AC direction and b) ZZ direction.23

Fig. 2.4 Band structure for mono-, bi-, trilayer and bulk BP. 24

Fig. 2.5 Reflection spectra of a) monolayer, b) bilayer, c) trilayer, d) tetralayer, e) pentalayer, and f) bulk BP for AC (x-polarisation) and ZZ (y-polarisation). 25

Fig. 2.6 Extinction coefficient of BP for the AC (red) and ZZ (black) direction. 26

Fig. 2.7 a) Raman spectra of bulk and 1–4L BP, b) layer-dependence of the BP vibrational peaks, c) thickness-dependence of the ratio between A_g^1 mode and silicon peak. 27

Fig. 2.8 Photoluminescence spectra of 1–5 layer-BP. 28

Fig. 2.9 BP flake on a SiO_2/Si substrate a) right after transfer b) after two weeks kept under air. c) Raman spectra for the BP flake in b) at the three points marked in the image on the left. 29

Fig. 2.10 Change of A_g^1/A_g^2 intensity ratio for a) high ratio (HRR) and b) low ratio (LRR) region. 30

Fig. 2.11 Raman spectra at 532 nm on 5 nm thick FLBP at 24, 48, 96 and 120 min after exfoliation. 31

Fig. 2.12 Absorbance at 710 nm for FLBP, and FLBP functionalised by AMPTS, DDTA and PFDTS. 31

Fig. 2.13 Classification of methods of protecting the BP layer against degradation. 32

Fig. 2.14 Scheme for the fabrication of very mono- or few-layers phosphorene covered with an Al_2O_3 layer using plasma oxidation and atomic layer deposition. 33

Fig. 2.15 a) Scheme of a Fabry-Perot cavity with 4 layers – hexagonal boron nitride, tri-layer BP, hexagonal boron nitride and gold. b) Polarised absorption from a Fabry-Perot cavity based on tri-layer BP for different doping electrons and holes along the AC direction. 35

Fig. 2.16 Brightness of the reflected light from a thick BP as a function of the rotation angle from three RGB channels. 35

Fig. 2.17 a) Schematic of an integrated tilted fibre grating configuration based on BP. b) Schematic of a fibre optic surface plasmon resonance based on phosphorene. 37

Fig. 2.16 Fluorescence of black phosphorus quantum dots for different concentrations of mercury ions. 38

Fig. 4.1 Transmittance curves of FLBP centrifugated at 9000 rpm, 3000 rpm, and 0 rpm. 44

Fig. 4.2 Polarisation images of FLBP centrifuged at a) 0 rpm, b) 3000 rpm, c) 6000 rpm, and d) 9000 rpm for the second and third sets of samples. 45

Fig. 4.3 Polarisation images of FLBP centrifuged at a) 0 rpm, b) 3000 rpm, c) 6000 rpm, and d) 9000 rpm with a 0°, 30° and 60° rotational angle. 47

Fig. 4.4 SEM images of FLBP centrifuged at a) 0 rpm, b) 3000 rpm, c) 6000 rpm, and d) 9000 rpm. 48

Fig. 4.5 Absorbance of few-layer black phosphorus with different centrifugation speeds. 49

Fig. 4.6 Microscopic image of mechanically exfoliated FLBP on Si substrate. 50

Fig. 4.7 Microscopic image of mechanically exfoliated FLBP on Si substrate immediately after exfoliation and after 30 days. 50

Fig. 4.8 Absorbance of black arsenic-phosphorene with different concentrations of As and BP. 51

Fig. 4.9 a) 3k-BP-ZnO NRs and b-AsP-ZnO NRs on Si and b) 3k-BP-ZnO NFs and b-AsP-ZnO NFs electrodes preparation. 53

Fig. 4.10 Comparison of PL spectra of ZnONRs, BP-ZnONRs and b-AsP-ZnONRs 54

Fig. 4.11 SEM images of a) 3kBP-ZnO NFs and b) b-AsP-ZnO NFs. 55

Fig. 4.12 Plot of a) Delta and b) Psi azimuths of Si wafer and FLBP centrifuged centrifugated with 9000 rpm, 3000 rpm, and 0 rpm for the wavelength range of 250 nm to 690 nm. 56

Fig. 4.13 Plot of a) Delta and b) Psi azimuths of Si wafer and FLBP centrifugated at 0 rpm, 6000 rpm and 9000 rpm for wavelength range of 260 nm to 830 nm. 57

Fig. 4.14 a) Delta and b) psi of FLBP centrifuged at 6000 rpm for wavelength range of 190 nm to 2000 nm. 57

Fig. 4.15 Model used in the analysis of the ellipsometry data. 58

Fig. 4.16 a) Extinction coefficient and b) refractive index of the FLBP-6k sample, obtained from analysis the ellipsometry data. 59

Fig. 4.17 Scheme of a polarised light microscope. The angle γ is a rotational angle between crossed polarisers and sample. 60

Fig. 4.18 B/N co-doped diamond grown on SCD IIa substrate for different B concentrations before annealing: a) 2,500 ppm, b) 5,000 ppm, and c) 7,500 ppm and for different B concentrations after the annealing: d) 2,500 ppm, e) 5,000 ppm, and f) 7,500 ppm. 61

Fig. 4.19 B/N co-doped diamond grown on SCD Ib substrate for different B concentration before annealing: a) 2500 ppm, b) 5000 ppm, and c) 7500 ppm and for different B concentration after the annealing: d) 2500 ppm, e) 5000 ppm, and f) 7500 ppm. 62

Fig. 4.20 B/N co-doped diamond grown with B concentration 2500 ppm on SCD Ib substrate for different angles between the sample and the polariser: a) 0°, b) 45°, c) 90°, d) 135°, e) 180°. 62

Fig. 4.21 a) Microscopic image of liquid-exfoliated FLBP. B–f) Polarisation images of the region marked with a red rectangle as a function of rotation angle. 64

Fig. 4.22 a) Polarisation image of FLBP-0k$_{\mathrm{DMF}}$. b) Red (R), c) green (G), and d) blue (B) image extracted from the image at a). e) The intensity of RGB channels as a function of the rotation angle. 65

Fig. 4.23 FLBP-0k$_{\mathrm{DMF}}$ averaged intensity values from polarisation images as a function of angle changes in time for a) red (R), b) green (G), and c) blue (B) channel. 66

Fig. 4.24 a) Microscopic image of mechanically exfoliated FLBP$_{\mathrm{MECH}}$. b–f) Polarisation images of the region marked with a red rectangle as a function of the rotation angle. The region more responsive to changes in the rotation angle is marked with blue rectangle. 67

Fig. 4.25 Averaged red-green-blue (RGB) intensity values from polarisation images as a function of the angle for a) the background and b) the BP flake. 68

Fig. 4.26 BP flake averaged intensity values from polarisation images as a function of angle changes in time for a) red, b) blue, and c) green channel. 69

Fig. 4.27 FLBP optical intensity as a function of rotation angle for four consecutive days. 70

Fig. 4.28 Comparison of FLBP optical intensity as a function of rotation angle on the first day and after 35 days. 70

Fig. 4.29 Photoluminescence sensor setup based on ZnO-BP to detect metal ions. 72

Fig. 4.30 a) Photoluminescence spectra of ZnONRs under the influence of zinc ions of different concentrations, and the PL signal changes in time at b) 382 nm, c) 447 nm, and d) 520 nm. Red arrows indicate when the flow was switched to the syringe with ions; blue arrows – when it was switched to the syringe with pure water. 73

Fig. 4.31 Changes of PL signal of ZnO NRs at a) 382 nm and b) 447 nm the under influence of Zn^{2+}, Ca^{2+}, Mg^{2+}, Na^{+} and Cu^{2+}. Red arrows indicate when it was switched to the syringe with different ions. 74

Fig. 4.32 Photoluminescence spectra of 3kBP-ZnO NRs under the influence of zinc ions with different concentrations, and the PL signal changes in time at b) 381 nm, c) 446 nm, and d) 520 nm. Red arrows indicate when the flow was switched to the syringe with ions; blue arrows when it was switched to the syringe with pure water. 75

Fig. 4.33 a) Photoluminescence spectra of 3kBP-ZnO NRs under the influence of magnesium ions with different concentrations, and the PL signal changes in time at b) 380 nm, c) 446 nm, and d) 520 nm. Red arrows indicate when the flow was switched to the syringe with ions; blue arrows when it was switched to the syringe with pure water. 76

Fig. 4.34 a) Photoluminescence spectra of b-AsBP-ZnONRs under the influence of different concentrations of zinc ions, and the changes in the PL signal in time at b) 380 nm, c) 440 nm, and d) 520 nm. Red arrows indicate when the flow was switched to the syringe with ions; blue arrows when it was switched to the syringe with pure water. 77

Fig. 4.35 Changes in the photoluminescence signal of b-AsBP-ZnONRs at a) 520 nm, b) 442 nm and 380 nm under the influence of Zn^{2+} with different concentrations. Red arrows indicate when the flow was switched to the syringe with ions; blue arrows when it was switched to the syringe with pure water. 78

Fig. 4.36 Electrochemical sensor setup with a counter electrode (C), reference electrode (R) and working electrode (W) immersed in electrolyte and connected to a potentiostat. 80

Fig. 4.37 a) CV response of the ZnO NFs electrode in $K_4[Fe(CN)_6]$ PBS electrolyte with different concentration of zinc ions. b) Change of current at the oxidations peak in the presence of 0.08 nM of Zn^{2+}. 80

Fig. 4.38 Voltammograms for different concentration of zinc ions (0–0.71 nM) a) without LED and b) with LED illuminating the b-AsP-ZnONFs electrode. c) Current peaks from voltammograms for different concentrations of zinc ions without LED (marked on black) and with LED (marked on red). 81

Fig. 4.39 a) Voltammograms for different concentrations of zinc ions (0–2.25 nM) with the b-AsP-ZnO NFs electrode. b) Current peaks from voltammograms for different concentrations of zinc ions. 82

Fig. 4.40 a) CV response of the 3kBP-ZnO NFs electrode in $K_4[Fe(CN)_6]$ PBS electrolyte for a 0 nM and 0.16 nM concentration of Zn^{2+} ions without and with LED illuminating the electrode. 83

Fig. 4.41 Voltammograms for different concentrations of zinc ions (0–4 nM) a) without LED and b) with LED illuminating the 3kBP-ZnO NFs electrode. c) Current at the oxidation peak from voltammograms for different concentrations of zinc ions without LED (marked as dark) and with LED. 84

Fig. 4.42 a) Voltammograms for different concentrations of magnesium ions (0–1.3 nM) with the 3kBP-ZnO NFs used as the working electrode. b) Current peaks from voltammograms for different concentrations of $Mg^{2+}$with trendline. 85

List of tables

Table 1.1 Comparison of parameters of graphene, TMDCs and phosphorene. 14

Table 2.1 Comparison of all allotropes of phosphorus 20

Table 4.1. Designations of all sets of electrochemical exfoliated FLBP samples. 44

Table 4.2. Designations of liquid-exfoliated FLBP in ethanol. 49

Table 4.3. Amount of reagents used in CVD process for obtained compositions of b-AsP. 51

Table 4.4. Sample designations 53

Table 4.5 Range and limit of detection of zinc ions for different method. 84

Table 4.6 Range and limit of detection of magnesium ions for different method. 85

Table 4.7 Comparison of properties for ZnO NFs electrodes without and with BP or b-AsP. 86